

Copyright  
by  
Joseph Arthur Dowd  
2001

**Response of Stay Cables to High-Amplitude Vibration**

**by**

**Joseph Arthur Dowd, B.S.**

**Thesis**

Presented to the Faculty of the Graduate School of

The University of Texas at Austin

in Partial Fulfillment

of the Requirements

for the Degree of

**Master of Science in Engineering**

**The University of Texas at Austin**

**May 2001**

# **Response of Stay Cables to High-Amplitude Vibration**

**Approved by  
Supervising Committee:**

---

**Eric B. Williamson**

---

**Karl H. Frank**

## **Dedication**

*To Alisa*

## **Acknowledgements**

I would like to thank everyone who made the completion of this thesis possible. Funding for the project was provided by the Texas Department of Transportation. Particularly, my appreciation goes to Elton Brown, Randy Cox and Keith Ramsey.

This study was a portion of a larger project organized by Whitlock Dalrymple Poston and Associates (WDP). I would like to thank WDP, especially Dr. Randy Poston, for assisting during field tests, providing valuable resources concerning the general project, and facilitating The University of Texas at Austin's role in the study.

Several other universities were involved in the general project. Researchers at Johns Hopkins University allowed the use of their data acquisition system on the Fred Hartman Bridge. This service, coupled with intelligent and willing answers to countless questions, have indebted me to Dr. Nick Jones, Ender Ozkan, and Joseph Main.

The laboratory testing, as well as preparation for fieldwork, was performed at Ferguson Structural Engineering Laboratory (FSEL) on the University of Texas at Austin's Pickle Research Campus. I would like to thank

sincerely the technical and office staff at FSEL for their hard work and patience. Mike Bell, Dennis Phillip, Ray Madonna, and Blake Stasney have taught me more than they know during the numerous hours that they have spent helping. Regina Forward, Ruth Goodson, Wanda Kitts, and Dijaira Smith have turned so many potential problems into solutions. Thanks to all of you.

I would also like to thank *all* of my fellow students at FSEL. Their companionship and willingness to lend a helping hand have been one of the highlights of my time at FSEL. I would especially like to thank those friends that have taken time away from their projects to help me with mine including Charles Bowen, Ben Cheplak, Kazuo Endo, Michael Hagenberger, and Dan Thatcher. My research partner throughout the majority of this study has been Marcel Poser. I would like to thank him for his help, input, and companionship.

My sincere appreciation goes to the professors guiding this study: Dr. Karl Frank, Dr. Michael Kreger, Dr. Eric Williamson, and Dr. Sharon Wood. Each has willingly given of their time to teach me a great deal about structural engineering. I would especially like to thank my supervisor, Dr. Williamson, for his input, promptness, and advice.

My parents Joe and Judy Dowd, along with the rest of my family, deserve gratitude for their years of love and encouragement. They have enthusiastically supported me in all of my academic endeavors, and I would never have made it to graduate school without them.

I would never have made it *through* graduate school without the encouragement and valued input of my beautiful wife Alisa. Without her patience

my research would not have been possible. Without her love, *my* patience would not have been possible.

Finally, I would like to thank God for giving me the strength and wisdom to achieve this goal and for blessing me with all of the people that helped make it possible.

May 4, 2001

## **Abstract**

### **Response of Stay Cables to High Amplitude Vibration**

Joseph Arthur Dowd, M.S.E.

The University of Texas at Austin, 2001

Supervisor: Eric B. Williamson

The development of cable-stayed bridges has included the discovery of unique phenomena such as rain-wind induced cable vibration. Excessive lateral motion of cables, supporting structures such as the Fred Hartman Bridge, has prompted the need to assess the degree of bending fatigue damage sustained by these cables. Characterization of vibration events has been attempted through strain measurements in the field. Finite element analyses of stay cables have indicated large steel and grout stresses near the anchorage region. Similar modeling of laboratory specimens has led to a geometry that mimics the curvature profile of an actual stay cable. A full-scale diameter, 32-foot long specimen was fatigue tested under cyclic transverse load to validate the finite element models. The long-term goal of this research is the establishment of a set of procedures for evaluating stay cable fatigue damage that will allow their condition to be identified, reliably predicting the current lifespan of individual bridge cables.



## Table of Contents

List of Tables .....	xiv
List of Figures.....	xv
Chapter 1: Cable-Stayed Bridges: History and Development.....	1
History of Cable-Stayed Bridges.....	1
Problems with Cable-Stayed Bridges .....	6
Chapter 2: Stay Cables and Their Vibration.....	9
Cables for Cable-Stayed Bridges.....	10
Helical Wire Rope (Spiral Strand).....	10
Locked-Coil Strand.....	11
Parallel Wire Strand (PWS).....	11
Parallel Wire Cable (PWC) .....	12
Parallel Strand Cable .....	13
Corrosion Protection Techniques .....	14
Cable Vibration Mechanisms .....	16
Vortex Shedding.....	16
Galloping .....	17
Buffeting.....	17
Wake Effects.....	17
Parametric Excitation .....	18
Rain-Wind Induced Vibration .....	18
Mitigation Techniques for Rain-Wind Induced Vibration .....	21
Structural Mitigation Techniques for Rain-Wind Induced Vibration.....	22
Mechanical Mitigation Techniques for Rain-Wind Induced Vibration.....	23

Aerodynamic Mitigation Techniques for Rain-Wind Induced Vibration.....	23
Chapter 3: Cable-Stayed Bridges of Texas: Vibration and Remediation	
History .....	25
Veterans Memorial Bridge: Background and Vibration History.....	25
Fred Hartman Bridge: Background .....	26
Cables of the Fred Hartman Bridge.....	26
Stay Cable Vibration History of the Fred Hartman Bridge .....	30
Evaluation and Repair of Stay Cable Vibrations on the Fred Hartman Bridge .....	32
Structural Repair.....	33
Instrumentation and Characterization of Cable Vibration.....	34
Mechanical Mitigation Efforts.....	34
Aerodynamic Mitigation Efforts .....	35
The Role of The University of Texas at Austin in the Vibration Investigation of the Fred Hartman Bridge.....	36
Bending Fatigue.....	36
Plan for Assessment of Bending Fatigue Damage .....	38
Visual Field Inspection.....	38
Field Strain Measurements .....	41
Analytical Modeling of Stay Cables.....	43
Laboratory Bending Fatigue Testing.....	44
Chapter 4: Measurement of Strain on the Stay Cables of the Fred Hartman Bridge .....	46
Primary Strain Acquisition Attempts .....	46
Strain Collection Instrumentation.....	47
Strain Gage Description and Location.....	49
Results of Initial Instrumentation Set-Up.....	50
Attempts to Repair the Strain Collection System.....	52
Results of Reinstallation of Strain Collection System.....	54

Further Problems and Noise Elimination Attempts.....	57
Characterization of Observed Strain Events from Primary Strain	
Acquisition Attempts.....	58
Expected Indicators of Cable Vibration .....	58
Traffic Events .....	60
Deck Vibration Events.....	62
Secondary Strain Acquisition Attempt.....	64
Strain Gage Description and Location.....	64
Pluck Test Description and Results .....	65
Chapter 5: Finite Element Modeling of Fred Hartman Bridge Stay Cables.....	69
Modeling of Cable A24S.....	69
Mesh Description and Model Properties .....	70
Modeling Contact with the Anchorage Box Opening .....	71
Tensioning of the Cable Model .....	72
Details of the Analysis.....	74
Results of Modal Extraction.....	77
Methods of Dynamic Excitation.....	77
Results of the Dynamic Analysis.....	81
Modeling of Cable A22S.....	84
Mesh Description, Model Properties, and Analysis Details.....	85
Results of Modal Extraction.....	86
Method of Dynamic Excitation .....	87
Results of the Dynamic Analysis.....	90
Axial Strain Representation of Lateral Vibration.....	93
Validation of Finite Element Models .....	96
Chapter 6: Design and Finite Element Modeling of a Laboratory Stay Cable	
Specimen .....	98
Defined Specimen Parameters.....	98
Specimen Variables .....	102

Modeling of the Specimen.....	103
Model Properties and Analysis Details .....	103
Intermediate Iteration Results.....	104
Modeling of the Ram Clamp for Dynamic Excitation .....	106
Direct Displacement Control .....	107
Contact Surfaces with Internal Curvature .....	109
Stepped Midspan Grout Section.....	112
Ram Clamp with Graduated Stiffness .....	114
Preliminary Stress Profile Predictions Before Start of First Laboratory Test.....	116
Chapter 7: Finite Element Model Adaptation and Validation Through a Bending Fatigue Test of a Stay Cable Specimen .....	120
Description of the Bending Fatigue Test.....	120
Strain Collection Instrumentation.....	122
Experimental Results.....	125
Static Test Strain Results.....	125
Sample Dynamic Test Strain Results .....	127
Deterioration of Stress Ranges .....	128
Validation and Adaptation of the Specimen Finite Element Model..	129
Comparison of Models to Measured Data Using Displaced Shape .....	131
Comparison of Models to Measured Stress Ranges Near the Anchorage Plate.....	135
Comparison of Models to Measured Stress Ranges Near the Tension Ring.....	137
Comparison of Models to Measured Stress Ranges Near the Ram Clamp .....	140
Comparison of Models to Measured Data Using Hydraulic Ram Force and First Fundamental Frequency.....	141
Optimum Specimen Finite Element Model.....	144

Chapter 8: Summary, Conclusions, and Recommendations for Future Work ...	146
Measurement of Strain on the Stay Cables of the Fred Hartman Bridge .....	146
Finite Element Modeling of Fred Hartman Bridge Stay Cables .....	147
Effect of End Rotation.....	148
Finite Element Modeling of Laboratory Stay Cable Specimen.....	151
Material Property Adjustment .....	151
Modeling Stages of Fatigue Deterioration.....	153
Bibliography .....	156
Vita... ..	160

## List of Tables

Table 3.1: Large-Amplitude Vibration Events on the Fred Hartman Bridge (Weaver and Poston 1998) .....	31
Table 5.1: Comparison of Measured and Calculated Natural Frequencies of Cable A24S.....	77
Table 5.2: Comparison of Cable A24S Finite Element Models at Peak of Cable Motion .....	84
Table 5.3: Comparison of Measured and Calculated Natural Frequencies of Cable A22S.....	87
Table 5.4: Comparison of Cable A22S and Cable A24S Finite Element Models at Peak of Cable Motion .....	93
Table 6.1: Target Ratios of Stress or Curvature at Anchorage Plate to Tension Ring for Peak Motion Results from Cable A22S Model.....	101
Table 6.2: Comparison of Curvature and Stress Profiles for Specimen and Cable A22S Models.....	119
Table 7.1: Schedule of Specimen Finite Element Models Based on Degree of Cracking.....	131

## List of Figures

Figure 1.1: Albert Bridge.....	2
Figure 1.2: Brooklyn Bridge.....	2
Figure 1.3: Roebling’s Niagara Falls Bridge.....	3
Figure 1.4: Roebling’s Niagara Falls Bridge – 1875.....	3
Figure 1.5: Major Components of a Modern Cable-Stayed Bridge .....	3
Figure 1.6: Theodor Huess Bridge .....	4
Figure 1.7: Severins Bridge .....	5
Figure 1.8: Fred Hartman Bridge .....	8
Figure 2.1: The Stay Cables of the Fred Hartman Bridge .....	9
Figure 2.2: Example Locked-Coil Strand Cross-Section .....	11
Figure 2.3: Example Parallel Wire Strand Cross-Section .....	11
Figure 2.4: Example Parallel Wire Cable Cross-Section .....	13
Figure 2.5: Example Parallel Strand Cable Cross-Section .....	13
Figure 2.6: Example Cross Section of Grouted Stay Cable .....	15
Figure 2.7: Vortex Shedding .....	16
Figure 2.8: Rain-Wind Induced Vibration.....	20
Figure 2.9: Cable Restrainers on the Fred Hartman Bridge .....	22
Figure 3.1: Veterans Memorial Bridge.....	25
Figure 3.2: The Fred Hartman Bridge .....	27
Figure 3.3: The Fred Hartman Bridge from South Pylon.....	27
Figure 3.4: Cross Section of Typical Stay Cable Anchorage .....	29
Figure 3.5: Typical Stay Cable Anchorage Transition.....	29

Figure 3.6: Peaks of Motion from a Video of Vibration of Cable A24S on the Fred Hartman Bridge .....	31
Figure 3.7: Failed Connection of Guide Pipe to Anchorage Box.....	32
Figure 3.8: Retrofit Stiffeners on Guide Pipe.....	33
Figure 3.9: Prototype Linear Damper.....	35
Figure 3.10: Prototype Freyssinet Damper.....	35
Figure 3.11: Inspection of Grout in Anchorage Region .....	39
Figure 3.12: Location of Polyethylene Sheath Inspection.....	40
Figure 3.13: Indentation in Polyethylene Sheath at Anchorage Box .....	40
Figure 3.14: Strain Gage Applied to Grout Surface .....	41
Figure 3.15: Sample Strain Data Produced by Ambient Traffic Response .....	42
Figure 3.16: Stay Cable Strain Gage Locations .....	42
Figure 4.1: Data Collector Maintained by Johns Hopkins University Inside the Southeast Pylon .....	47
Figure 4.2: Four Signal Conditioners Mounted in a Box .....	48
Figure 4.3: Schematic of Instrumentation for Strain Data Collection.....	49
Figure 4.4: Cable A22S Showing Window in Polyethylene Sheath Where Strain Gages Were Located .....	50
Figure 4.5: Strain Gage.....	51
Figure 4.6: Typical Noise Signal from Strain Data Collection .....	52
Figure 4.7: Corrosion Damage to Strain Gage .....	53
Figure 4.8: CR9000 Mobile Data Acquisition System.....	54
Figure 4.9: Sample Traffic Data Collected by CR9000 on Cable A22S .....	55



Figure 4.10: Typical Strain Record Excerpt from Cable A22S Following Reinstallation of Instrumentation .....	56
Figure 4.11: Typical Signal Excerpt from the Channels Assigned to Cable A22S Prior to Reinstallation of Instrumentation .....	56
Figure 4.12: Strain Record Excerpt from a Typical Traffic Event.....	61
Figure 4.13: Five Minute Strain History (with Floating Averaging) Showing Traffic Events and Deck Vibration.....	63
Figure 4.14: Strain Record Excerpt from a Typical Deck Vibration Event .....	63
Figure 4.15: Encapsulated Strain Gage on Cable A22S.....	65
Figure 4.16: Pluck Test of Cable A22S.....	66
Figure 4.17: Sample Acceleration Frequency Response.....	67
Figure 4.18: Sample Strain Frequency Response.....	67
Figure 5.1: Two of the Eight Stay Cables Designated as Cable 24.....	70
Figure 5.2: Linear Mesh of Cable A24S for ABAQUS Finite Element Model ....	71
Figure 5.3: Nonlinear Spring Representation of Anchorage Box Opening.....	72
Figure 5.4: <i>Worst-Case Scenario</i> Vibration Event for Cable A24S Model .....	78
Figure 5.5: Excitation Using Cyclic Transverse Point Loads .....	79
Figure 5.6: Extreme Grout Fiber Stress Profile for 25 feet of Cable A24S Model Nearest the Deck Anchorage.....	82
Figure 5.7: Extreme Steel Fiber Stress Profile for 25 feet of Cable A24S Model Nearest the Deck Anchorage.....	83
Figure 5.8: Linear Mesh of Cable A22S for ABAQUS Finite Element Model ....	85

Figure 5.9: Example of Indentation in Polyethylene Sheath at Anchorage Box Opening .....	88
Figure 5.10: Extreme Grout Fiber Stress Profile for 20 feet of Cable A22S Model Nearest the Deck Anchorage.....	91
Figure 5.11: Extreme Steel Fiber Stress Profile for 20 feet of Cable A22S Model Nearest the Deck Anchorage.....	92
Figure 5.12: Comparison of Axial and Flexural Strain at the Strain Gage Location on Cable A22S.....	94
Figure 5.13: Axial Strain Ranges at the Cable A22S Gage Location Corresponding to Maximum Mean-to-Peak Displacement Amplitudes.....	97
Figure 6.1: Cable Stay Bending Fatigue Specimen.....	99
Figure 6.2: Extreme Steel Fiber Stress Profile for 20 feet of Cable A22S Model Nearest the Deck Anchorage.....	100
Figure 6.3: Geometric Variable Parameters of the Specimen Model.....	102
Figure 6.4: Typical Specimen Steel Stress Profile in the Anchorage Zone for a Peak of Motion .....	105
Figure 6.5: Typical Specimen Steel Stress Profile for a Peak of Motion.....	107
Figure 6.6: Effect of Ram Clamp Length on Steel Stress Profile When Using Direct Displacement Control .....	108
Figure 6.7: Specimen and Clamp with Internal Curvature .....	110
Figure 6.8: Effect of Ram Clamp Internal Curvature on Steel Stress Profile When Using Contact Surface Control .....	111

Figure 6.9: Specimen with Stepped Midspan Grout Section.....	112
Figure 6.10: Effect of Midspan Stepped Grout Diameter Length on Steel Stress Profile.....	113
Figure 6.11: Ram Clamp Used for First Laboratory Fatigue Test.....	114
Figure 6.12: Cross-Section and Modeling Approach for Ram Clamp Used for First Laboratory Test .....	115
Figure 6.13: Predicted Extreme Steel Fiber Stress Profiles for Peaks of Motion – Uncracked Model .....	117
Figure 6.14: Predicted Extreme Grout Fiber Stress Profiles for Peaks of Motion – Uncracked Model.....	118
Figure 7.1: Installation of Strand During Construction of Stay Cable Specimen	121
Figure 7.2: Stay Cable Bending Fatigue Test.....	122
Figure 7.3: Locations of Strain Gages for First Stay Cable Specimen.....	123
Figure 7.4: Strain Gages Near the Tension Ring.....	124
Figure 7.5: Strain Gages Near the Anchorage Plate.....	124
Figure 7.6: Top Gage Strain Histories for Upward Motion of the Static Test ....	125
Figure 7.7: Top Gage Strain Histories for Downward Motion of the Static Test	127
Figure 7.8: Strain Histories During Cycling at 77,000 Cycles.....	128
Figure 7.9: Deterioration of Extreme Steel Fiber, Fatigue Stress Ranges.....	130
Figure 7.10: General Agreement of Specimen Models to Measured Data Based Upon Displacement Range .....	132
Figure 7.11: Agreement of Specimen Models to Measured Data Based Upon Displacement Range Near Anchorage Without Wire Breaks.....	133

Figure 7.12: Agreement of Specimen Models to Measured Data Based Upon Displacement Range Near Anchorage With Wire Breaks.....	135
Figure 7.13: Comparison of Predicted and Measured Extreme Steel Fiber Fatigue Stress Ranges Near the Anchorage Plate.....	136
Figure 7.14: Comparison of Predicted and Measured Extreme Steel Fiber Fatigue Stress Ranges Near the Tension Ring.....	138
Figure 7.15: Extreme Steel Fiber Stress Profiles for Models 1 and 2 .....	139
Figure 7.16: Comparison of Predicted and Measured Extreme Steel Fiber Fatigue Stress Ranges Near the Ram Clamp .....	140
Figure 7.17: Comparison of Predicted and Measured Ram Force Range .....	142
Figure 7.18: Comparison of Predicted First Fundamental Frequencies .....	143
Figure 8.1: Effect on Stress Profile of End Rotation Due to Local Damage.....	149

## **Chapter 1: Cable-Stayed Bridges: History and Development**

Cable-stayed bridges comprise well over two hundred of the world's bridges. Currently, about twenty cable-stayed bridges grace the infrastructure of the United States, including two maintained by the state of Texas. While the basic technology behind cable-stayed bridges has existed for centuries, only within the past few decades has the structural form gained widespread popularity. The aesthetic appeal and efficient constructability of cable-stayed technology have initiated this popularity surge that has, perhaps, proceeded too rapidly. Recent problems such as corrosion and excessive cable vibration have led to serviceability concerns about the true life span of a typical cable-stayed bridge. Understanding and correcting these problems is vital to cable-stayed bridge technology.

### **History of Cable-Stayed Bridges**

The use of a long slender element to carry tension is far from a new concept. Ropes, vines, chains, and cables have been used to carry load for centuries. They have been used in bridge designs for, doubtlessly, as long. An 1823 study by French engineer C. L. Navier represents one of the earliest records of cable-stay bridge technology as it appears today. Remarkably, Navier considered several multi-cable arrangements that were not to again surface for generations. Navier concluded, however, that suspension bridge designs were superior to cable-stayed bridge designs. These conclusions, coupled with



**Figure 1.1: Albert Bridge**

Photo courtesy of Godden Collection, Earthquake Engineering Library, University of California, Berkeley.



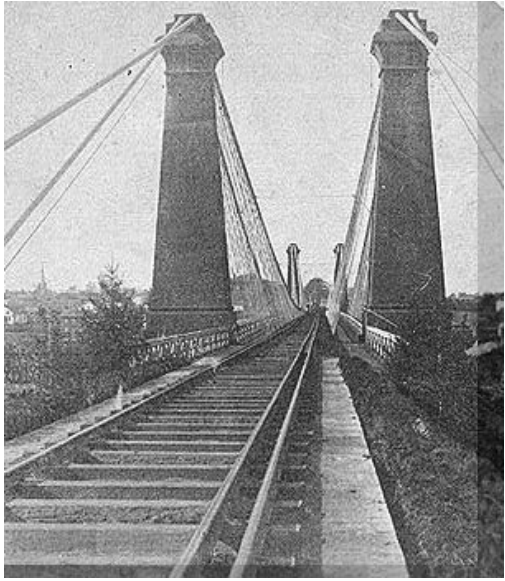
**Figure 1.2: Brooklyn Bridge**

Photo courtesy of Godden Collection, Earthquake Engineering Library, University of California, Berkeley.

fabrication difficulties in cable-stayed bridges that had already been attempted, delayed the construction of the first successful pure cable-stayed bridges until the middle of the twentieth century (Gimsing 1999).

In the interim, many bridges were designed and constructed that combined cable-stayed and suspension bridge technology. One of the earliest examples is the 1873 Albert Bridge spanning the Thames in London shown in Figure 1.1 (Gimsing 1999). In the United States, John Roebling used the combined technology to create such structural engineering landmarks as the 1883 Brooklyn Bridge (Figure 1.2) and the 1854 Niagara Falls Bridge (Figure 1.3 and Figure 1.4). The latter was a combined railway and roadway bridge incorporating a wood truss system with the first major use of air-spun wire cables invented by Roebling. The structure was replaced in 1897 (Gimsing 1997; Berketa 2000).

A modern cable-stayed bridge is generally considered to be one that relies solely on cable-stayed technology as its main structural support system. The major components of a modern cable-stayed bridge are shown in Figure 1.5.



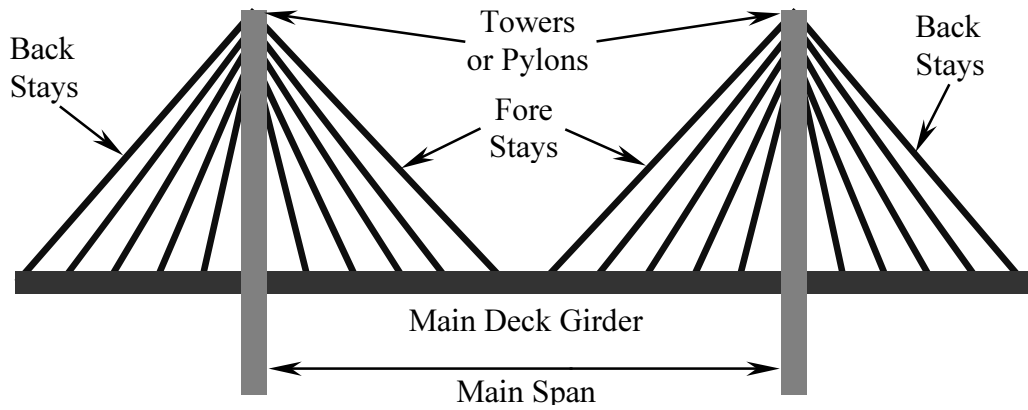
**Figure 1.3: Roebling's Niagara Falls Bridge**

Photo courtesy Rick Berketa.



**Figure 1.4: Roebling's Niagara Falls Bridge – 1875**

Photo courtesy Rick Berketa.



**Figure 1.5: Major Components of a Modern Cable-Stayed Bridge**

Conceptually, the bridge's main deck girder is suspended from stay cables that transfer the bridge load into the towers or pylons. The stay cables that support the main span are termed fore stays while the stay cables that equilibrate the horizontal component of the fore stay load at the pylon are called back stays. It is common, but not necessary, to have one fore stay for every back stay. Each pair may even be comprised of a single cable draped over a saddle at the top of the pylon.

Most literature including Gimsing (1997, 1999) and Ohashi (1991) credit the 1955 Strömsund Bridge in Sweden as the first modern pure cable-stayed bridge. Designed by Dischinger, the Strömsund Bridge carries a main span of 599 feet (182.6 meters). Integral in the early development of modern cable-stayed bridges was a trio of German bridges: the 1957 Theodor Huess Bridge (Figure 1.6), over the Rhine, the 1961 Severins Bridge in Köln (Figure 1.7) and the



**Figure 1.6: Theodor Huess Bridge**

Photo courtesy of Godden Collection, Earthquake Engineering Library, University of California, Berkeley.





**Figure 1.7: Severins Bridge**

Photo courtesy of Nicolas Janberg, Webmaster of [www.structurae.de](http://www.structurae.de).

Norderelbe Bridge in Hamburg. Germany is often considered the birthplace of the cable-stayed bridge because each of these bridges offered something new with regard to the development of modern cable-stayed bridges (Gimsing 1997).

This development has continued to the present day. In the United States alone, several new cable-stayed bridges are either being designed or constructed. The Charles River crossing in Boston, Massachusetts is on schedule to become the newest cable-stayed bridge in the United States in 2002. Its design includes a great deal of new technology including ungrouted cables with internal damping devices. The Charles River crossing will be the widest cable-stayed bridge in the world (Angelo 2000). In 1999, the world's longest cable-stayed bridge, the Tatara Bridge, opened in Japan. Its main span of 2920 feet (890 meters) may be compared to the Strömsund Bridge's main span of 599 feet (182.6 meters) as testimony to the progress that cable-stayed bridge technology has made in less than a half-century. This progress, however, has not come without a cost.

## **Problems with Cable-Stayed Bridges**

A recent international survey of cable-stayed bridge owners showed that the average expected lifespan of their bridges' stay cables is 75 years (Hamilton, Breen, and Frank 1998). Serviceability failures throughout the fifty-year history of modern cable-stayed technology have proven the surveyed bridge owners to be, perhaps, a little optimistic.

Watson and Stafford (1988) surveyed what at the time was more than half of the world's cable-stayed bridges. They reported evidence of cable corrosion on many of them. Almost every specified technique for corrosion protection had experienced some failure. Surprisingly, some of the bridges investigated had been repaired previously. For example, Germany's Köhlbrand Estuary Bridge required replacement of its cables due to corrosion after only three years of service (Watson and Stafford 1988).

An early cable-stayed bridge, the 1962 Maracaibo Bridge in Venezuela, has already had its cables replaced. In 1979, three of its cables completely failed due to corrosion. This failure prompted replacement of all of the cables in 1980. As of 1997, plans were being made to replace the cables a second time (Hamilton 1995; Feld and Carper 1997; Dupre 1997; Watson and Stafford 1988).

A more recent example of a stay-cable failure occurred in 1996 on the Guazú Bridge in Argentina. The structure is one of the two 1977 Zárate-Brazo Largo Bridges possessing stay cables made of high-strength, non-galvanized, parallel wires encased in cement grout within a polyethylene pipe. A combination

of corrosion and fatigue caused the rupture of one of these cables at a location approximately 8 inches (200 millimeters) from the lower anchorage. The fatigue was attributed to traffic loads exceeding design expectations and excessive, high-amplitude cable vibrations. Subsequent investigation of the remaining cables revealed significant deterioration in many of them. Damage was typically more critical at the lower anchorage than at the top anchorage. Other cables in critical danger of failure have been strengthened or replaced as necessary (Andersen, Hommel, and Veje 1999).

Excessive cable vibration is as serious a serviceability issue as corrosion. The cables of the Guazú Bridge have been observed vibrating at displacement amplitudes up to 39 inches (100 centimeters). Indentations in the polyethylene sheath exist where many of the cables exit their anchorage boxes revealing that numerous cables are vibrating at unacceptably large amplitudes. The vibrations create extreme cyclic bending stresses near the anchorage region, which becomes vulnerable to fatigue (Andersen, Hommel, and Veje 1999).

A bridge experiencing similar vibration problems is the Fred Hartman Bridge (Figure 1.8) over the Houston Ship Channel. The structure has incurred vibration amplitudes observed in excess of 40 inches (102 centimeters) peak-to-peak during its life of less than ten years. Vibrations have caused more than half of the cables' guide pipes to fracture (Weaver and Poston 1998; Poston 1998). Remediation efforts, including the current study, are underway to reduce the vibration and assess fatigue damage already sustained.



**Figure 1.8: Fred Hartman Bridge**

Photo courtesy of Dr. Suzanne Smith, University of Kentucky

Excessive cable vibrations have been observed on numerous other bridge structures, and preventative design measures are a popular topic in the literature. The many sources of cable vibration discussed in the next chapter make this design effort a challenging task. The vibration and corrosion failures discussed here may be viewed as an indication that cable-stayed bridge technology is developing too rapidly, but as with any emergent system, knowledge is often gained through failure. Each individual failure prompts the state of the technology to advance further while, concurrently, the advancing technology exposes or creates new failure mechanisms. The process inherently perpetuates itself, but this cycle is necessary for progress.

## **Chapter 2: Stay Cables and Their Vibration**

The dominating feature of cable-stayed bridges is their cable system (Figure 2.1). Not only do the stay cables form the integral part of the bridge's structural support, but the slender elements also provide the basis for the aesthetic appeal of the structural form. Stay cables have evolved just as the bridges they support have. Concern regarding corrosion of the cable's steel components has led to numerous corrosion protection schemes, and more recently, stay cables are being designed to prevent excessive vibration. The numerous mechanisms that instigate cable vibration, including buffeting, parametric excitation, vortex shedding, and rain-wind induced vibration, must be carefully considered in the design of a stay cable.



**Figure 2.1: The Stay Cables of the Fred Hartman Bridge**

## **Cables for Cable-Stayed Bridges**

Stay cables must primarily be designed to carry the tension induced by the dead load of the bridge's superstructure and the live load of vehicular traffic. This function is typically accomplished using high-strength steel. The guaranteed ultimate tensile strength of cable steel can reach 270 kips per square inch (1860 megaPascals), a value several times larger than ordinary structural steel (Gimsing 1997).

The steel component of a stay cable can take on various forms. For example, helical wire ropes (or spiral strands), locked-coil strand, parallel wire strand cable, parallel wire cable, and parallel strand cable have all been used in cable-stayed bridges in different parts of the world. Regardless of the composition of the main tension-carrying elements of a stay cable, a barrier to protect the critical steel components from a corrosive environment typically is included.

### ***Helical Wire Rope (Spiral Strand)***

Layers of helical wire are wound around a straight core with successive layers spiraled in opposite directions to form multi-wire helical strands. The twisting of the wires compared with the same wires laid straight leads to a reduced tensile strength and stiffness of the overall cable. As a result, helical wire rope is typically only used on short span bridges. This cable type is more popular for suspension bridges, and the majority of the cable-stayed bridges that have incorporated spiral strand are in the United Kingdom (Ito 1999; Gimsing 1997).

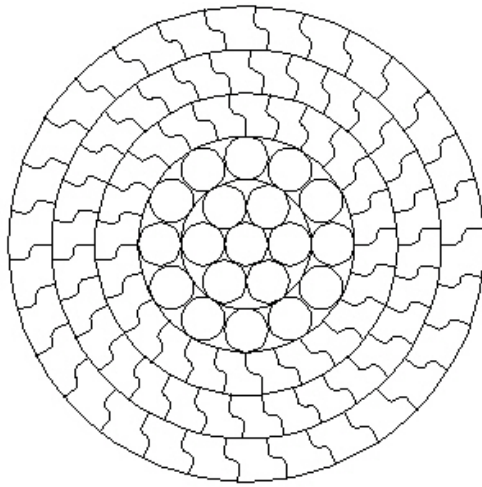


**Figure 2.2: Example Locked-Coil  
Strand Cross-Section**

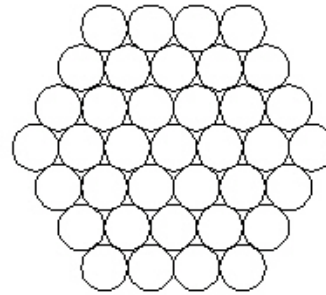


**Figure 2.3: Example Parallel Wire  
Strand Cross-Section**

### ***Locked-Coil Strand***

Locked-coil strands (Figure 2.2) begin with a core of twisted round wires very similar to helical wire rope. Unique Z-shaped wires spiral around this core, interlocking with one another to provide a solid continuous surface. The high degree of internal surface contact accompanied with the associated lack of significant internal voids allows locked-coil strand to be less sensitive to lateral pressures in locations such as saddles or anchorages. Sweden's Strömsund Bridge, the first modern cable-stayed bridge, uses locked-coil strand (Gimsing 1997; Ohashi 1991).

### ***Parallel Wire Strand (PWS)***

Spiral strand and locked-coil strand both involve twisting of the individual wire components causing decreased mechanical properties relative to straight wire components. Parallel wire strand (Figure 2.3), therefore, possesses higher

structural properties because it provides the straight wire alternative. A bundle of 0.20 to 0.28-inch (5 to 7-millimeter) diameter wires are laid parallel in a hexagonal shape to form a parallel wire strand. A stay cable may be comprised of a single large parallel wire strand, or, more likely, the cable will contain several strands grouped together (Ohashi 1991; Gimsing 1997; Ito 1999).

### ***Parallel Wire Cable (PWC)***

Parallel wire cable (Figure 2.4) is similar to parallel wire strand in that round steel wires are laid parallel to one another. However, parallel wire cables consist of a single large bundle of wires not necessarily arranged in a hexagonal cross-section. Due to the large number of wires in the grouping, a means of ensuring the parallel lay of the wires is necessary. Usually a helical strand is wrapped around the bundle (Ohashi 1991; Gimsing 1997).

A newer variation of the parallel wire cable and the parallel wire strand cable is an ultra-long lay cable generally designated as a “New PWS Cable.” These longer cables are twisted up to around  $4^\circ$  in order to facilitate installation. Additionally, the twist of the cable produces a tendency for the individual wires to group closer together when the cable is tensioned producing a beneficial self-compacting characteristic. The low angle of twist does not significantly affect the mechanical properties of the cable. The first cable-stayed bridge to use such cables was the 1986 Alex Fraser Bridge in Vancouver, Canada (Ito 1999; Gimsing 1997; Ohashi 1991).



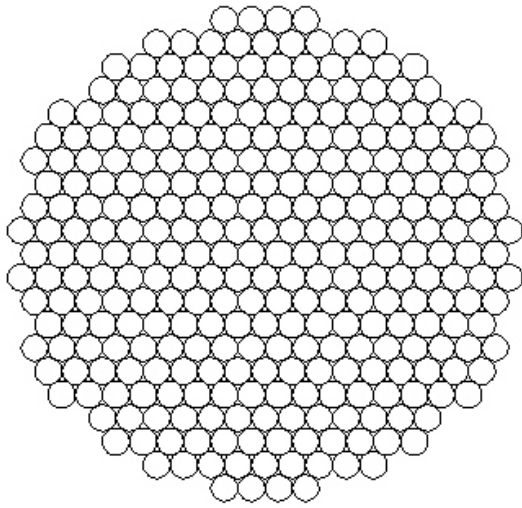


**Figure 2.4: Example Parallel Wire  
Cable Cross-Section**

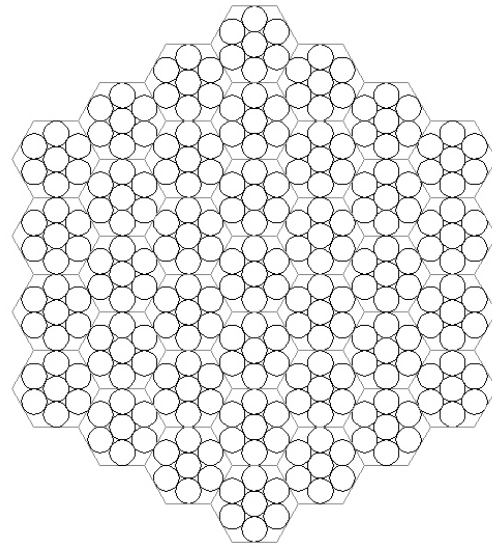


**Figure 2.5: Example Parallel Strand  
Cable Cross-Section**

### ***Parallel Strand Cable***

This stay cable variety is again similar to parallel wire cable and parallel wire strand cable. Parallel strand cable (Figure 2.5) is comprised of steel elements laid parallel to one another. However, these steel elements are not individual wires, but seven-wire strand used in prestressed concrete. Each prestressing strand is made up of six wires helically wound around the seventh wire. Each of the seven wires is similar in diameter to the individual wires of the previous stay cable types: 0.20 to 0.28 inches (5 to 7 millimeters). The seven-wire strands are arranged in a hexagonal cross-section and secured together typically by a helical strand or wire (Gimsing 1997; Ohashi 1991; Ito 1999). Parallel strand cable is common in the cable-stayed bridges of the United States.

### ***Corrosion Protection Techniques***

Locked-coil strands are typically comprised of galvanized steel. This form of corrosion protection is then covered with a protective paint. The continuous outer surface created by a locked-coil strand makes the painting of the cable easier and more efficient (Gimsing 1997; Ohashi 1991). Wire ropes are also typically zinc-galvanized and additional voids between the wires are sealed (Ito 1999).

Use of galvanized steel is a common corrosion protection technique among all of the other stay cable forms as well, but additional methods are generally used. There are many corrosion prevention techniques available, but one of the most popular for parallel wire strand cable, parallel wire cable, and parallel strand cable involves containing all of the steel elements within a sheath (Figure 2.6). Once the stay cable has been installed as part of the bridge structure, the steel load-carrying elements are encased by cementitious grout injected into the sheath. In the past, this sheath has been made of a thin steel pipe, but today, weather resistant black polyethylene is used commonly. Due to the vulnerability of polyethylene to ultraviolet light, a final, protective layer is normally included to prevent damage. Often, this visible layer of the stay cable is selected to be a lighter color for aesthetic reasons based on the bridge's surroundings. The lighter color also reduces thermal fluctuations that the black polyethylene might otherwise experience. This final layer may consist of a polymer extrusion, a complex painting routine using specially developed primer coatings for

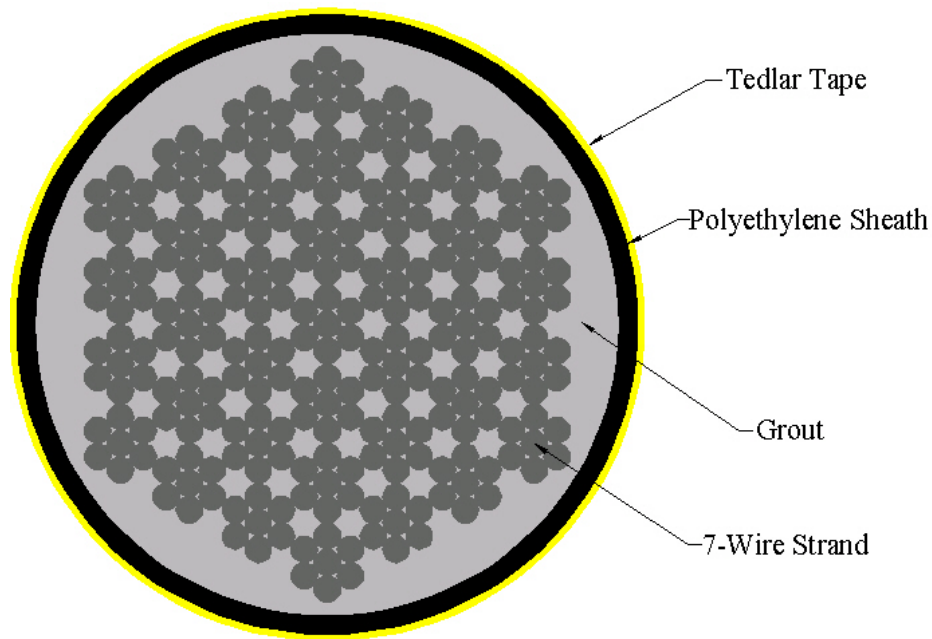


**Figure 2.6: Example Cross Section of Grouted Stay Cable**

polyethylene, or PVF Tedlar tape wrapped around the cable (Gimsing 1997; Ohashi 1991; Ito 1999).

Theoretically, the grouted cable corrosion protection scheme should provide the load carrying steel with a dual barrier from a corrosive environment. Recent tests at the University of Texas at Austin by Hamilton (1995) have indicated that this belief may not be true. Hamilton found that wherever the polyethylene sheath was breached, the grout contained fine cracks attributed to either traffic load or shrinkage encouraged by the exposure to air that was provided by the breach in the sheath. This discovery has spawned concern over the adequacy of corrosion protection systems for stay cables (Hamilton 1995).

## **Cable Vibration Mechanisms**

Just as stay cables are designed to prevent corrosion, they are also being designed more and more to prevent excessive vibration. Vibration of a stay cable may be initiated by numerous phenomena, to be discussed below, including vortex shedding, galloping, buffeting, wake effects, parametric excitation, and rain-wind induced vibration. The numerous mechanisms of stay cable vibration make its prevention a complicated design challenge, but stay cable technology is continually evolving to meet that challenge.

### ***Vortex Shedding***

Smooth airflow around a cross-section produces vortices shedding off of a stay cable (Figure 2.7). Consecutive vortices shed off of opposite sides of the cross-section producing alternating forces, perpendicular to the wind direction, that induce vibration. When the frequency of the vortex shedding matches any of a stay cable's natural frequencies, perceptible levels of vibration occur. An increased wind speed increases the shedding frequency, but wind turbulence

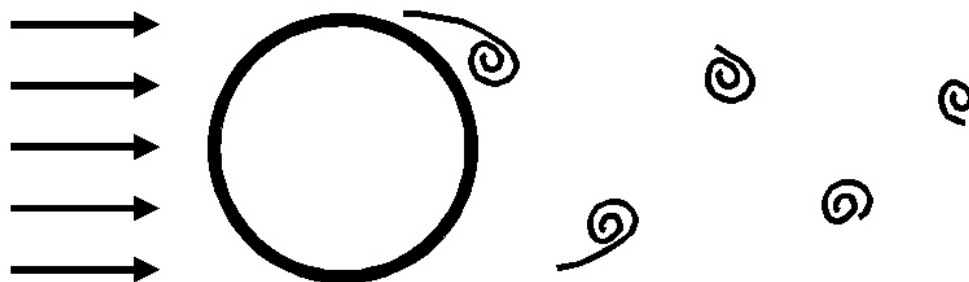


**Figure 2.7: Vortex Shedding**

serves to reduce the vibration mechanism. For smooth flow, vortex shedding typically excites a stay cable's higher modes of vibration (Virlogeux 1998; Ito 1999).

### ***Galloping***

Galloping is vibration perpendicular to the wind direction caused by aerodynamic instability. Lift forces created by airflow around an unsymmetrical cross-section initiate the lateral movement that leads to vibration. Stay cables are generally circular, limiting the presence of galloping under normal conditions. However, cross-section irregularities such as ice can make the section unsymmetrical and, thus, vulnerable to galloping. Additionally, oblique wind directions may cause a circular cross-section to appear elliptical, introducing the possibility for galloping without section irregularity (Virlogeux 1998; Ito 1999).

### ***Buffeting***

Turbulent, high-speed wind conditions create a complicated environment with sizeable forces and significant pressures that will influence any flexible structure. Buffeting can be used to describe the excitation of stay cables due to these random loads. Buffeting differs from other vibration mechanisms in that it does not deal with an aerodynamic or resonant phenomenon; it is simply the result of high loads, rapidly changing with time, that happen to be introduced by wind (Virlogeux 1998; Ito 1999; Wardlaw 1991).

### ***Wake Effects***

The vortices that shed off of bodies in the flow of wind produce more effects than the vortex shedding phenomenon described earlier. Cables in the

wake of a shedding body are disturbed by the turbulent vortices as well. Just as the vortices shed periodically, they also impact a downstream cable periodically, potentially initiating vibration. Several scenarios for this mechanism exist on a cable-stayed bridge. Vortices shedding off of one of the pylons may influence neighboring cables. Vortices from the cables in one plane of stays may affect the stay cables in another plane. Similarly, if the wind direction is parallel to a plane of stays, vortices shedding from one cable may disturb the next downwind cable (Virlogeux 1998).

### ***Parametric Excitation***

Movement or vibration of one of a stay cable's anchorages may also cause vibration of the cable. Termed parametric excitation, this mechanism may be induced by structural vibration of the bridge's pylon, deck, or both. Pylon and deck vibration may be achieved through many of the methods described for the individual cable. One unique source of vibration, though, is traffic loading of the deck. For example, a train passing over a cable-stayed bridge may impart a periodic load on the deck prompting structural vibration, which then generates vibration of the stay cables through the anchorages. Parametric excitation may be avoided during design through careful separation of the natural frequencies of the bridge's components (Gimsing 1997; Virlogeux 1998).

### ***Rain-Wind Induced Vibration***

Within the last fifteen years, the most dominant mechanism of stay cable vibration that has been discussed in the literature and has been the focus of researchers and designers is rain-wind induced vibration. The phenomenon

surfaced in 1984 with the then inexplicable, large-amplitude vibration of the stay cables of Japan's Meikonishi Bridge while it was under construction. The mysterious vibration then began appearing on other cable-stayed bridges around the world. Previously known mechanisms of vibration were all eliminated from consideration mostly due to the large amplitude of vibration, and similarities among the dynamic incidents were noted. The vibration usually takes place on bridges with polyethylene-sheathed cables set in flat landscapes near a large body of water. Typically, a wind speed of 10 to 45 miles per hour (5 to 20 meters/second) produces cable vibrations in the frequency range of 1 to 3 Hertz. Most importantly, rain is always present (Pacheco and Fujino 1993).

Eventually the mechanism of rain-wind induced vibration was established. In short, rainwater streaming down a smooth stay cable forms one or more rivulets that alter the cable's aerodynamic profile. In combination with wind forces, this altered profile can experience large amplitude oscillations. As the cable vibrates, the rivulet or rivulets oscillate at the same frequency as the cable, continuously changing the cable's cross-section and maintaining the vibration (Figure 2.8). The formation of rivulets is the key to the vibration mechanism. Therefore, the phenomenon can occur even in light rain. Further, heavy wind can blow the water off of the cable preventing rain-wind induced vibration. The

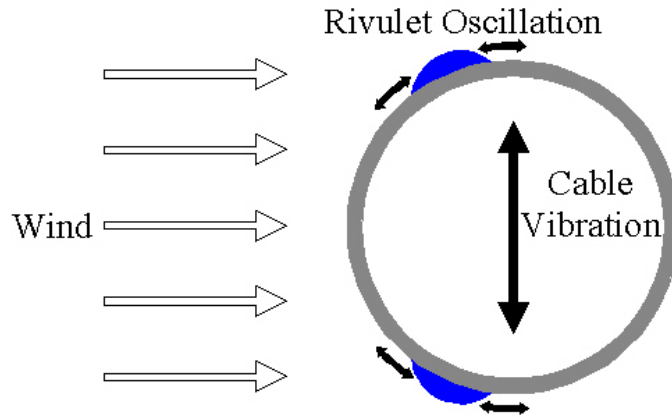


**Figure 2.8: Rain-Wind Induced Vibration**

severity of this form of cable movement lies in the typically large displacements that are produced. Stay cables are tested for axial fatigue, but they are not fatigue tested for the bending of the magnitude observed during rain-wind induced vibration.

It initially was believed that rain-wind induced vibration could only occur on cables that inclined downward into the wind. Rainwater rivulets, forming on the upper and lower sides of the cable, oscillate, causing vibration. Wind tunnel tests indicated that formation of the rivulet on the upper (windward) side of the cable was essential for the mechanism to cause vibration (Hikami and Shiraishi 1988). More recent publications such as Virlogeux (1998) and Miyazaki (1999) have promulgated the necessity of the upper rivulet. However, reports such as in Verwiebe (1998) of rain-wind induced vibration on nearly vertical members have led to a closer look at the phenomenon.



Depending on the location of the rivulets and the direction of the cable vibration, there are three different mechanisms of rain-wind induced vibration described in the literature (Verwiebe 1998). The first mechanism involves vibration of the cable parallel to the wind direction. Two rivulets formed on the leeward side of the cable oscillate symmetrically in their own quadrants. The other two mechanisms deal with vibration of the cable mostly perpendicular to the wind direction and are detailed in Verwiebe (1998). The major principal of oscillating rainwater rivulets remains the same for all variations of rain-wind induced vibration. The implication that rain-wind induced vibration theoretically may cause a cable to vibrate in more than one plane makes the task of mitigating the motion more complex.

### **Mitigation Techniques for Rain-Wind Induced Vibration**

When choosing the appropriate mitigation technique, many factors must be considered such as aesthetic appeal, efficacy, lifespan, and cost. It is important to bear in mind other types of vibration when trying to prevent one specific mechanism. For example, a design intended to control rain-wind induced vibration may worsen the effect of vortex shedding. Often, the chosen mitigation technique represents a compromise of all of the factors involved. Methods of stay cable vibration control may be classified into three general categories: structural, mechanical, or aerodynamic (Yamaguchi and Fujino 1998).

### ***Structural Mitigation Techniques for Rain-Wind Induced Vibration***

Structural mitigation involves the addition of structural elements to the design to restrain vibration. Cable restrainers or cross ties are commonly used to connect adjacent cables to one another (Figure 2.9). The cable restrainers stiffen the stay cable system and allow vibration energy from one cable to be transferred to others. The cross ties generally prevent a single cable from vibrating in a low mode. However, a single stay cable may still vibrate at higher modes, or the plane of stays may still vibrate as a unit. Overall, though, this technique has been successful at reducing rain-wind induced vibration. Nevertheless, this form of structural mitigation is not considered aesthetically pleasing and is expensive to maintain. Therefore, cable restrainers are used often only as a temporary control device (Yamaguchi and Fujino 1998; Virlogeux 1998; Bournand 1999).



**Figure 2.9: Cable Restrainers on the Fred Hartman Bridge**

### ***Mechanical Mitigation Techniques for Rain-Wind Induced Vibration***

Mechanical mitigation typically entails increasing the damping of a vibrating stay cable. This augmentation is commonly accomplished with a viscoelastic or hydraulic damper between the bridge deck and the cable. It is believed that even 0.5% damping will limit the cable oscillations. Because rain-wind induced vibration has the potential to excite motion in any plane, a single linear damper may not be an adequate remediation. Therefore, ring dampers have also been used that are installed around the circumference of the cable and bear against a guide pipe or something similar (Yamaguchi and Fujino 1998; Virlogeux 1998; Bournand 1999). New damper technologies, including controllable fluid dampers used to semiactively control the damping, are continually being developed (Johnson *et al.* 1999).

### ***Aerodynamic Mitigation Techniques for Rain-Wind Induced Vibration***

Aerodynamic mitigation focuses on the prevention of rain-wind induced vibration rather than its control as structural and mechanical techniques attempt to do. If the rivulets of rainwater may be prohibited from forming, the entire vibration mechanism may be halted. Poston (2000) suggests that rain-wind induced vibration has only surfaced within the last fifteen years due to the introduction of polyethylene sheaths wrapped with smooth tape. Previously, steel pipe was commonly used. Poston believes that the inherent rust on steel pipe was enough of a surface irregularity to break up any water rivulets and prevent rain-wind induced vibration (Poston 2000).

Elimination of the smooth, continuous cable surface is the dominant form of aerodynamic mitigation. The cables of Japan's Tataro Bridge are dimpled like a golf ball. Other bridges have used gear-shaped cross-sections or U-shaped grooves to channel water and prevent rivulet movement (Virlogeux 1998; Yamaguchi and Fujino 1998). Another variation is placement of a helical strake winding down the length of the cable, but the efficacy of this method has been questioned in the literature (Verwiebe 1998). Researchers at Texas Tech University are experimenting with an aerodynamic damping method consisting of a series of rings fastened around a stay cable to prevent rivulet formation (Sarkar and Gardner 2000).

Mitigation techniques for rain-wind induced vibration continue to develop because the problem has yet to be completely solved. Despite the introduction of the phenomenon in 1984, not all cable-stayed bridge designs since that time have taken the vibration mechanism into account. Two such bridges currently facing remedial efforts are the Veterans Memorial Bridge and the Fred Hartman Bridge. These bridges are the focus of the next chapter.

## **Chapter 3: Cable-Stayed Bridges of Texas: Vibration and Remediation History**

The state of Texas currently maintains two cable-stayed bridges: Veterans Memorial Bridge near Port Arthur and the Fred Hartman Bridge near Baytown. Both of these structures are experiencing problems with excessive cable motion. The mechanism of excitation has been identified as rain-wind induced vibration, and remediation has been a major focus of the Texas Department of Transportation. This research endeavor and, therefore, this chapter focus on the Fred Hartman Bridge.

### **Veterans Memorial Bridge: Background and Vibration History**

Veterans Memorial Bridge (Figure 3.1), completed in 1991, carries a 640-foot (195-meter) main span across the Neches River. Fifty-six stay cables in a harped configuration transfer the load from the externally post-tensioned, precast concrete box girder superstructure to four vertical concrete towers. Cable

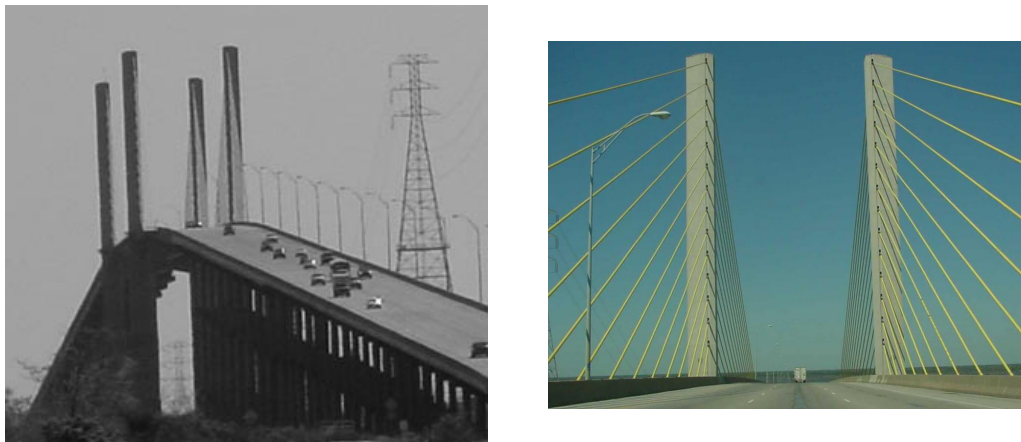


**Figure 3.1: Veterans Memorial Bridge**

vibrations were first observed during construction prior to grouting of the cables. By 1995, many of the steel band clamps that attach the neoprene boots to the steel guide pipes had failed due to cable vibration, thermal movement, or a combination of the two. Repairs were made, but vibration has continued (Weaver and Poston 1998).

### **Fred Hartman Bridge: Background**

The Fred Hartman Bridge (Figure 3.2), completed in 1995, carries a 1250-foot (381-meter) main span across the Houston Ship Channel between La Porte and Baytown. This main span is comprised of twin composite concrete decks supported by steel girders. Two planes of forty-eight stay cables, in a fanned arrangement, suspend each 78-foot (24-meter) wide deck. In all, 192 stay cables in four separate planes (Figure 3.3) transfer the deck load to four diamond-shaped concrete towers (Weaver and Poston 1998).

### **Cables of the Fred Hartman Bridge**

The Fred Hartman Bridge's stay cables consist of parallel strand cable using 0.6-inch (15-millimeter) diameter prestressing strand grouted inside of a black polyethylene pipe sheath. The bundle of prestressing strands is wound with a 0.25-inch (6.4-millimeter) diameter spacer, helically wound with a pitch of 3 feet (0.91 meter). The final visible layer on each cable is a wrap of yellow Tedlar tape. The smallest stay cables are those nearest the pylons and contain twenty



**Figure 3.2: The Fred Hartman Bridge**



**Figure 3.3: The Fred Hartman Bridge from South Pylon**

prestressing strands within a 4.5-inch (114-millimeter) diameter pipe. The largest cables are the backstays farthest from the pylons and contain sixty-one strands within a 7.6-inch (194-millimeter) diameter pipe.

In all, the Fred Hartman Bridge's 192 stay cables are classified into eight sets of twenty-four cables, numbered from the backstay farthest from a pylon (cable 1) to the forestay farthest from a pylon (cable 24). The shortest cables are, thus, cables 12 and 13, nearest a given pylon. Additionally, the four planes of stays are identified with letters A through D. The A plane of stay cables is nearest the Gulf of Mexico, while the D cable plane is inland. Further, the cables anchored to the pylon nearest the north (Baytown) approach are designated with an *N*, and the cables anchored to the pylon closest to the south (La Porte) approach are distinguished with an *S*. In this way, the forestay cable farthest from and anchored to the south pylon, in the plane of cables facing the Gulf of Mexico, is labeled stay cable A24S.

Each cable has a constant free length diameter, which then becomes larger at the anchorages (Figure 3.4 and Figure 3.5). At the anchorage, each strand is secured into an anchor head or anchorage plate with wedges. The larger diameter of pipe at the anchorage is referred to as the anchorage region and contains the strand profile that reduces the arrangement of the strands into a compact configuration. A tension ring is positioned at the beginning of the free length that facilitates the transition of the strands into this compact arrangement. A steel anchorage box and a steel guide pipe enclose each cable's anchorage region and



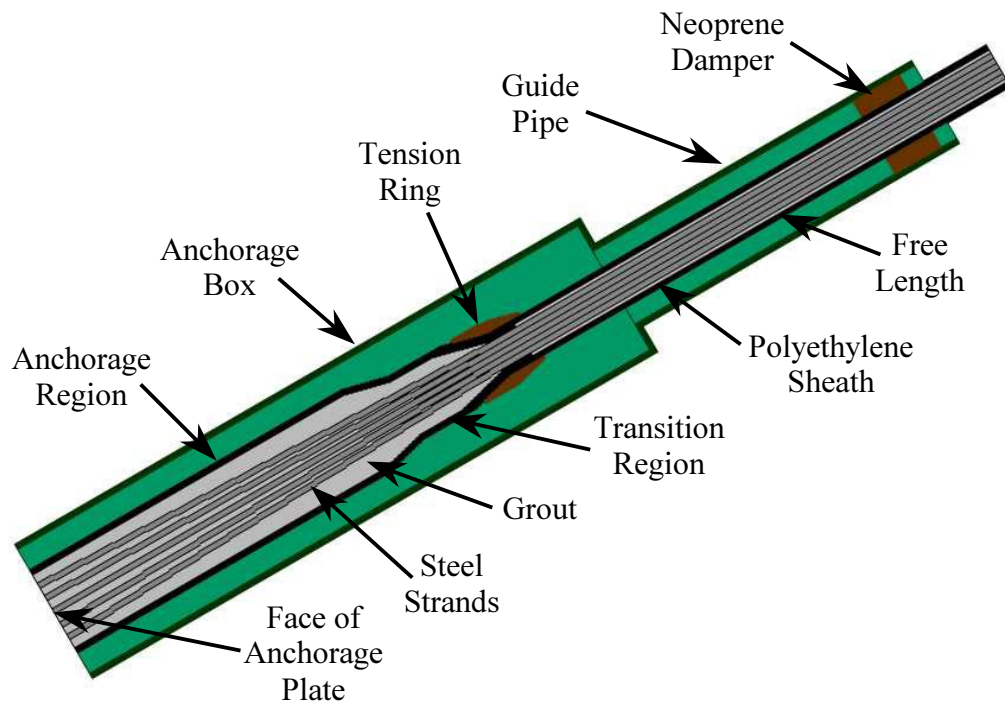


**Figure 3.4: Cross Section of Typical Stay Cable Anchorage**

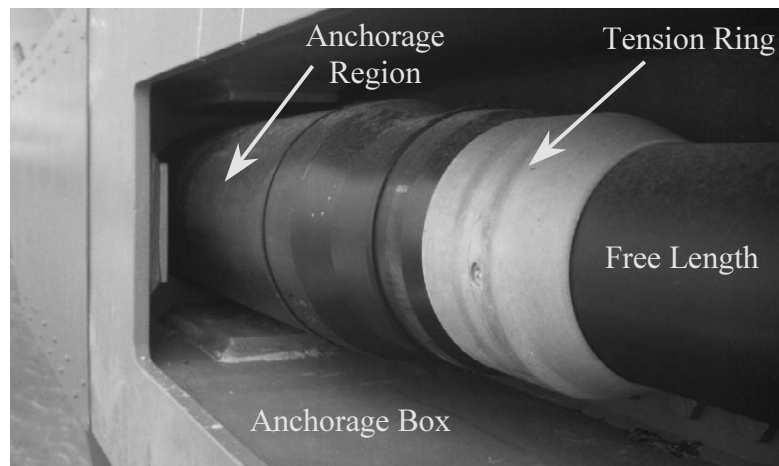


**Figure 3.5: Typical Stay Cable Anchorage Transition**

the lower portion of the free length. The end of the guide pipe contains a neoprene damper designed to minimize high-frequency vibration.

### **Stay Cable Vibration History of the Fred Hartman Bridge**

Just as with Veterans Memorial Bridge, cable vibrations were first observed on the Fred Hartman Bridge during construction. Repair of thirty-five steel guide pipes was required before the bridge opened for traffic in September of 1995. After the structure's opening, large-amplitude, low-frequency cable vibrations continued, prompting the installation of a cable restrainer system in January of 1996. By April of 1997, thirty-seven additional guide pipes had fractured along with the fatigue failure of seven cable restrainers, including one that fell to the bridge deck. As a result, the cable restrainer system was removed. Shortly thereafter, large amplitude vibrations were documented (Table 3.1) and videotaped (Figure 3.6). Cable 24, vibrating in the third mode, provided the largest observed, peak-to-peak, displacement amplitude estimated at 42 inches (1070 millimeters) (Weaver and Poston 1998).

In general, the large-amplitude vibrations that have been observed on the bridge have been in one of the first three modes of vibration corresponding with the three lowest natural frequencies, all less than 2 Hertz. The characteristics of these vibrations, including the conditions in which they occur, suggest rain-wind induced vibration as the mechanism. The neoprene dampers installed at the end of each cable's guide pipe were designed to mitigate low-amplitude, high-frequency vibrations expected from phenomena such as vortex shedding and

**Table 3.1: Large-Amplitude Vibration Events on the Fred Hartman Bridge  
(Weaver and Poston 1998)**

Date	Cable ID	Primary Mode of Vibration	Frequency (Hz)	Estimated Peak-to-Peak Amplitude (in)
April 3, 1996	1, 2, 3	1	0.8	25
April 3, 1996	10, 11	2	>1.5	4
April 4, 1996	15, 16	1	1.0	12
April 4, 1996	23, 24	2	1.2	26
April 4, 1996	24	3	1.8	42



**Figure 3.6: Peaks of Motion from a Video of Vibration of Cable A24S on the Fred Hartman Bridge**

Video courtesy of WDP

buffeting. Ideally, the neoprene damper system should lessen the magnitude of the cyclic bending stresses incurred at the anchorage. By July of 1997, however, rain-wind induced vibration had contributed to the failure of 101 of the total of 192 guide pipes (Figure 3.7) (Weaver and Poston 1998; Poston 1998).

### **Evaluation and Repair of Stay Cable Vibrations on the Fred Hartman Bridge**

Whitlock Dalrymple Poston and Associates (WDP) have been retained by the Texas Department of Transportation to head a team of researchers from several universities in the investigation of the cable vibration problems and proposal of repair techniques. WDP's primary concerns include eliminating the effects of rain-wind induced vibration from the Fred Hartman Bridge and assessing the damage already inflicted upon the structure by any unanticipated stress at the anchorages of the vibrating cables.

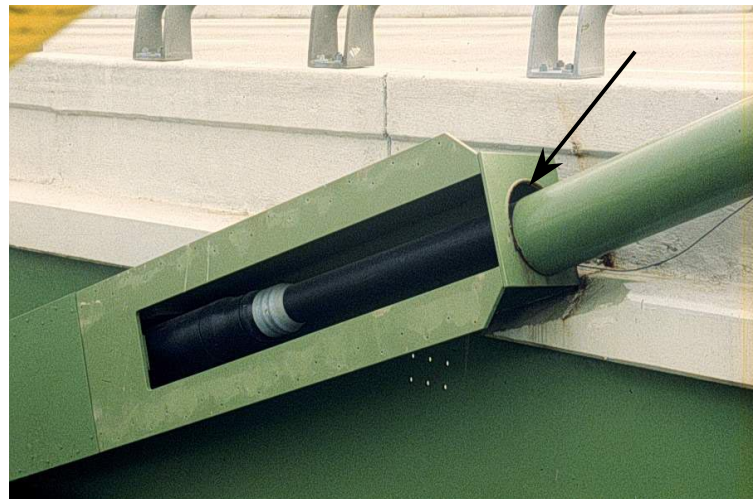


**Figure 3.7: Failed Connection of Guide Pipe to Anchorage Box**

### ***Structural Repair***

In an effort to control the vibrations temporarily, a second cable restrainer system was designed and installed. A principal design flaw of the first restrainer system that prompted its removal was the potential for failed pieces of the restrainer structure to fall to the bridge deck, risking injury to motorists. WDP corrected this flaw on the second design to allow failed pieces simply to slide down the nearest cable. The design of the guide pipes was also retrofitted to include stiffeners (Figure 3.8). These stiffeners were intended to allow the guide pipe to withstand the large lateral forces produced by the cable vibration (Weaver and Poston 1998; Kesner and Poston 1999).

While the stiffeners do allow the guide pipe to better resist excessive cable vibration, they do not prevent or control the vibration itself. Additionally, the cable restrainer system is designed to be temporary. Therefore, a permanent solution to the problem of rain-wind induced vibration on the Fred Hartman

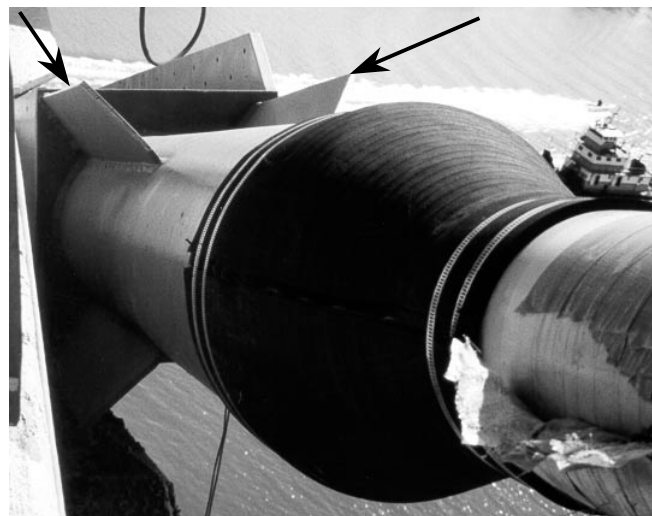


**Figure 3.8: Retrofit Stiffeners on Guide Pipe**

Bridge has yet to be realized. Researchers at WDP and at universities including Johns Hopkins University, Texas Tech University, and the University of Kentucky are working on a variety of topics aimed at providing such a solution.

### ***Instrumentation and Characterization of Cable Vibration***

Johns Hopkins University has assumed the task of characterizing the vibration on the bridge through a large array of full-scale measurements. Instrumentation including accelerometers installed on stay cables and the bridge deck, displacement transducers installed on cables, and weather stations at deck level and on the top of one of the pylons, have provided thousands of five-minute data sets, recorded on a data acquisition system inside of one of the pylons. Each record is triggered by an acceleration, displacement, or wind event that exceeds a given starting threshold. Using these records, Johns Hopkins University was able to establish correlations between parameters such as the severity of a vibration event, the amount of rainfall, wind speed, and wind direction. These data records also provide invaluable information to those experimenting with prototypical dampers as a means of mitigating cable vibration (Main and Jones 2000).

### ***Mechanical Mitigation Efforts***

WDP has developed two prototypical mechanical dampers as possible long-term vibration control devices. The first type is a linear damper attached perpendicular to the cable and connected to the bridge deck (Figure 3.9). The device's damping coefficient was established based on the cable's natural frequency, mass, length, and damper location relative to the cable anchorage. The second prototype damper was designed by the Freyssinet Company and surrounds



**Figure 3.9: Prototype Linear Damper**



**Figure 3.10: Prototype Freyssinet Damper**

the cable with a pressurized bladder system (Figure 3.10). The particular cable's characteristics define the bladder's pressure and flow metering properties. The bridge instrumentation maintained by Johns Hopkins University is being used to determine the efficacy of these prototype dampers (Kesner and Poston 1999).

### ***Aerodynamic Mitigation Efforts***

As discussed in Chapter 2, mechanical vibration mitigation techniques, such as the dampers described above, and structural vibration mitigation techniques, such as cable restrainers, aim to control excessive stay cable vibrations. Aerodynamic mitigation focuses on the prevention of a particular vibration mechanism. In the case of the Fred Hartman Bridge, Texas Tech University is developing a type of aerodynamic damper to prevent rain-wind induced vibration. The damper system consists of circular rings placed around a stay cable. The diameter of the tube comprising the ring is approximately a fourteenth of the diameter of the stay cable to which it will be applied. The rings are wrapped around a stay cable at a spacing equivalent to two to four diameters of the stay cable to which it will be applied. The rings are designed to prevent the

formation of the rivulet of rainwater that is vital to the mechanism for rain-wind induced vibration. Wind tunnel tests have indicated promising results, but the aerodynamic dampers have yet to be tested on an actual bridge structure (Sarkar and Gardner 2000).

### **The Role of The University of Texas at Austin in the Vibration Investigation of the Fred Hartman Bridge**

While establishment of a permanent solution to the problem of rain-wind induced vibration on the Fred Hartman Bridge is a central goal, assessment of the damage the bridge's cables have already sustained is just as critical. This objective is the primary issue with which The University of Texas at Austin is concerned.

#### ***Bending Fatigue***

Typically, stay cables are rigorously tested in the laboratory to discern their resistance to axial fatigue under the cyclic tensile load that is characteristic of the load that bridge traffic would produce in the cables of a completed structure. Normally, however, bending fatigue is not considered because, in design, cables are considered perfectly flexible. Designed to carry tension only, a cable possesses slenderness that causes any moment, and associated bending stress that accrue, to be considered negligible. This assumption is largely a valid one, but applications do exist where the assumption fails to be prudent (Dowd and Thatcher 2000).



One such application is the fixed anchorage of a stay cable exposed to excessive vibration. A stay cable anchorage is designed to align with the catenary shape produced by its cable's self-weight so that ordinary service will not produce excessive flexural stress in the anchorage region of the cable. The anchorage region of a stay cable, however, is not designed to withstand the cyclic bending stress produced by the excessive cable vibrations observed on the Fred Hartman Bridge.

When considering the overall bending fatigue of a stay cable, several key locations and mechanisms arise. Fretting fatigue is the dominant mechanism of concern. The relative slip of two metal surfaces that bear against one another can produce damage known as fretting fatigue. An abrasive oxidation product forms between the two surfaces that exacerbates the deterioration of the metal surfaces.

Any two adjacent wires, belonging to the same strand or neighboring strands within a stay cable, may slide against one another, especially at the center of the cable where the shear is the highest, fostering this type of fatigue. The tension ring is another major location of concern as the outer strands bear against the tension ring. Along the free length, the only real danger of fretting fatigue lies in the contact between the outer strands and the helical spacer strand. At any of the critical locations, the surface damage caused by fretting fatigue may propagate into wire breaks that reduce the load-carrying cross-section of the cable at that point.

In addition to producing the potential for fretting fatigue, high cycles of bending stress raise questions about the condition of the grout within a stay cable.

Cracked or even pulverized grout could seriously decrease the bending stiffness of a cable along with leaving the steel strands more susceptible to a corrosive environment. Finally, the anchorage components must endure similar bending stress cycles as the cable, testing the limits of the anchorage design. At the anchorage plate, each strand is gripped by tapered wedges that form notches in the strand. These areas of stress concentration are susceptible to axial fatigue damage.

### ***Plan for Assessment of Bending Fatigue Damage***

To assess the extent of bending fatigue damage to the stay cables of the Fred Hartman Bridge, The University of Texas at Austin is executing a scope of work consisting predominantly of four major tasks. First, visual field inspection of certain cables reveals the extent of damage. Second, field measurements of extreme grout fiber strains during vibration events and during ordinary traffic events allow comparison between the two, providing insight into the relative severity of the vibration events. Third, an analytical model of a given stay cable relates cable motion to fatigue stress ranges. Last, laboratory bending fatigue tests allow the establishment of a correlation between attainable data, such as observed displacements and measured strains or accelerations, and the fatigue life of the cable. In this manner, a set of procedures for evaluating stay cable fatigue damage is established (Dowd *et al.* 2001).

### ***Visual Field Inspection***

Grouted stay cable systems are difficult to inspect for fatigue damage because the load-carrying steel strand is not visible. Rather than compromising

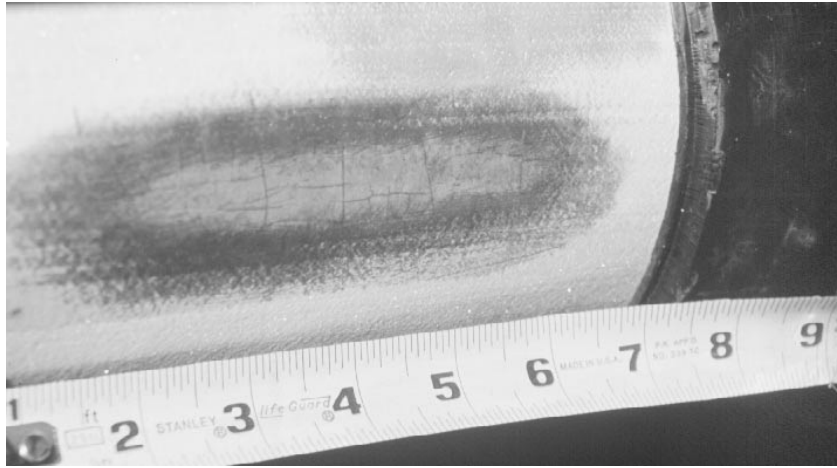


**Figure 3.11: Inspection of Grout in Anchorage Region**

the corrosion protection system, visual field inspection consisted of cutting a small window in the polyethylene sheath to make an observation of the grout. The sheath was promptly patched following each inspection. Three stay cables, all of which have experienced large-amplitude vibrations, have been inspected in such a manner. No pulverized grout was found, but fine, intersecting cracks with a spacing of 0.5 inch (12 millimeter) to 0.75 inch (19 millimeter) were found in all inspected locations (Figure 3.11).

An inspection of the exterior of the polyethylene pipe was also conducted at the location where the cable exits the anchorage box and enters the guide pipe (Figure 3.12). For the estimated displacement amplitudes of Table 3.1 to be accurate, damage to the polyethylene pipe in this area of minimal clearance was expected. For cables A24N, A24S, and A23S, indentations were found that go all the way around the pipe (Figure 3.13). Each depression is consistently deeper on

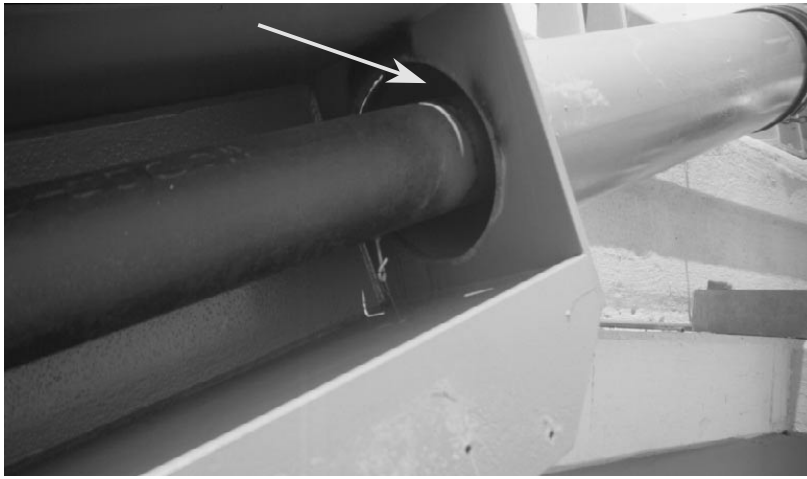


**Figure 3.12: Location of Polyethylene Sheath Inspection**



**Figure 3.13: Indentation in Polyethylene Sheath at Anchorage Box**

the top of the pipe. This damage is consistent with the banging of the cable against the anchorage box opening, occurring during large amplitude vibrations following the failure of the guide pipe. Damage to the polyethylene on the sides of the sheath indicates that the cable motion was not confined to the plane of stay cables.

### ***Field Strain Measurements***

Multiple strain gages have been attached to the exterior grout surface of several stay cables over the past few years in order to measure ambient traffic response (Figure 3.14). A sample of these data is shown in Figure 3.15. The plot shows strain from four strain gages applied around the circumference of the cable at approximately the same distance along the cable's length. The four gages shown were installed on the top, bottom, inside, and outside of the cable (Figure 3.16). Each of the four gages provides a similar strain history, indicating that the cable was acting predominately as an axial member. If the cable had been



**Figure 3.14: Strain Gage Applied to Grout Surface**

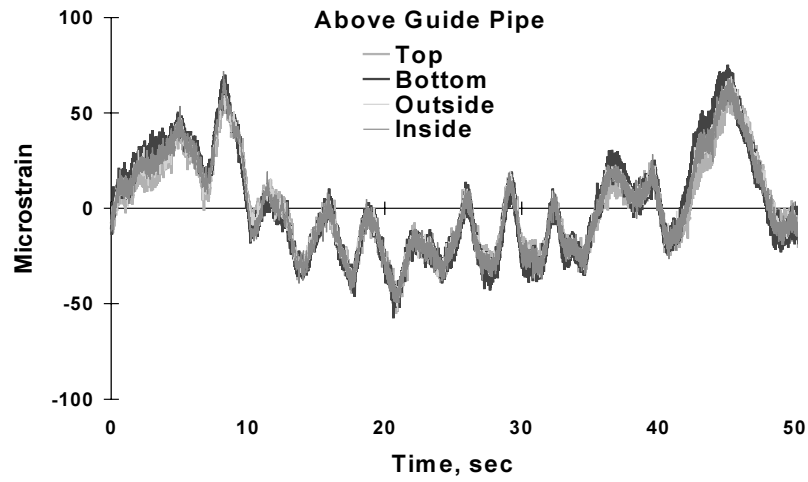


**Figure 3.15: Sample Strain Data Produced by Ambient Traffic Response**

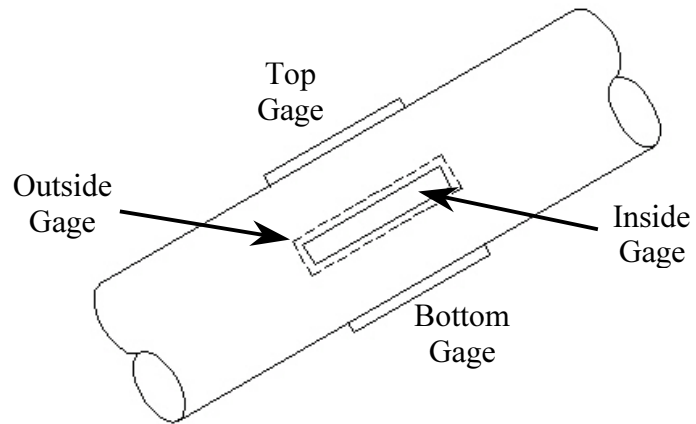


**Figure 3.16: Stay Cable Strain Gage Locations**

vibrating parallel to the plane of stays (up and down), the top and bottom gages would reflect strain fluctuations in opposite directions while the inside and outside gages would still only reflect the traffic data. This response would be justified by beam theory. As the cable bends into positive curvature during vibration, the top of the cable goes into compression while the bottom goes into tension. The inside and outside gages do not reflect significant bending strain because they are positioned near the neutral axis.

Strain data records in The University of Texas at Austin's inventory prior to November of 1999 do not include information from a significant rain-wind induced vibration event. Attempts to acquire reliable strain data from a significant vibration event are a major focus of this study.

### ***Analytical Modeling of Stay Cables***

Willox (1998) performed a series of analyses on cable A24S. In the first analysis, the cable was idealized as a taut string incorporating the work of Irvine (1993) on local bending stress near the terminations. This analysis, however, did not include the variance in cross section in the anchorage region. An upper and a lower bound for extreme-fiber grout and steel stresses were established by first using the free length properties uniformly along the entire length of the cable and then using the anchorage section properties along the entire length in the same manner. The grout stress at the anchorage, determined from the analysis, is bound between 13.5 (93.0) and 3.14 kips per square inch (21.6 megaPascals), and the grout stress at the tension ring is bound between 0.154 (1.06) and 0.653 kips per

square inch (4.50 megaPascals). These numbers are higher than those expected (Willox 1998).

Next, Willox (1998) created a finite element model of cable A24S using ABAQUS. This model, established using transformed section properties, dynamically represented a vibration event equivalent to the maximum event observed for cable 24 (see Table 3.1). Results for extreme-fiber grout and steel stresses were again higher than expected when the inspection of the cable was considered. The maximum extreme-fiber grout stress was 13.3 kips per square inch (91.6 megaPascals) at the anchorage for the maximum displacement amplitude; the grout used in the cable is expected to crack in tension at 0.4 kips per square inch (3 megaPascals) (the modulus of rupture). A comparison of these stress levels indicates that, based upon the finite element model, the grout inspection should have revealed a much more deteriorated condition of grout. Because of this significant difference between computed and observed results, attempts to duplicate and refine this finite element model, along with the creation of supplementary finite element models for additional cables, are another major focus of this research.

### ***Laboratory Bending Fatigue Testing***

Central to the efforts of The University of Texas at Austin is the execution of bending fatigue tests at Ferguson Structural Engineering Laboratory. At least four specimens, full scale in cross section and anchorage detail, will be fatigue-tested with a cyclic, lateral load at the specimen's mid-length. The last major



focus of this study is the design of an initial test specimen based upon parameters drawn from a model of an actual Fred Hartman Bridge cable.

The research objectives of the University of Texas at Austin all aim at assessing the extent of the bending fatigue damage already incurred by the stay cables of the Fred Hartman Bridge. Correlating observed displacements and measured strains or accelerations to the fatigue life of a stay cable is paramount in this evaluation. The establishment of a set of procedures for evaluating stay cable fatigue damage will allow the condition of every cable on the Fred Hartman Bridge, and possibly others, to be identified, reliably predicting the current lifespan of individual bridge cables.

## **Chapter 4: Measurement of Strain on the Stay Cables of the Fred Hartman Bridge**

As discussed in Chapter 3, strain data records in The University of Texas at Austin's inventory prior to November of 1999 did not include information from a significant rain-wind induced vibration event. Multiple records, however, containing a stay cable's ambient response to bridge traffic had been obtained. These traffic records were required to ascertain the relative severity of the strain data recorded from vibration events, but before any such comparison could be made, strain data from a vibration event had to be collected. Since November of 1999, multiple attempts had been made to acquire such data using two different strain gage types, varying gage application procedures, and two independent data acquisition techniques.

### **Primary Strain Acquisition Attempts**

Previously, a mobile data acquisition system had been used to collect traffic strain data during field visits to the bridge, but this data acquisition system could not be left unattended to capture strain data from a vibration event during light wind and rain. Therefore, in November of 1999, instrumentation to facilitate the unsupervised collection of strain data was installed on the Fred Hartman Bridge. The instrumentation linked strain gages with the data collection system maintained by Johns Hopkins University as discussed in Chapter 3. The data acquisition unit was housed within the southeast pylon (Figure 4.1). For research



**Figure 4.1: Data Collector Maintained by Johns Hopkins University Inside the Southeast Pylon**

purposes, cables A24S, A23S, and A22S were not tied into the cable restrainer system, leaving them free to vibrate in any mode. Consequently, these cables were the only ones where strain measurements were relevant for this study. The large distance between the strain gages and the data acquisition system presented a problem to be accounted for in the strain collection instrumentation installed on the bridge.

#### ***Strain Collection Instrumentation***

The unrestrained cables reached the bridge deck over 500 feet (150 meters) from the pylon that housed the data acquisition system. The resistance inherent in 500 feet (150 meters) of wire will reduce the signal from the strain gage, making it difficult to detect.

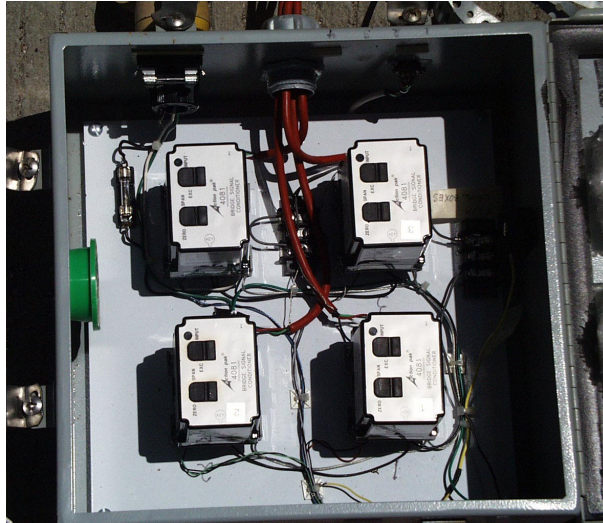


**Figure 4.2: Four Signal Conditioners Mounted in a Box**

To circumvent this problem, the instrumentation installed on the bridge included signal conditioners (Figure 4.2). These devices were enclosed in a box attached to the guardrail near the gaged cables and accepted the voltage signal from the strain gages. One signal conditioner was required for each gage. A schematic of the strain measurement instrumentation is shown in Figure 4.3. Each signal conditioner changed the respective voltage signal into a current signal, which was then transmitted to the pylon containing the data acquisition system. Before the signal was read, however, it had to be converted back into a voltage signal because the data acquisition system could only monitor voltage. This conversion was accomplished by routing the current signal across a known resistance to produce a voltage proportional to the current. Finally, the voltage signal was recorded by the data acquisition system.

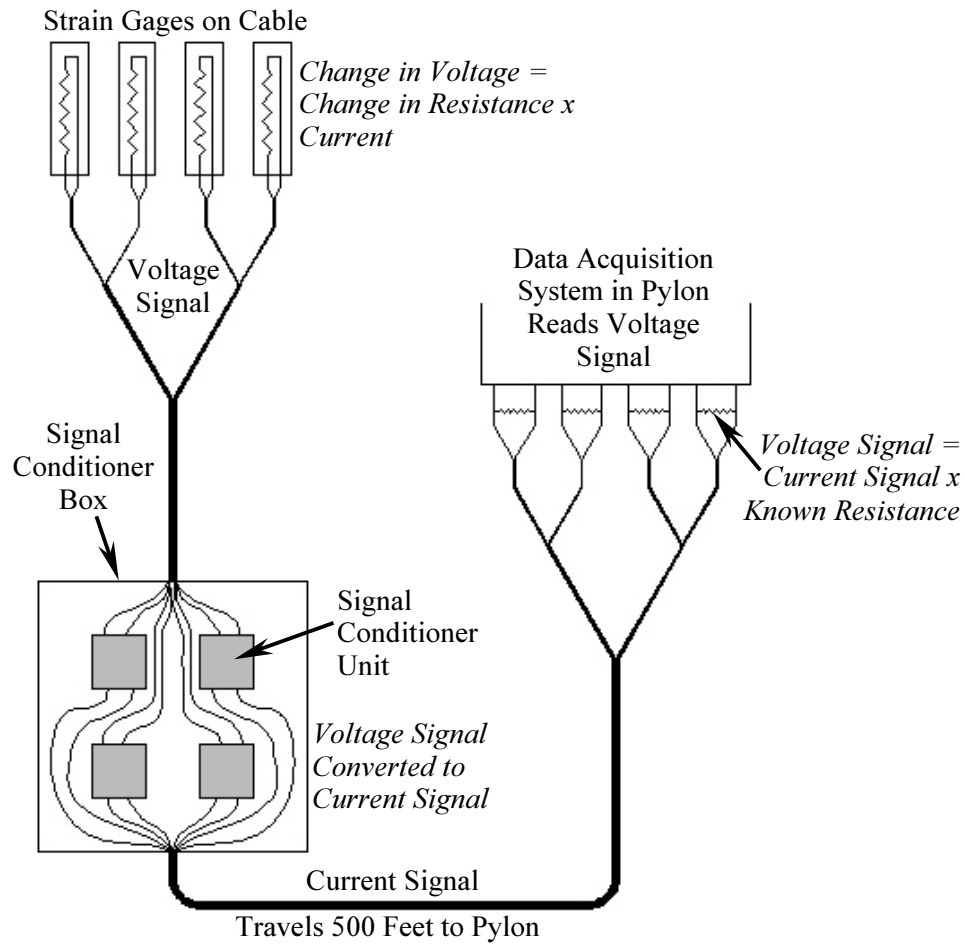


**Figure 4.3: Schematic of Instrumentation for Strain Data Collection**

***Strain Gage Description and Location***

When the instrumentation system was installed on the bridge, the signal conditioners were wired to four strain gages distributed on two adjacent, unrestrained stay cables. Two of the gages were mounted on cable A22S, one on the bottom and one on the inward-facing side. The remaining two gages monitored strain on cable A23S, one on the inward and one on the outward-facing

side of the cable. The gages were mounted approximately at the level of the guardrail (Figure 4.4).

Each strain gage was a 2.4-inch (60-millimeter), 120-Ohm concrete strain gage (Figure 4.5). The gages were installed on a thin layer of epoxy spread on the surface of the grout with M-Bond adhesive after temporary removal of a window in the polyethylene sheath. Precautions against contact of the exposed wire leads with the grout were not made because grout does not effectively conduct electricity. This was consistent with typical concrete gaging techniques.

#### ***Results of Initial Instrumentation Set-Up***

The first strain information recorded by the data acquisition system consisted of 120 records obtained over an eighteen-day period in late November



**Figure 4.4: Cable A22S Showing Window in Polyethylene Sheath Where Strain Gages Were Located**

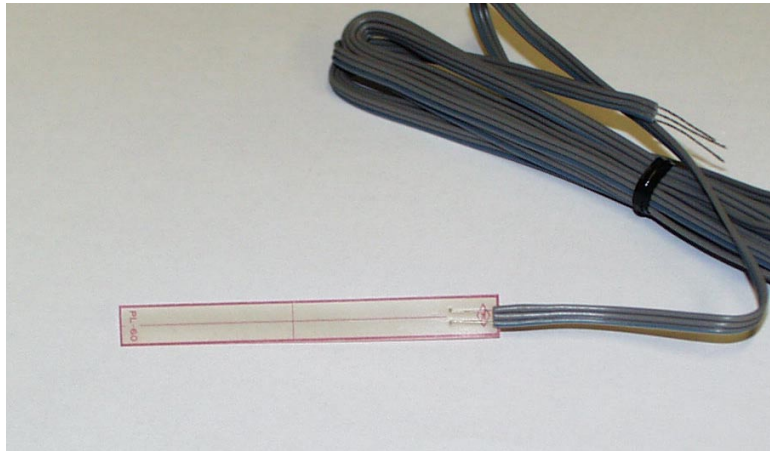


**Figure 4.5: Strain Gage**

and early December of 1999. Each five-minute data set, recorded at a sampling rate of 40 Hertz, was the result of a triggered event detected by the Johns Hopkins University monitoring system discussed in Chapter 3.

Each record was examined for meaningful strain information. No strain data were observed. Companion acceleration data provided by Johns Hopkins University indicated the presence of acceleration events. The introduction of acceleration with amplitudes several times larger than the average, however, did not produce a noticeable strain difference in any of the gages. Additionally, the recorded signal from the inward-facing strain gage on cable A22S revealed that the gage was inoperable as a result of a short circuit.

Despite the inadequacy of this first group of data records, some valuable information was gained. At least one gage required replacement. Of the three gages that provided information, all exhibited a significant amount of noise that resulted in a beating-type signal shown in a sample record (Figure 4.6). The zero of each gage's signal was shifted so that each history could be displayed

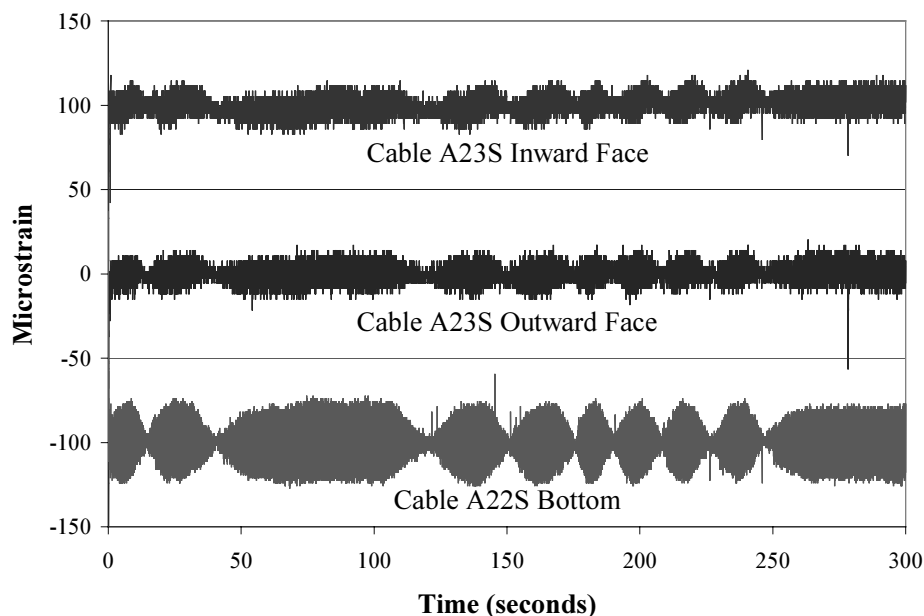


**Figure 4.6: Typical Noise Signal from Strain Data Collection**

individually. No actual strain data was found within this noise. The patterns of fluctuating signal amplitude for each gage matched one another along the time scale. Since the data shown are from two individual stay cables, this phenomenon was attributed to noise in the instrumentation system rather than to the motion of an individual cable or an isolated problem with a particular strain gage.

***Attempts to Repair the Strain Collection System***

In April of 2000, the strain gages connected to the instrumentation system were inspected. Severe corrosion was found at the location of the gage that had stopped responding (Figure 4.7). The corrosion was attributed to a process initiated by the temporary breach in the polyethylene sheath. Injected grouts very frequently contain water-retentive admixtures that trap moisture (Feld and Carper





**Figure 4.7: Corrosion Damage to Strain Gage**

1997). The brief exposure of the grout surface during application of the strain gage may have drawn some of this moisture to the surface. Since the precaution of preventing the exposed wire leads from making contact with the grout surface was not made, corrosion of the leads and the gage was inevitable. All four gages exhibited corrosive degradation.

After removing the damaged gages, four new strain gages of the same type as those that corroded were installed and linked with the instrumentation system. These new gages were mounted on the top, bottom, inward side, and outward side of cable A22S. The gaging technique was similar to the previous installation, but the exposed wire leads were prevented from making contact with the grout. The strain collection system, however, remained inoperable and was removed for repair.

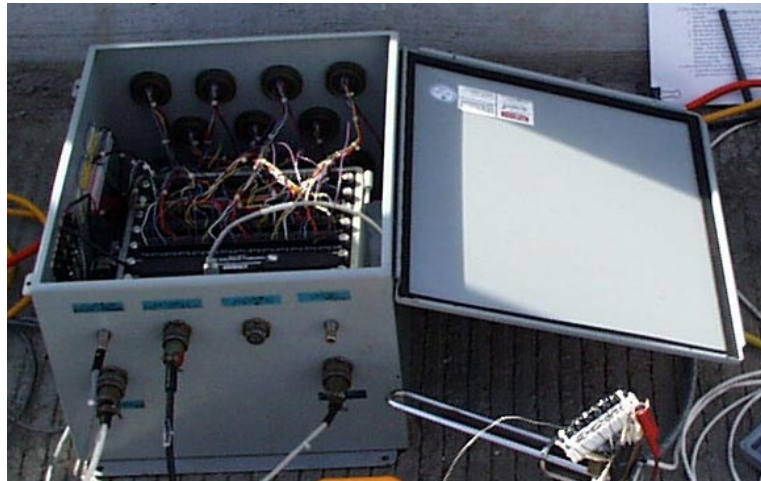


**Figure 4.8: CR9000 Mobile Data Acquisition System**

***Results of Reinstallation of Strain Collection System***

In June of 2000, the restored instrumentation system was reinstalled on the Fred Hartman Bridge, connected to the four strain gages previously applied to stay cable A22S. A mobile data acquisition system, the CR9000 (Figure 4.8), was used to collect strain information from traffic events such as the passing of large trucks. A sample record logged by the CR9000 is shown in Figure 4.9. The zero of each gage's signal was shifted so that each history could be displayed individually. The range of the typical noise in the signal was 20 microstrain, much lower than the 50-microstrain range shown in Figure 4.6. As expected, the strain history showed only axial deformation for the traffic loads experienced.

After reinstallation, several five-minute, 40-Hertz records, from triggered events, were obtained from the Johns Hopkins University monitoring system. A plot of a typical excerpt from one of these data sets allowed a relative comparison of noise levels among the individual signals (Figure 4.10). The zero of each

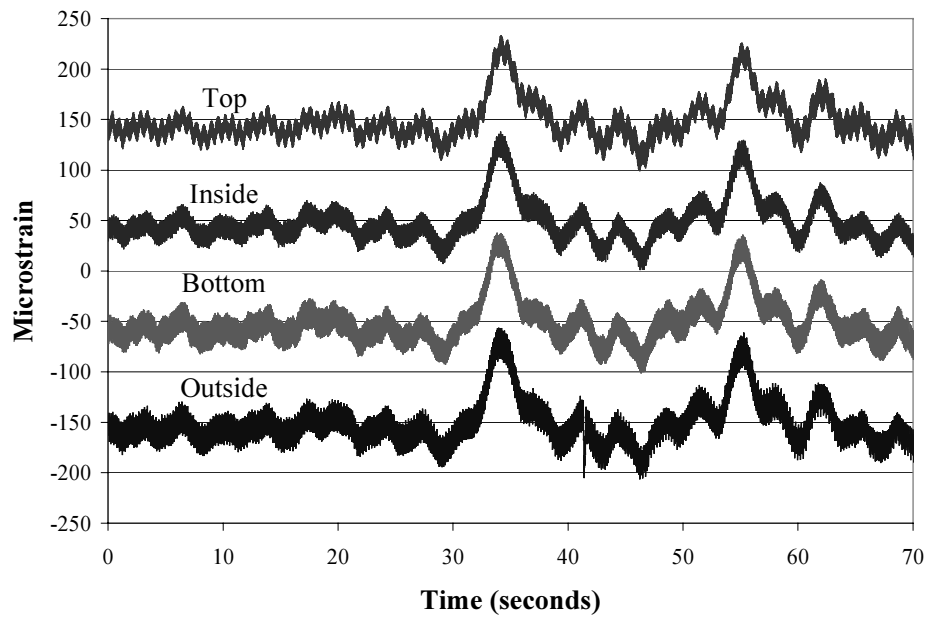


**Figure 4.9: Sample Traffic Data Collected by CR9000 on Cable A22S**

gage's signal was again shifted for visual clarity. The top and inside strain gages displayed a noise level corresponding to a 40-50 microstrain range, while the bottom and outside gages exhibited almost a 200 microstrain variance. All of these noise levels were very high, but the 200-microstrain range was considered to be unacceptable. Nevertheless, all four gages revealed an axial strain event, signifying actual strain data within the record, but the excessive noise caused noteworthy events to be difficult to identify. Therefore, the strain collection system had been improved in that strain events were being detected, but considerable noise was still presenting a significant problem.

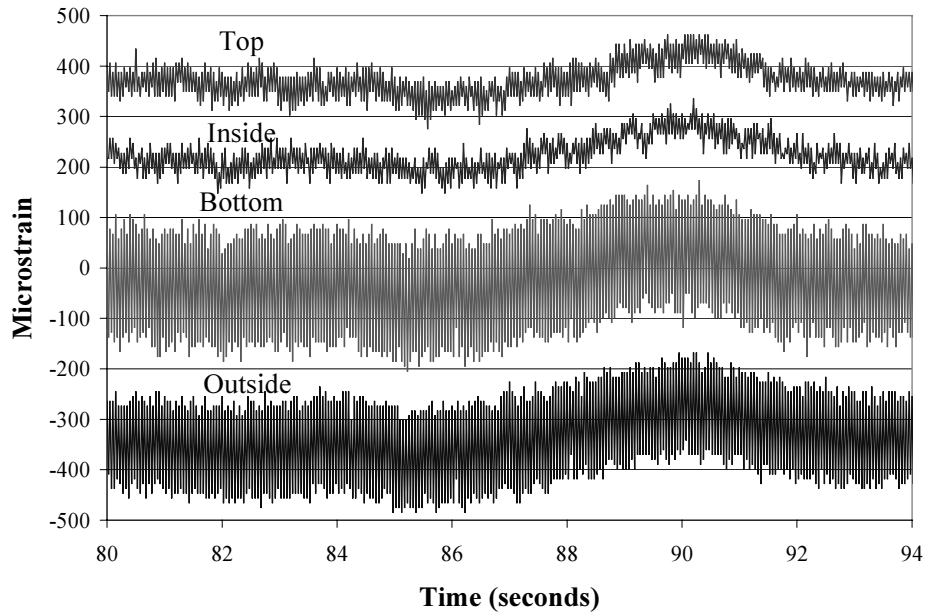


**Figure 4.10: Typical Strain Record Excerpt from Cable A22S Following Reinstallation of Instrumentation**

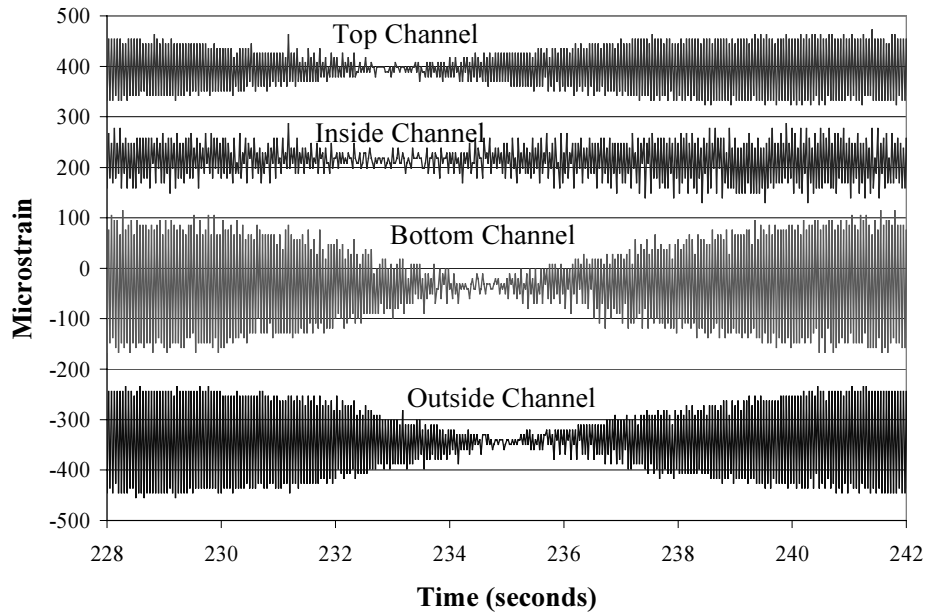


**Figure 4.11: Typical Signal Excerpt from the Channels Assigned to Cable A22S Prior to Reinstallation of Instrumentation**

### ***Further Problems and Noise Elimination Attempts***

To locate the source of the noise on the bottom and outside gages, a data set corresponding to a time before reinstallation of the strain collection instrumentation was obtained from the Johns Hopkins University monitoring system. Figure 4.11 shows the signals from the data acquisition system channels that were to be associated with the four strain gages on cable A22S. The noise that each channel exhibited was similar to the level of noise that each corresponding gage's signal displayed after reinstallation of the system. Additionally, the beating-type signal observed earlier was present, and the fluctuating signal amplitudes again matched one another along the time scale. These observations indicated that the noise problem might not be localized within the strain collection system.

In August of 2000, further attempts were made to locate the source of the seemingly external noise. Different problems, however, were discovered. Primarily, the bottom and outside gages were not responding. The outside gage was restored by replacing its signal conditioner, but a signal from the bottom gage was not recovered. Nevertheless, the system was left in place on the bridge to collect data from the three surviving gages.

Problems with Johns Hopkins University's system, including downed phone lines preventing data download, delayed the attainment of further strain records for three months. In November and December of 2000, over 1000 records, predominantly from fourteen days scattered throughout August, September, October, and November of 2000, were obtained. Johns Hopkins

University's weather and acceleration data for the corresponding time period were not dependable due to the problems with their instrumentation. According to the National Weather Service, precipitation was recorded in the area on only four of the fourteen days. The noise level of the data records was similar to the high noise level of the strain histories collected prior to the August 2000 field visit. The records showed further that in early November, one of the three remaining strain gages ceased responding.

### **Characterization of Observed Strain Events from Primary Strain Acquisition Attempts**

Deciding which strain information was the result of cable vibration without concurrently witnessing the vibration event was a challenging task, especially when significant noise existed in the measurements. Information from the analytical models to be discussed in later chapters and from the observations of Johns Hopkins University researchers, though, facilitated this endeavor, allowing recorded strain events to be identified and characterized.

### ***Expected Indicators of Cable Vibration***

As discussed in Chapter 3, with strain gages oriented on all four quadrants of a cable's circumference (as they were on cable A22S), axial strain events appear, in phase, on the data histories of each gage. With purely flexural strain from cable vibration in the plane of stays (up and down motion), for example, the top and bottom gages reflect periodic strain fluctuations in opposite directions while the inside and outside gages still only reflect the traffic data. This response

is justified by beam theory. As the cable bends into positive curvature during vibration, the top of the cable goes into compression (relative to the cable's pretensioned state) while the bottom experiences additional tension. The inside and outside gages do not reflect significant bending strain because they are positioned near the neutral axis.

Any cross-section along the length of a cable experiences a combination of bending strain and axial strain. The response described above is expected for a section in which bending dominates. The analytical models to be discussed later, however, indicate that the cable's change in length, due to the lateral displacements imposed by vibration, may produce a significant axial strain. This axial strain contribution may exceed the flexural strain level. Additionally, the axial strain component produced from vibration is theoretically constant along the length of the stay cable. Conversely, the contribution of the flexural strain to the combined strain profile depends on the location along the cable where strain is being measured.

As traffic and other loading events made axial strain prevalent among the data records obtained from the Fred Hartman Bridge's stay cables, a strain event caused by rain-wind induced vibration would be much easier to identify from flexural strain information. Therefore, a region of the cable exhibiting high curvature during lateral motion was an ideal location to obtain vibration data. Such a region of high curvature existed near the anchorage of each stay cable on the structure. The majority of this region, though, was contained within the anchorage box and the guide pipe, making application of strain gages on all sides

of the circumference of the cable impractical. Thus, the gages for the primary strain acquisition attempts were placed above the guide pipe termination (Figure 4.4), where flexural strain representation of a rain-wind induced vibration event was not guaranteed. In short, the location of the strain gages along the length of the cable could have corresponded to a cross-section dominated by axial strain, making flexural strains difficult to detect.

Despite the high level of noise experienced with the primary strain acquisition attempts, axial strain events were observed in many of the data records while flexural strain measures were not. These observations suggested at least four possible scenarios concerning the primary strain acquisition attempts. First, no data sets containing any information from a rain-wind induced vibration event were recorded. Second, a vibration event represented by flexural strain data was recorded, but could not be identified within the excessive noise. Third, a vibration event solely represented by axial strain data was recorded, but could not be identified within the excessive noise. Fourth, a vibration event solely represented by axial strain data was recorded and observed, but was mischaracterized as another phenomenon such as deck vibration. Regardless of the correct scenario, the observed axial strain events gleaned from the primary strain acquisition attempts require characterization.

### ***Traffic Events***

The most common and readily identifiable strain events observed in the data records were the result of traffic events such as the passing of large trucks. These events were recognized without the help of any filtering or smoothing



techniques, but using a floating point averaging method provided higher clarity (Figure 4.12). Strain signals from traffic events were not periodic. Rather, they consisted, generally, of a single large peak. The large peaks, typically with a magnitude of approximately 100 microstrain, were likely heavy trucks. Assuming that the strain in the grout was identical to the strain in the steel strand, the 100-microstrain range may be translated into a fatigue steel stress range of almost 3 kips per square inch (20 megaPascals). The most significant traffic event reached a strain of almost 200 microstrain (6 kips per square inch, 40 megaPascals), but smaller peaks were observed as well. For example, Figure 4.12 shows a smaller peak around 220 seconds. As demonstrated in the plot, these smaller peaks are more difficult to identify within the noise. The characterization of axial strain from traffic was validated by similar events that were witnessed while recording

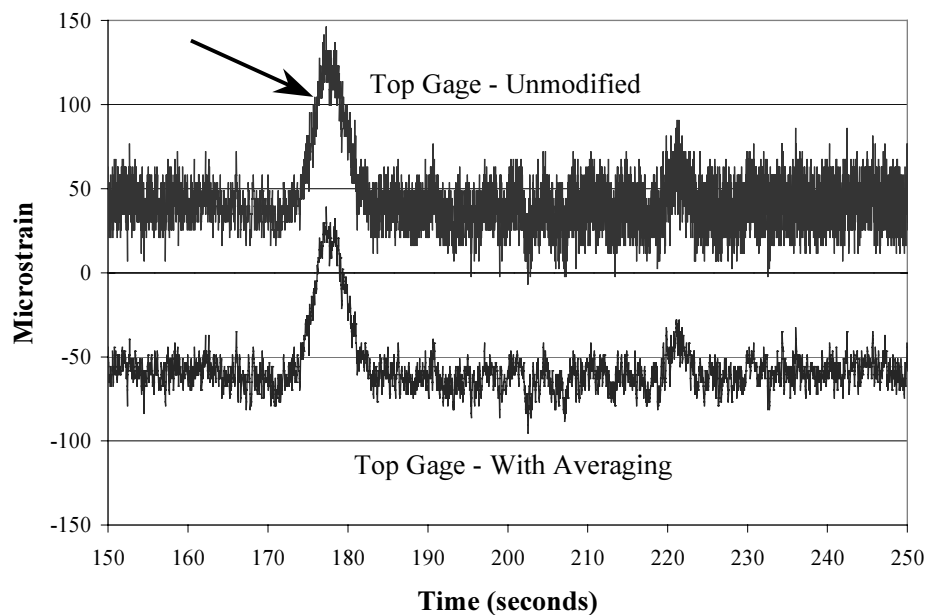


**Figure 4.12: Strain Record Excerpt from a Typical Traffic Event**

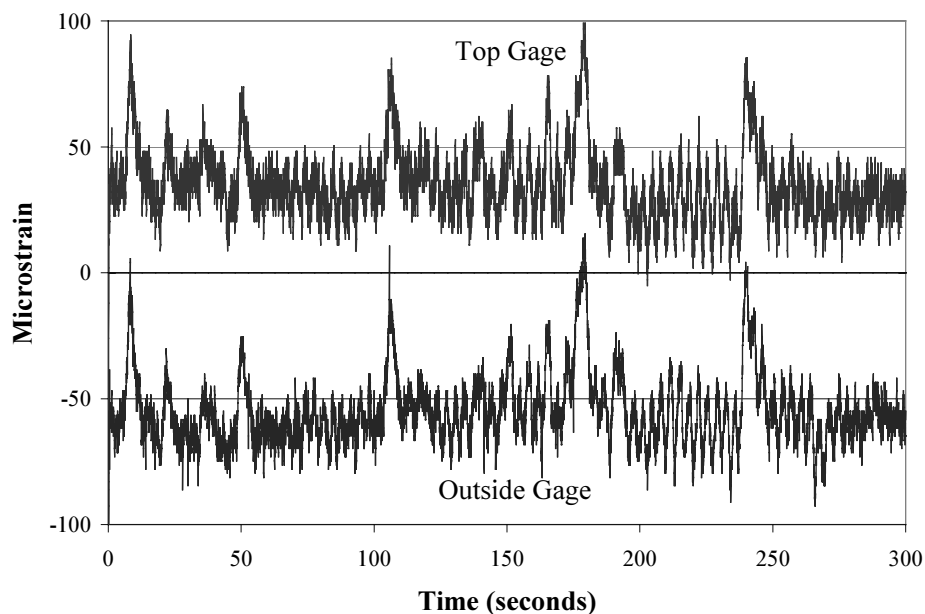
information with the mobile data acquisition system (Figure 4.9).

### ***Deck Vibration Events***

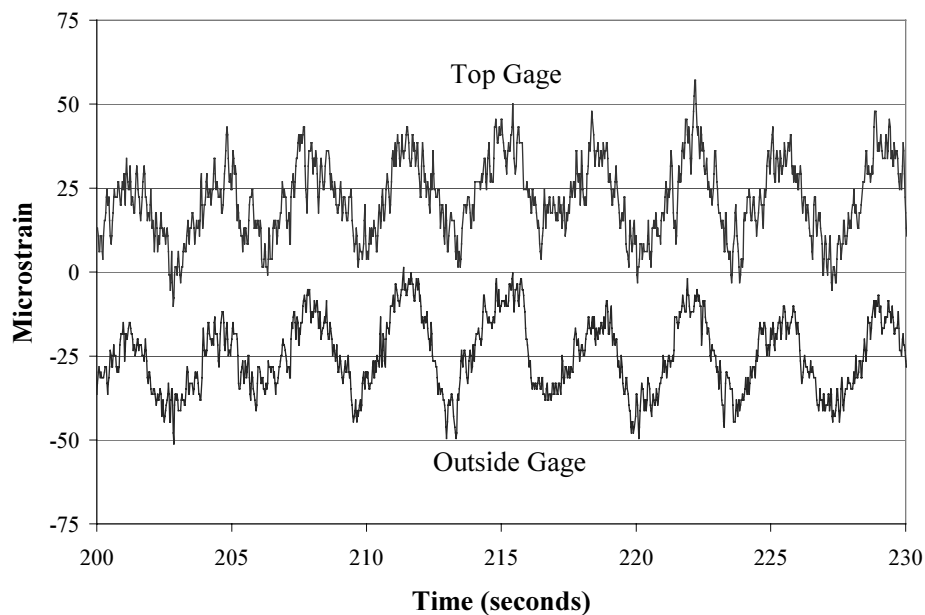
While strain from traffic events cannot likely be mistaken for cable vibration data due to the highly variable nature of traffic, other phenomena on the bridge, such as deck vibration, produced periodic axial strain in the stay cables. This periodicity was expected of purely axial representation of cable vibration. However, when investigating records including a periodic strain history such as in Figure 4.13, the time scale could be used to differentiate between cable vibration and events such as deck vibration.

Figure 4.14 shows a portion of the data record in Figure 4.13 revealing periodic strain. The plots shown are floating point averages of the original measurements, allowing a peak-to-peak amplitude of roughly 40-50 microstrain to be observed. Again assuming identical grout and steel strains, this strain range corresponds to a fatigue steel stress range of almost 1.5 kips per square inch (10 megaPascals). The two strain histories shown were in-phase, indicating that the event was axial. The time scale indicated that the period of the signal was approximately 3.5 seconds, which corresponded to a frequency of 0.29 Hertz.

Cable A22S, the element from which the strain measurements were taken, possessed a fundamental first mode frequency near 0.7 Hertz. As the frequencies for all other modes of vibration are higher than the first mode's frequency, the strain history exhibited in Figure 4.14 was likely not the result of cable vibration. Johns Hopkins University recorded and calculated that the first two modes of vibration of the Fred Hartman Bridge's deck were very close to 0.29 Hertz. Thus,



**Figure 4.13: Five Minute Strain History (with Floating Averaging) Showing Traffic Events and Deck Vibration**



**Figure 4.14: Strain Record Excerpt from a Typical Deck Vibration Event**

it was likely that deck vibration, in either the first or second mode, cyclically loading the stay cables, was responsible for the periodic strain histories observed in Figure 4.14 and in a large number of other records obtained from the primary strain acquisition attempts.

### **Secondary Strain Acquisition Attempt**

Due to the lack of effectiveness of the primary strain acquisition approach, a secondary strain collection scheme was devised so that a relationship between strain and vibration of cable A22S could be established. Instead of maintaining data collection instrumentation on the bridge to detect an actual vibration event, the mobile data acquisition unit was used to collect strain data from a manufactured vibration event produced by plucking the cable with a rope.

### ***Strain Gage Description and Location***

By March of 2001, the four strain gages on cable A22S linked to the strain collection instrumentation had corroded. The precaution of preventing the exposed wire leads from touching the grout likely increased the life of each gage but the harsh environment still caused a short gage life. After removal of the damaged gages, four new gages were installed in the same locations. To lengthen the gage life, a new variety of strain gage was used. The replacement gages were completely encapsulated in an impermeable material (Figure 4.15).

In addition to the four strain gages mounted on cable A22S at the level of the guardrail, two strain gages were installed near the tension ring of the same stay cable. Gage application was limited in this region due to the confinement of



**Figure 4.15: Encapsulated Strain Gage on Cable A22S**

the anchorage box. As a result, strain gages could only be positioned on the top and outside face at this location along the cable.

All six gages were installed using a different technique than previous attempts. A quick-setting cold weld compound formed a thin adhesive layer to attach each gage to the grout surface. This approach accelerated the gage application process and allowed data to be collected from the gages earlier.

#### ***Pluck Test Description and Results***

To establish a relationship between strain and vibration of cable A22S, an attempt was made to excite the cable manually. Whitlock Dalrymple Poston and Associates (WDP) had performed pluck tests to experimentally determine the frequencies of the lower modes of vibration of several stay cables (Kesner and Poston 1999). The test procedure involved imposing a forced vibration by pulling on a rope attached along the free length of the cable (Figure 4.16). So the forcing frequency did not affect the results, data was collected during the free vibration period directly following the excitation. Investigation of the frequency domain of



**Figure 4.16: Pluck Test of Cable A22S**

acceleration data from an accelerometer placed on the top surface of the cable revealed the lower modal frequencies.

During the March 2001 site visit, WDP performed a series of pluck tests on cable A22S. In addition to collecting acceleration data for the cable, strain data were recorded for all six strain gages using the mobile data acquisition system. The frequency domain for the acceleration data from the 40-second period following one of the tests is shown in Figure 4.17. Several natural frequencies were observed. Similarly, the frequency domain for one of the top strain gage's data for the same time period is shown in Figure 4.18. The only dominating frequency illustrated by the plot corresponded to the deck vibration phenomenon previously described. Similar plots for all of the gages revealed the same information, meaning that the amplitude of vibration produced by the pluck test was not significant enough to be detected in the strain histories.

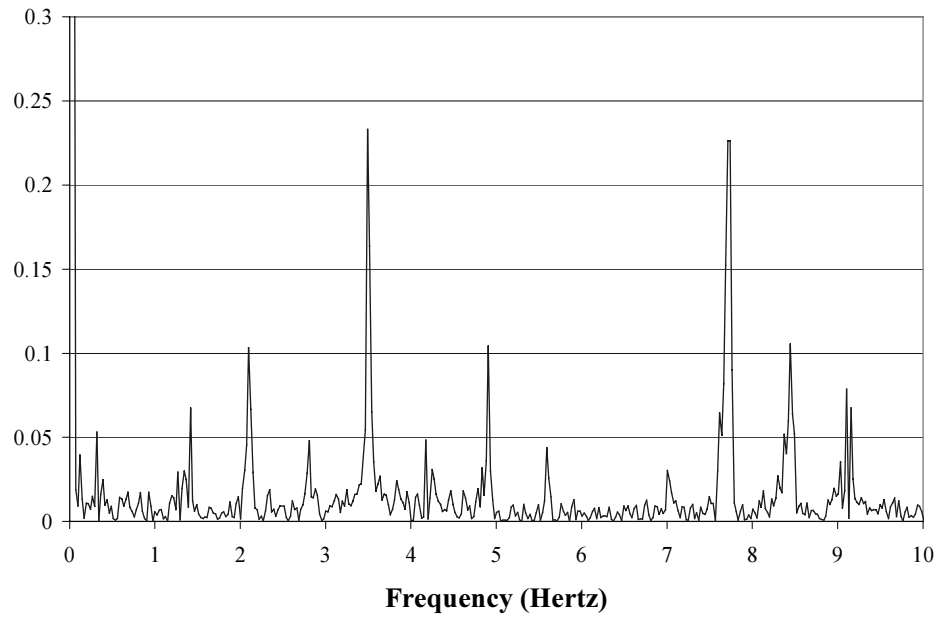


**Figure 4.17: Sample Acceleration Frequency Response**

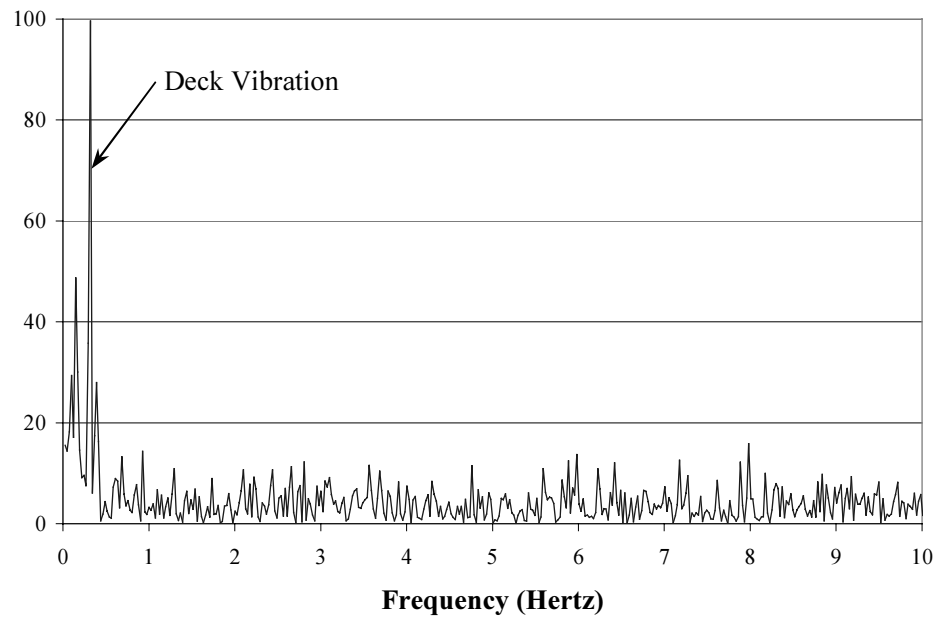


**Figure 4.18: Sample Strain Frequency Response**

The failure to detect the forced excitation with the strain gages may have indicated a general inability to record strain data from a vibration event characterized by the magnitude of accelerations present during the pluck test. The accelerations measured by WDP were approximately  $\pm 0.1g$  during the free vibration following the pluck. Main and Jones (2000) report accelerations measured during vibration events on the Fred Hartman Bridge that are many times larger. Therefore, the failure of the pluck test did not necessarily signify that a vibration event could not be detected by the strain gages.

Although all attempts to obtain strain information from both natural and manufactured vibration events failed, valuable experience was gained. Traffic and deck vibration events were characterized with typical fatigue steel stress ranges of 3 kips per square inch (20 megaPascals) and 1.5 kips per square inch (10 megaPascals), respectively, the strain gage corrosion problem was hopefully lessened with the encapsulated gages, knowledge was gained about the noise in the instrumentation system, and necessary modifications to the manual excitation method were discovered. Strain data from a stay cable vibration event on the Fred Hartman Bridge, however, must still be recorded. Such information is not only useful in assessing the severity of an oscillation event, but the data is also required to validate finite element models to be discussed in the next chapter.



## **Chapter 5: Finite Element Modeling of Fred Hartman Bridge Stay Cables**

Recalling that the ultimate goal of The University of Texas at Austin's study was the production of a set of procedures for evaluation of fatigue damage in the Fred Hartman Bridge's stay cables, the establishment of reliable analytical models that relate stay cable vibration to fatigue stress ranges was essential. The finite element program ABAQUS was implemented to create such models for two of the cables on the bridge. A preliminary model of cable A24S was established for comparison with the work of Willox (1998), and cable A22S was then modeled to allow validation by the strain measurements of cable A22S on the actual bridge structure.

### **Modeling of Cable A24S**

Willox (1998) modeled cable A24S prompting this stay cable to serve as the focus of preliminary modeling. Cable A24S is one of eight cables designated with the number 24, signifying it as the longest of the forestays (Figure 5.1). The cable is 649-feet (198-meters) long, forms a 22° angle with the bridge deck, and is prestressed to 1000 kips (4450 kiloNewtons). Cable A24S contains 50, grade 270, 0.6-inch (15-millimeter) diameter, seven-wire prestressing strands. The cable has grout diameters of 6.75 inches (171 millimeters) and 11.8 inches (300 millimeters) along the free length and anchorage region, respectively. The anchorage region is defined as the 4.5-foot (1.4-meter) length of cable from the

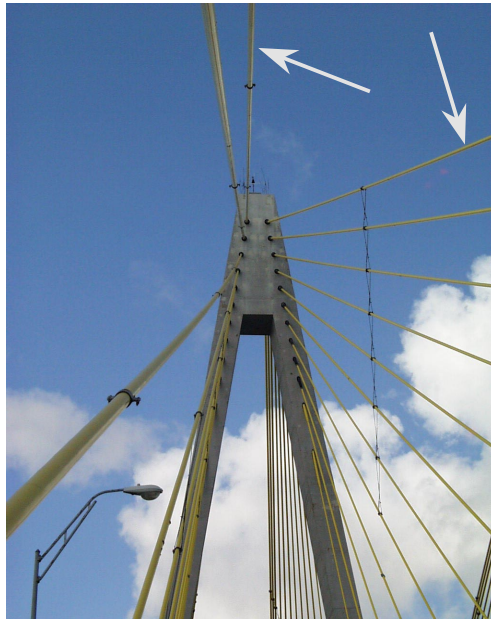


**Figure 5.1: Two of the Eight Stay Cables Designated as Cable 24**

face of the anchorage plate to the beginning of the transition region, and the transition region is the 18-inch (460-millimeter) region that gradually reduces the grout diameter from the anchorage diameter to the free length diameter. The interface of the transition region with the free length is the location of the tension ring.

#### ***Mesh Description and Model Properties***

The length of cable A24S was discretized into 1304 linear elements as shown in Figure 5.2 to form the ABAQUS mesh. Each element represents a Timoshenko beam, which allows transverse shear deformation. The small span-to-depth ratio of each individual element prompted the inclusion of transverse shear deformation, but the consequence of neglecting the effect was not investigated. The composite cross-sectional properties for each of the linear

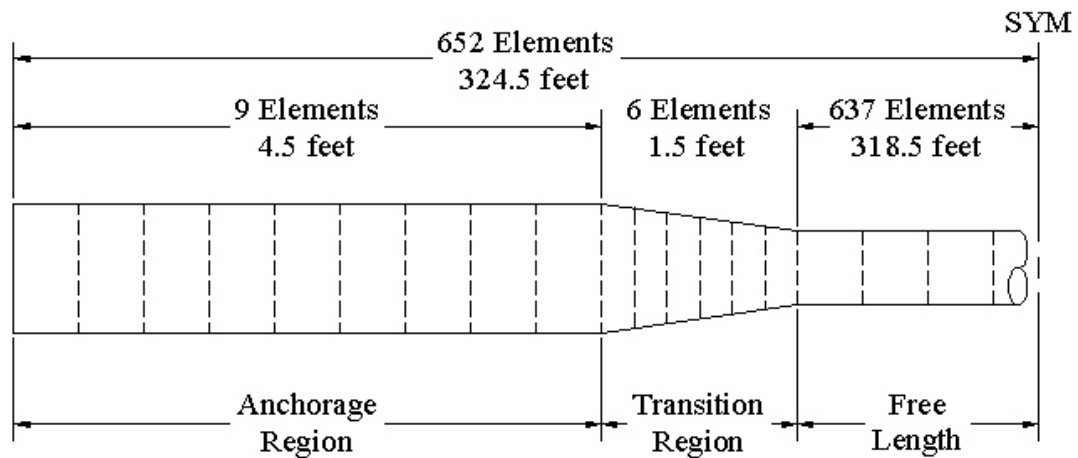


**Figure 5.2: Linear Mesh of Cable A24S for ABAQUS Finite Element Model**

elements were defined in terms of a transformed grout section. These properties were constant along the free length, but in the anchorage and transition regions, the grout diameter and tendon profile were averaged over the length of the individual element to calculate representative properties for an entire element.

Consistent with the work of Willox (1998) and Hamilton (1995), a modulus of elasticity of 27,600 kips per square inch (190 gigaPascals) was used for the steel strand, and a modulus of elasticity of 4000 kips per square inch (28 gigaPascals) was used for the grout. The grout was assumed to be uncracked, and any stiffness associated with the polyethylene sheath was neglected. Complete fixity of the cable's ends was assumed.

### ***Modeling Contact with the Anchorage Box Opening***

As discussed in Chapter 3, the most extreme vibration events were observed during a period when the high-amplitude vibrations had fractured the guide pipes leading out of the anchorage box. Thus, the cable A24S model did

not include the neoprene damper installed at the end of the guide pipe designed to dampen high frequency vibrations. The model instead provided for contact between the cable and the side of the opening to the anchorage box. A nonlinear spring was attached to the location along the cable that corresponds with the anchorage box opening (Figure 5.3). The spring possessed negligible stiffness until displacement of the model indicated that the real cable A24S would have collided with the anchorage box. At this point the spring provided a very high resistance until the displacement of the model no longer indicated contact (Figure 5.3).

### *Tensioning of the Cable Model*

During construction of the cables of the Fred Hartman Bridge (and other cable-stayed bridges), the load-carrying steel strand was tensioned before grout was injected into the polyethylene sheath. This construction technique presented a modeling difficulty because only a portion of the cross-section was prestressed.

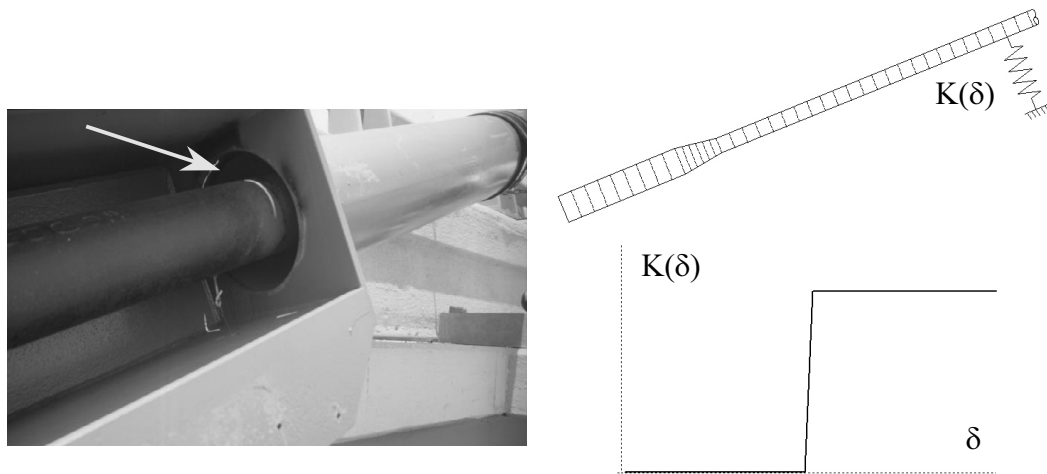


**Figure 5.3: Nonlinear Spring Representation of Anchorage Box Opening**

The models discussed here assumed that the prestressing is evenly distributed over the transformed cross-section.

The tensioning of the cable model could have been accomplished in a variety of ways from the introduction of a thermal flux to the implementation of an initial displacement. Willox (1998) employed a *construction sequence* approach. The model was created in several steps:

- 1) The untensioned length of steel strand was calculated, based on the final length of the tensioned cable and the cable's design pretension, using elastic principles.
- 2) A linear mesh was created along this untensioned length with the cable's ends modeled as pinned connections.
- 3) To tension the model, an initial displacement of one of the cable's supports was imposed as a boundary condition. The displacement created a cable model with both design length and tension.
- 4) The self-weight of the grout was then added to the model, producing a catenary deflection.
- 5) The model's supports were changed from pinned-pinned to fixed-fixed.

Willox's procedure followed the construction process of a Fred Hartman Bridge stay cable and was an effective way of modeling a pretensioned cable. The method, however, also assumed that the prestressing was evenly distributed over the transformed cross-section. Therefore, while the technique allowed more

effective visualization of model creation, it did not offer any technical advantage over methods that exploit the built-in functions of ABAQUS.

The tensioning method used in the modeling of cable A24S for the current research took advantage of the ability of ABAQUS to impose a stress on any given cross-section as an initial condition using the command *\*INITIAL CONDITIONS, TYPE=STRESS*. Using this approach, each cross-section of the model was pretensioned to a force 1.5% below the 1000 kip (4450 kiloNewton) design tension. The application of self-weight provided an axial component of force in the inclined cable that brought the model's average pretension close to the design level.

### ***Details of the Analysis***

As previously mentioned, each of the model's 1304 elements was a Timoshenko beam with each segment defined using two nodes. The resulting linear mesh was based only on the longitudinal geometry of the cable. The details of each cross-section's geometry were only represented by user-defined values for modulus of elasticity, moment of inertia, area, and density. Also included in the definition of the elements was the prescribed condition of the initial stress on each cross-section to represent the cable's pretension.

A more rigorous approach could have included a three-dimensional mesh encompassing each cross-section's geometry in addition to the longitudinal geometry. This approach could also have allowed the grout and steel to be modeled as independent materials instead of using transformed sections, allowing the pretension to be added to the steel elements only. Additionally, the transition

region could have been modeled with tapered elements instead of stepping through the change with a series of graduated uniform elements. To reduce modeling and processing time, however, the linear mesh with transformed section properties approach was chosen.

Following definition of the mesh, the analysis was divided into four steps. Step one involved fixing the ends of the cable. The actual degree of fixity at the anchorages of the Fred Hartman Bridge stay cables was unknown, but for this analysis, full fixity was assumed to provide an upper bound on the response of the cable ends. The second step statically applied the cable's self-weight. Because the cable model was inclined at the same angle as the actual cable, the self-weight imposes both lateral and axial load, creating a catenary shape. The third step extracted the modal frequencies of the tensioned cable. Step four dynamically excited the cable model to produce vibration similar to that experienced by the actual stay cable.

Due to the slenderness and high axial load of the structure being investigated, the structural analysis included geometrically nonlinear terms in the stiffness matrix. To aid in the dynamic analysis, a mass-dependent damping parameter was included that corresponded to approximately 0.5% damping in the third mode, consistent with the findings of Whitlock Dalrymple Poston and Associates (WDP) (Kesner and Poston 1999). Material nonlinearity was not considered although this issue may be a significant one. It was reasonable to assume that the high-strength steel strand would not yield, but because the cable was represented as a composite section comprised of both steel and grout, it may

not have been reasonable to assume the grout would not crack. Any deterioration of the grout would alter the stiffness of the cable, creating a material nonlinearity. This nonlinearity was neglected assuming that the contribution of the grout to the stiffness of the cable was not as significant as the contribution of the steel.

For the numerical implementation of the dynamic analysis, ABAQUS iteratively solves a set of nonlinear dynamic equilibrium equations at each time increment using Newton's method. Among the alternatives that ABAQUS provides is the option to use a fixed or variable time step for the dynamic analysis. In either case, the program calculates the equilibrium residual error (or out-of-balance forces) halfway through each time increment. This half-step residual check monitors the accuracy of the dynamic solution. If the variable time increment option is used, the half-step residual check also directs the magnitude of the next time step. A small residual indicates high accuracy and prompts a larger time increment, and a large residual signifies low accuracy and results in a smaller time increment (*ABAQUS* 1998).

For the variable time increment option, ABAQUS allows the user to specify an acceptable value for the half-step residual as a variable termed *HAFTOL*. For a highly accurate elastic solution, the *ABAQUS/Standard User's Manual* suggests a value for *HAFTOL* that is an order of magnitude lower than the expected forces and reactions in the model. On the other end of the spectrum, for a coarse elastic solution, the manual recommends a *HAFTOL* value that is one or two orders of magnitude higher than the expected model forces (*ABAQUS* 1998). For the stay cable application, the forces anticipated encompassed a large



range because the pretension of the cable was two orders of magnitude larger than the expected lateral forces. The scope of acceptable tolerance values coupled with the range of anticipated model forces left the best value for *HAFTOL* in doubt. Trial and error resulted in an optimum *HAFTOL* value of 100 kips (440 kiloNewtons) to be discussed later.

***Results of Modal Extraction***

The extraction of several fundamental modes of vibration from the cable A24S model provided the basis for both a preliminary comparison with Willox’s model and a preliminary validation from field tests performed by WDP. Based on the natural frequency of the third mode, Table 5.1 shows very close correlation between the cable A24S model and Willox’s similar model. Additionally, the natural frequency of the first mode of vibration obtained from the WDP field test matches the value from the cable A24S model very closely.

***Methods of Dynamic Excitation***

As the goal of the stay cable finite element analyses was to assess the severity of rain-wind induced vibration events through investigation of the curvatures produced during motion, a method for simulating these oscillations

<b>Table 5.1: Comparison of Measured and Calculated Natural Frequencies of Cable A24S</b>			
	First Mode	Second Mode	Third Mode
Willox Model	-	-	1.69 Hz
Dowd Model	0.585 Hz	1.15 Hz	1.72 Hz
WDP Field Test	0.585 Hz	-	-

was necessary. As discussed in Chapter 3, cable 24, vibrating in the third mode, provided the largest observed peak-to-peak displacement amplitude, estimated at 42 inches (1070 millimeters) (Weaver and Poston 1998). This event was established as the *worst-case scenario* to be investigated (Figure 5.4). For cable A24S, the third-mode frequency and mode shape were obtained from the modal extraction. The interference of the anchorage box opening (modeled with the nonlinear spring) prevented a simple mode shape magnification procedure from providing the desired curvatures. Numerous options for exciting the cable were available, but significant difficulty was encountered while attempting to produce the desired motion.

A general approach to the cable excitation problem involved disturbing the catenary shape in some way to produce free vibrations. This excitation could be accomplished by numerous means including lateral pulses at one or more positions along the length of the cable, release of an initial displaced shape, or even transversely cycling the position of one end support to produce a whipping effect. These methods, however, were difficult to calibrate. While free vibration

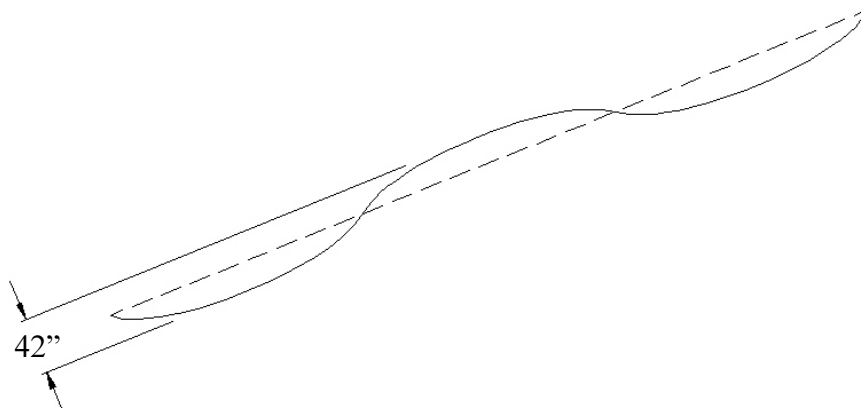


**Figure 5.4: *Worst-Case Scenario* Vibration Event for Cable A24S Model**

could have been attained, achieving specifically the *worst-case scenario* of third mode vibration with a peak-to-peak displacement amplitude of 42 inches (1070 millimeters) would be considerably more challenging. As a result, a forced vibration approach was used.

A preliminary forced vibration attempt included a single, cyclic point load applied, transverse to the stay cable's longitudinal axis, at midspan (Figure 5.5a). The frequency of the load matched that of the cable's third mode. This approach produced wave propagations, originating at the point load and traveling along the length of the cable toward the two anchorages. The desired third mode shape was not produced, and numerical difficulties were encountered, prompting the method to be improved. Similar cyclic point loads were added to the cable's quarter points (Figure 5.5b). The third mode frequency was again used, and similar numerical difficulties were again experienced.

The wave propagation problems and numerical difficulties indicated that the forced vibration of the cable required additional control. Therefore, the excitation technique evolved into an approach where every fifth node along the length of the model was cyclically loaded (Figure 5.5c). The magnitude of each point load was scaled relative to the model's third eigenvector as in Equation 5.1.

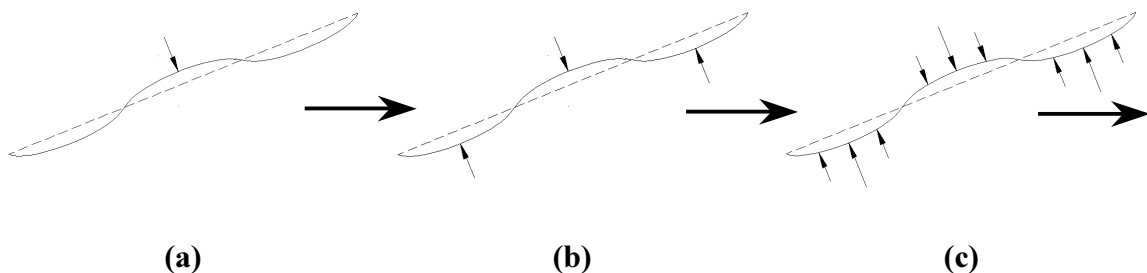


**Figure 5.5: Excitation Using Cyclic Transverse Point Loads**

$$F(t, x) = SM_3(x) \sin(\omega t) \quad \text{Equation 5.1}$$

Where  $F(t, x)$  represents the point load at a location  $x$  along the length of the cable at time  $t$ . The transverse component of displacement at location  $x$  corresponding to the cable's third mode shape is denoted by  $M_3(x)$ , and  $S$  designates an overall scale factor that was adjusted to achieve the desired displacement amplitude of cable vibration. Each load was again cycled at the same frequency,  $\omega$ , as the cable's third mode.

The excitation method produced unrealistically large curvatures under the point loads, making the region where dynamic loading occurred a poor model of the actual cable behavior. Because this study was focused, however, on the cable anchorages, approximately 25 feet (7.6 meters) of the model's length at each end were exempted from the cyclic point loads. This balance left a sufficient length of the cable exposed to dynamic loading to sustain the *worst-case scenario* while leaving an adequate portion of the cable ends unrestrained to respond freely to the vibration.

Numerical problems were still encountered with this method of excitation, prompting a variable time increment to be used for the dynamic analysis. As mentioned earlier, the scope of acceptable values for the half-step residual tolerance, *HAFTOL*, coupled with the range of anticipated model forces left the best value for the tolerance parameter in doubt. The minimum value for *HAFTOL* that would allow the analysis to proceed was 100 kips (440 kiloNewtons). This value was an order of magnitude greater than the maximum applied transverse force but was an order of magnitude less than the pretension of 1000 kips (4400

kiloNewtons). The *ABAQUS/Standard User's Manual* implies such a value for *HAFTOL* provides moderate accuracy. Significant improvements to the method of dynamic excitation were made for the cable A22S model that will be discussed later.

### ***Results of the Dynamic Analysis***

A consequence of the linear mesh modeling technique was that a stress profile for a given cross-section could not be directly produced by ABAQUS. The program could not make calculations based on cross-sectional geometry that it was never given. Equation 5.2 allowed all of the stress profiles to be calculated based upon the curvature,  $\phi$ , provided by the analysis.

$$\sigma(y) = \phi y E(y) \quad \text{Equation 5.2}$$

The stress a distance  $y$  from the centroid is represented by  $\sigma(y)$ , and  $E(y)$  denotes the modulus of elasticity at location  $y$ . Equation 5.2 assumes elastic behavior and that no slip occurs between the strand and uncracked grout.

In this manner, stress profiles for the extreme grout fiber stress and extreme steel fiber stress were calculated along the 25 feet (7.6 meters) of the model's length nearest the anchorage. Figure 5.6 shows the extreme grout fiber stress profile for the cable's peak response during the *worst-case scenario* vibration event. The maximum stress of 9.4 kips per square inch (65 megaPascals) occurred at the anchorage plate. Another peak occurred at the tension ring with a stress of 7.0 kips per square inch (48 megaPascals). The location of the anchorage box opening was accompanied by a third local maximum of 2.2 kips per square inch (15 megaPascals). Similarly, Figure 5.7

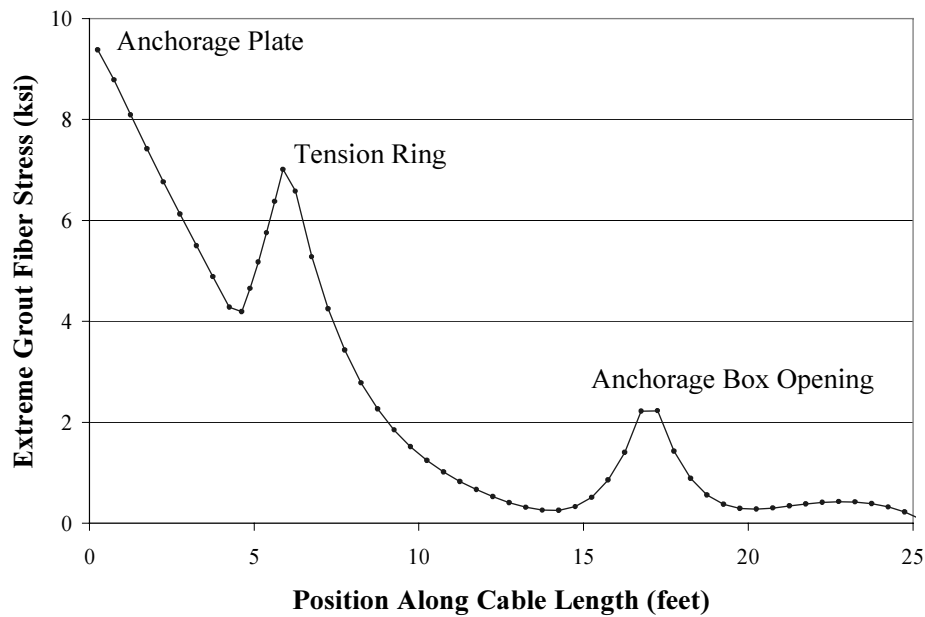


**Figure 5.6: Extreme Grout Fiber Stress Profile for 25 feet of Cable A24S Model Nearest the Deck Anchorage**

illustrates the extreme steel fiber stress profile for the same peak cable motion. The same locations for the peaks of stress were observed: 49 kips per square inch (340 megaPascals) at the anchorage plate, 33 kips per square inch (230 megaPascals) at the tension ring, and 11 kips per square inch (76 megaPascals) at the anchorage box opening.

The stress magnitudes produced from the *worst-case scenario* dynamic excitation of the cable A24S model were very large compared to expected values, but they were less than the values obtained by Willox (1998) (Table 5.2). The grout stress throughout the anchorage region was significantly higher than the grout’s modulus of rupture, implying substantial cracking of the grout. The deterioration of the grout indicated by the model, however, was not observed on

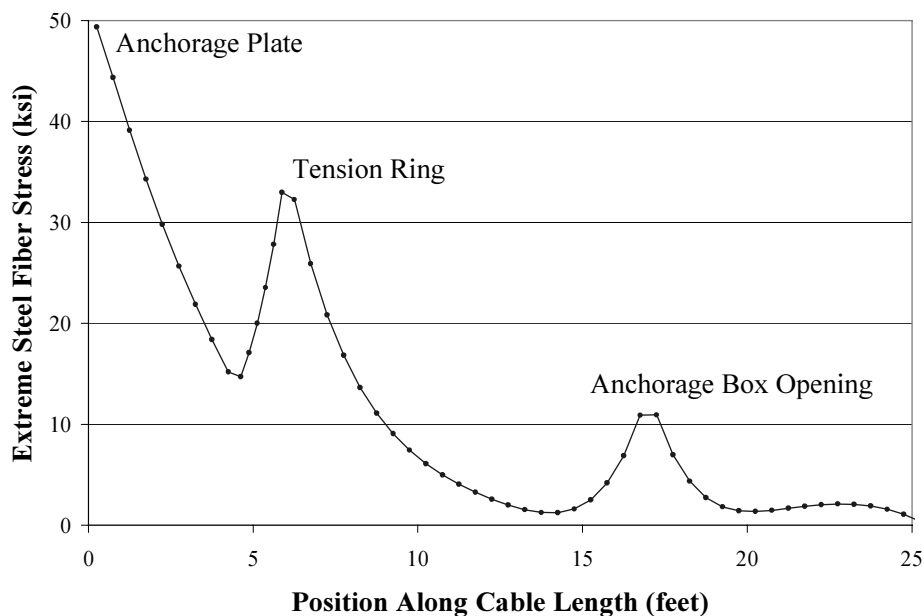


**Figure 5.7: Extreme Steel Fiber Stress Profile for 25 feet of Cable A24S Model  
Nearest the Deck Anchorage**

the actual bridge. Additionally, the force in the spring representing contact with the anchorage box opening should correspond to the lateral force transmitted by the cable during contact on the actual structure. For the peak motion presented, the spring force exceeded 20 kips (89 kiloNewtons). As described in Chapter 3, an inspection of cable A24S revealed an indentation in the polyethylene sheath at the location of the anchorage box opening. Contact definitely had occurred, but the condition of the sheath did not suggest that a collision transferring 20 kips (89 kiloNewtons) had ever taken place.

The cable A24S finite element model, therefore, might be regarded as an upper bound on the actual stay cable response. Excitation with a series of cyclic point loads was not the most controlled method of dynamic loading, and the

<b>Table 5.2: Comparison of Cable A24S Finite Element Models at Peak of Cable Motion</b>			
Location	Material	Dowd Model	Wilcox Model
Anchorage	Grout	9.4 ksi	13.3 ksi
	Steel	49 ksi	91.8 ksi
Tension	Grout	7.0 ksi	11.1 ksi
	Steel	33 ksi	76.5 ksi

*worst-case scenario* event, based on an estimated displacement amplitude, was perhaps too severe. While creating the cable A22S model, considerable improvements were achieved in the areas of dynamic excitation method and the definition of the simulated extreme event.

### **Modeling of Cable A22S**

Validation of a finite element model may be accomplished through comparison of model data to information obtained from the actual structure being analyzed. Since the focus of the strain data collection efforts detailed in Chapter 4 was cable A22S, this stay cable was modeled in ABAQUS. Cable A22S is one of eight cables designated with the number 22, signifying it as the third longest of the fore stays. The cable is 553-feet (168-meters) long, forms a 25° angle with the bridge deck, and is prestressed to 806 kips (3590 kN). Cable A22S contains 44, grade 270, 0.6-inch (15-millimeter) diameter, seven-wire prestressing strands. The cable has grout diameters of 5.9 inches (150 millimeters) and 10.2 inches (260 millimeters) along the free length and anchorage region, respectively. The



anchorage region is defined as the 5-foot (1.5-meter) length of cable from the face of the anchorage plate to the beginning of the transition region, and the transition region is again the 18-inch (460-millimeter) region that gradually reduces the grout diameter from the anchorage diameter to the free length diameter. The interface of the transition region with the free length remains the location of the tension ring.

***Mesh Description, Model Properties, and Analysis Details***

The length of cable A22S was discretized into 1111 linear elements as shown in Figure 5.8 to form the ABAQUS mesh. Similar to the cable A24S model, each element represents a Timoshenko beam with composite cross-sectional properties defined in terms of a transformed grout section. These properties were constant along the free length, but in the anchorage and transition regions, a grout diameter and tendon profile location that were averaged over the length of the individual element were used to calculate representative properties for an entire element.

Consistent with the cable A24S model, the work of Willox (1998), and the

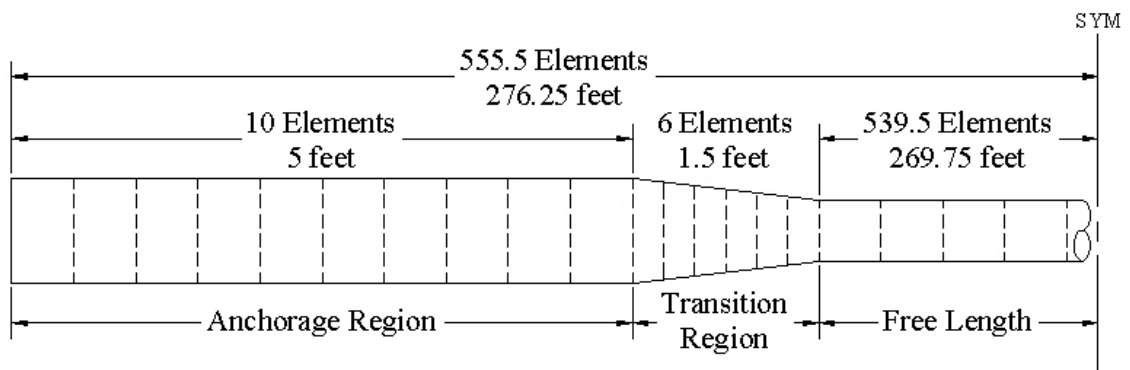


**Figure 5.8: Linear Mesh of Cable A22S for ABAQUS Finite Element Model**

work of Hamilton (1995), a modulus of elasticity of 27,600 kips per square inch (190 gigaPascals) was used for the steel strand, and a modulus of elasticity of 4000 kips per square inch (28 gigaPascals) was used for the grout. Despite the results of the cable A24S model, the grout was still assumed to be uncracked, and any stiffness associated with the polyethylene sheath was neglected. Complete fixity of the cable's ends was again assumed.

Similar to the cable A24S model, contact with the anchorage box opening was modeled with a nonlinear spring as described earlier, the cable model was tensioned using the same prescribed condition approach, and the same mass-dependent damping parameter was used to aid in the dynamic analyses. The overall analysis was again divided into four steps. Step one involved fixing the ends of the cable. The second step statically applied the cable's self-weight. The third step extracted the modal frequencies of the tensioned cable, and step four dynamically excited the cable model to produce vibration similar to that experienced by the actual stay cable. The structural analysis again included geometrically nonlinear terms in the stiffness matrix, but neglected any material nonlinearity.

### ***Results of Modal Extraction***

The extraction of several fundamental modes of vibration from the cable A22S model provided the basis for a preliminary comparison with the field tests performed by WDP (Table 5.3). The natural frequency of the first mode of vibration obtained from the WDP field test matches the value from the cable A22S model closely.

<b>Table 5.3: Comparison of Measured and Calculated Natural Frequencies of Cable A22S</b>			
	First Mode	Second Mode	Third Mode
Dowd Model	0.686 Hz	1.35 Hz	2.03 Hz
WDP Field Test	0.700 Hz	-	-

### ***Method of Dynamic Excitation***

As discussed in Chapter 3, cable 24, vibrating in the third mode, provided the largest observed peak-to-peak displacement amplitude, estimated at 42 inches (1070 millimeters) (Weaver and Poston 1998). This event was investigated using the cable A24S model and was found to be possibly too severe. Instead of establishing the model's extreme vibration event based on an estimated displacement amplitude, the motion event simulated for cable A22S was founded on physical evidence from the Fred Hartman Bridge. The inspection of the polyethylene sheath at the anchorage box opening of cable A22S revealed a very minor indentation (Figure 5.9). The damage was similar but less severe than that of cable A24S. The condition of the sheath indicated that while contact of the cable with the anchorage box did occur, the collision was minor. The extreme vibration event for the cable A22S model was, therefore, established as the cable motion producing light contact with the anchorage box opening. Light contact was defined for the model as producing a force of approximately 2.5 kips (11 kiloNewtons) in the nonlinear spring.

The method of dynamic excitation used for the cable A22S model was similar to that of the cable A24S model in that many nodes along the free length



**Figure 5.9: Example of Indentation in Polyethylene Sheath at Anchorage Box Opening**

were controlled to capture the free response of the anchorage zone, but improvements were made. Instead of using cyclic point loads to displace the cable, the nodes were forced to move using displacement control. The motion of each node transverse to the cable's longitudinal axis was defined with Equation 5.3.

$$U_{T,DYN}(t,x) = SM_3(x)\sin(\omega t) + U_{T,SW}(x) \quad \text{Equation 5.3}$$

Where  $U_{T,DYN}(t,x)$  represents the imposed transverse displacement at a location  $x$  along the length of the cable at time  $t$ . The transverse component of displacement at location  $x$  corresponding to the cable's third mode shape is denoted by  $M_3(x)$ , and  $U_{T,SW}(x)$  represents the transverse displacement due to the static self-weight catenary at location  $x$  to ensure that oscillation occurred about the catenary shape rather than the straight configuration. Finally,  $S$  designates an overall scale factor that was adjusted to achieve the desired displacement amplitude of cable

vibration. Each imposed displacement was again cycled at the same frequency,  $\omega$ , as the cable's third mode.

Similar to the cable A24S model, the excitation method produced unrealistically large curvatures in the region of controlled displacement, making this portion of the cable a poor model of the actual structural response. Because this study was focused on the cable anchorages, approximately 22 feet (6.7 meters) of the model's length at each end were exempted from the displacement control. This balance left a sufficient length of the cable exposed to dynamic loading to sustain the simulated vibration event while leaving an adequate portion of the cable ends unrestrained to respond freely to the vibration.

Numerical problems were initially encountered with this method of excitation. The root of the numerical instability was located in the definition of the nonlinear spring representing the anchorage box opening. Recall that contact was simulated with a large spring stiffness once a specified displacement was achieved. This rigid spring stiffness was defined at a level many orders of magnitude higher than the next largest term in the model's stiffness matrix, preventing efficient manipulation of the matrix solution. The spring stiffness was reduced to a magnitude closer to the other stiffness terms. This change eliminated many numerical problems while effectively maintaining the desired behavior of the anchorage box opening. The cable A24S model was altered as well to determine if the change in stiffness significantly affected the force in the spring at the peak cable motion. The force still exceeded 20 kips (89 kiloNewtons),

indicating that the *worst-case scenario* was unrealistically severe even with the change in spring stiffness.

### ***Results of the Dynamic Analysis***

The simulated vibration event used in the dynamic analysis of cable A22S was defined as the cable motion required to make the light contact with the anchorage box opening as defined earlier. After calibrating the model using the overall scale factor,  $S$ , in Equation 5.3, the peak-to-peak displacement amplitude for the simulated event was approximately 36 inches (910 mm). This amplitude compares reasonably well to the displacement amplitudes estimated on the Fred Hartman Bridge.

The cable A22S model incorporated the same linear mesh modeling technique as the cableA24S model, again necessitating the use of Equation 5.2 to determine stress profiles. In this manner, stress profiles for the extreme grout fiber stress and extreme steel fiber stress were calculated along the 20 feet (6.1 meters) of the model's length nearest the anchorage. Figure 5.10 shows the extreme grout fiber stress profile for the cable's peak motion during the simulated vibration event. The maximum stress of 12 kips per square inch (83 megaPascals) occurred at the anchorage plate. Similar to the A24S model, another peak occurred at the tension ring with a stress of 6.3 kips per square inch (43 megaPascals). The location of the anchorage box opening was accompanied by a very slight third local maximum of 0.37 kips per square inch (2.6 megaPascals). Figure 5.11 illustrates the extreme steel fiber stress profile for the same peak in cable motion. The same locations for the peaks of stress were observed: 65 kips

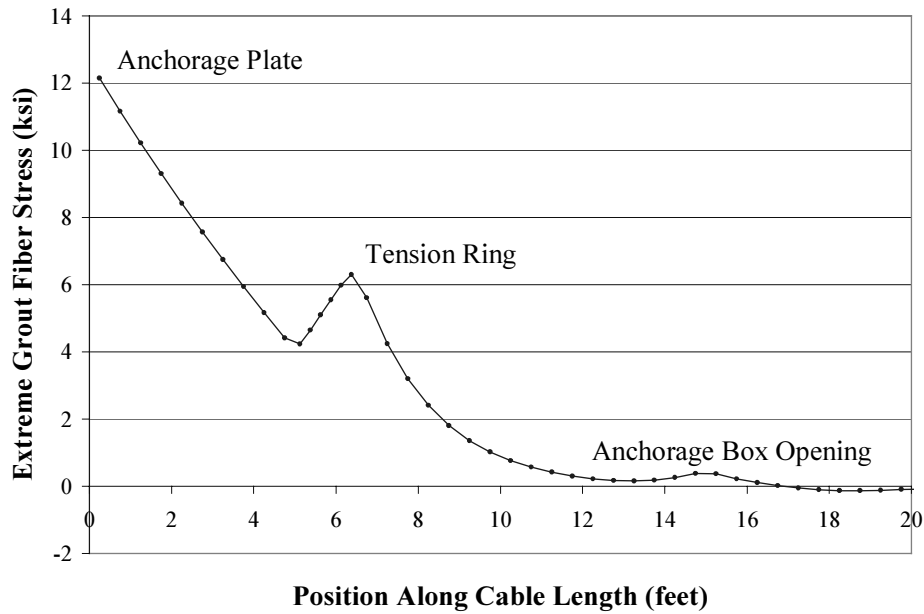


**Figure 5.10: Extreme Grout Fiber Stress Profile for 20 feet of Cable A22S**

**Model Nearest the Deck Anchorage**

per square inch (450 megaPascals) at the anchorage plate, 30 kips per square inch (210 megaPascals) at the tension ring, and 1.9 kips per square inch (13 megaPascals) at the anchorage box opening.

The stress magnitudes produced from the dynamic excitation of the cable A22S model were very large compared to expected values. As with cable A24S, the grout stress throughout the anchorage region was significantly higher than the grout’s modulus of rupture, implying substantial cracking of the grout. The deterioration of the grout indicated by the model, however, again was not observed on the actual structure. A possible reason for this phenomenon will be discussed in a Chapter 8.

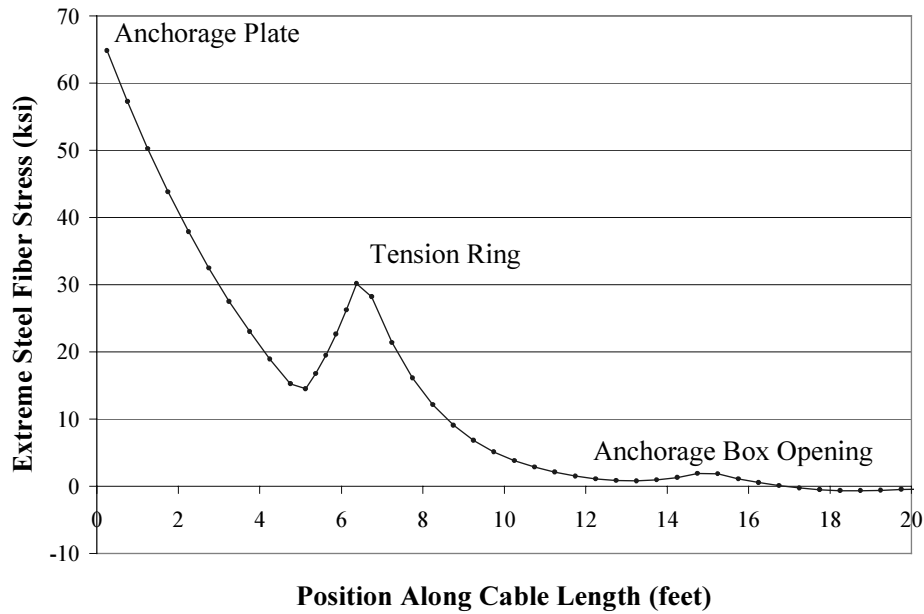


**Figure 5.11: Extreme Steel Fiber Stress Profile for 20 feet of Cable A22S Model Nearest the Deck Anchorage**

Table 5.4 displays a comparison between the cable A22S results and the corresponding peak values of the cable A24S model. The simulated vibration event for the A24S model was constrained by the maximum observed amplitude, resulting in severe contact with the anchorage box opening. The motion of A22S was established based on physical evidence, resulting in the light contact with the anchorage box opening indicated by the indentation in the polyethylene sheath.

Table 5.4 shows that the cable A24S model accrued higher stress at the tension ring and anchorage box opening at the peak motion while the A22S model accumulated higher stress at the anchorage plate. The trend at the anchorage box opening could be reasonably explained by the relative severity of contact. A more significant contact event (as with A24S) produced a larger stress concentration.



<b>Table 5.4: Comparison of Cable A22S and Cable A24S Finite Element Models at Peak of Cable Motion</b>			
Location	Material	Cable A22S Model	Cable A24S Model
Anchorage Plate	Grout	12 ksi	9.4 ksi
	Steel	65 ksi	49 ksi
Tension Ring	Grout	6.3 ksi	7.0 ksi
	Steel	30 ksi	33 ksi
Anchorage Box Opening		Light Contact	Severe Contact
	Grout	0.37 ksi	2.2 ksi
	Steel	1.9 ksi	11 ksi

This explanation seemed to apply to the comparison of tension ring stresses as well, but the anchorage plate stresses display the opposite trend. Cable A22S may exhibit a higher anchorage plate stress because of the less severe contact at the opening. The contact adds an inflection point and changes the curvature profile along the length of the cable, reducing the motion of the cable at the face of the anchorage plate. With the minimal contact, more energy is transferred to the anchorage plate, resulting in more motion, more critical curvature, and, thus, higher stress.

### **Axial Strain Representation of Lateral Vibration**

The cable A22S model was used to investigate the significance of axial strain resulting from a vibration event. As discussed in Chapter 4, the strain gages

placed on cable A22S of the Fred Hartman Bridge had to be positioned in a location along the cable's length that may not experience considerable flexural strain. The element in the cable A22S model's mesh corresponding to the strain gage location was monitored for axial and extreme grout fiber flexural strain for a variety of vibration displacement amplitudes. Figure 5.12 exhibits the two strain components for the initial six seconds of a simulated vibration event with a mean-to-peak displacement amplitude of 4 inches (100 millimeters). For reference, the mean-to-peak displacement amplitude for the event in which the cable made light contact with the anchorage box opening was approximately 18 inches (460 millimeters). The 4-inch (100-millimeter) amplitude event was considered to be more prevalent on the bridge.

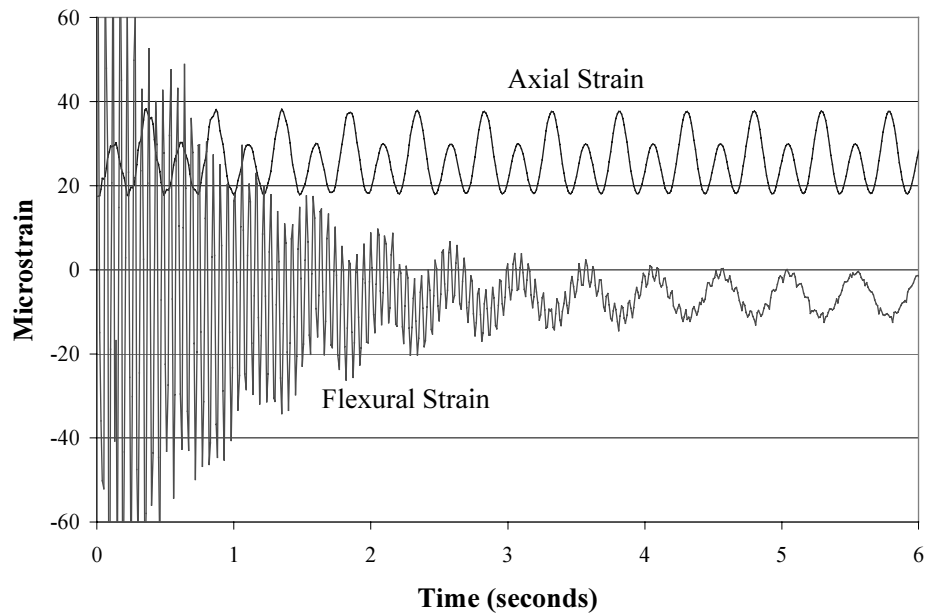


**Figure 5.12: Comparison of Axial and Flexural Strain at the Strain Gage Location on Cable A22S**

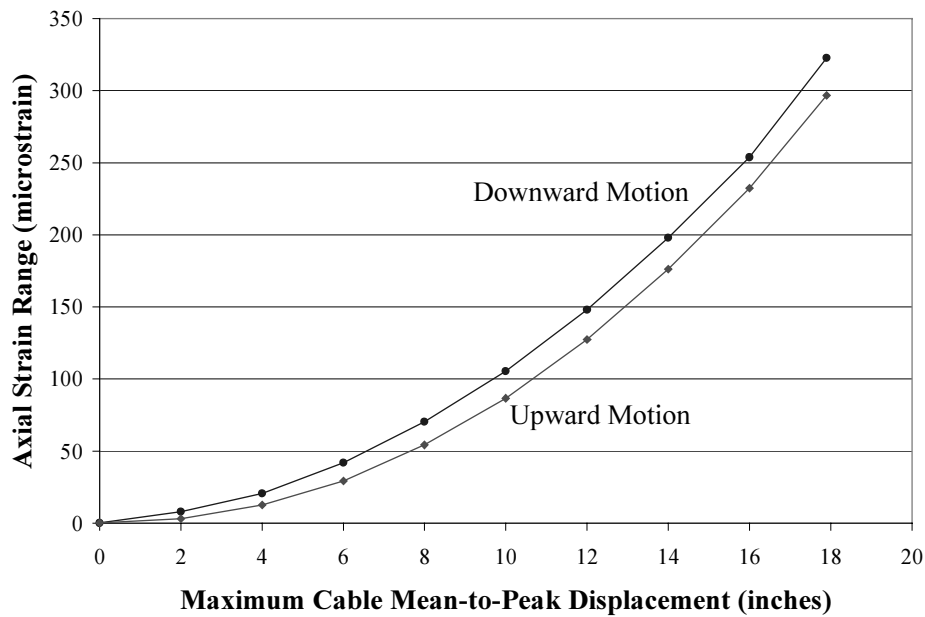
Figure 5.12 indicates that, in the model, the large flexural strains observed at the beginning of the motion were an artifact of the excitation method. Over a short period of time, the flexural strain reduced to a sinusoidal response matching the frequency of the cable oscillation. After damping out of the high frequency response to the excitation, the flexural strain range associated with a mean-to-peak displacement amplitude of 4 inches (100 millimeters) was approximately 10 microstrain.

Figure 5.12 also reveals significant information about the axial strain response. The minimum axial strain of 18 microstrain corresponded to the axial strain due to the self-weight catenary. The plot also shows that the amplitude of the sinusoidal axial strain was not constant. Rather, two individual amplitudes alternate throughout the response. The frequency of the axial sinusoid was twice that of the flexural strain curve because maximum axial strain is positive for both the upward and downward peaks of motion with the minimum value corresponding to the cable passing through the self-weight catenary. Flexural strain at a particular location has maximum and minimum values that correspond to the upward and downward peaks of cable motion, respectively. Therefore, the alternating amplitudes of the axial strain response were the result of alternating upward and downward peaks of cable motion. The axial strain range associated with a mean-to-peak displacement amplitude of 4 inches (100 millimeters) was approximately 21 and 13 microstrain for the downward and upward peaks, respectively.

The axial strain range, then, from the self-weight catenary position to the downward peak of cable motion, was 21 microstrain, while the flexural strain range, for the same simulated vibration event, from the upward peak to the downward peak of cable motion, was only 10 microstrain. Therefore, for the position along cable A22S where the strain gages were located, the finite element model indicated that axial strain was more significant than flexural strain. So that any periodic axial strain recorded by the strain collection instrumentation could be roughly calibrated into a vibration event of known severity, the axial strain response was established for a spectrum of mean-to-peak displacement amplitudes ranging from zero to the 18-inch (460-millimeter) amplitude that caused the cable to lightly contact the anchorage box opening (Figure 5.13). The largest axial strain range of over 300 microstrain was very significant when the strain data from the Fred Hartman Bridge were reviewed. The largest event recorded was a rare traffic load producing an axial strain range of approximately 200 microstrain. Typical traffic events were below 100 microstrain. Therefore, based on the analysis, a significant rain-wind induced vibration event would be very evident from the periodic axial strain response alone.

### **Validation of Finite Element Models**

The cable A22S model was created, in part, to allow validation of the ABAQUS modeling technique through comparison of results with strain data collected from cable A22S on the Fred Hartman Bridge. As detailed in Chapter 4, reliable strain data from a known vibration event was never acquired despite



**Figure 5.13: Axial Strain Ranges at the Cable A22S Gage Location Corresponding to Maximum Mean-to-Peak Displacement Amplitudes**

repeated efforts, preventing such a validation. Chapter 6, however, discusses finite element modeling of a full-scale stay cable specimen for laboratory fatigue testing, and Chapter 7 briefly outlines the construction of this specimen along with a description of strain data gathered from its testing. Because the same ABAQUS modeling techniques were used for the specimen finite element analysis, comparison of model results and laboratory strain data allowed validation of the specimen model while providing basic insight into the modeling techniques used for all of the ABAQUS finite element models.

## **Chapter 6: Design and Finite Element Modeling of a Laboratory Stay Cable Specimen**

The next step in the assessment of bending fatigue damage to the stay cables of the Fred Hartman Bridge was the design and finite element modeling of a cable specimen for fatigue testing in the laboratory. The finite element program ABAQUS was implemented to model a series of possible specimen geometries. The specimen was designed to match the anchorage stress profile of the cable A22S model described in the previous chapter. The stress profile under the point of load application proved to be of equivalent concern, however. Ultimately, the combination of the specimen model and data from the laboratory testing allowed validation of the finite element modeling techniques.

### **Defined Specimen Parameters**

To simulate cable vibration in the laboratory, lateral excitation of a 20 – 40-foot (6 – 12-meter) stay cable specimen was proposed. Lateral motion was to be induced with a hydraulic ram cyclically loading the specimen at midspan (Figure 6.1). For ease of specimen construction and test execution, the cross-sectional geometry associated with the smallest of the Fred Hartman Bridge stay cables was chosen for the laboratory specimen. One of the final designs for the shortest group of stay cables on the bridge called for 19, grade 270, 0.6-inch (15-millimeter) diameter, seven-wire prestressing strands. The final structure was

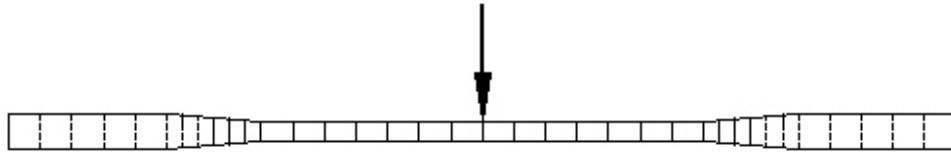


**Figure 6.1: Cable Stay Bending Fatigue Specimen**

built with 20 strands in each of these shorter stay cables, but the 19-strand design was retained for the specimen cross-section.

As with the bridge design, the specimen was to be prestressed to 445 kips (1980 kiloNewtons) and have grout diameters of 6.75 inches (171 millimeters) and 4 inches (100 millimeters) along the anchorage region and free length, respectively. Similar to the A24S and A22S models, the anchorage region was defined as the length of cable from the face of the anchorage plate to the beginning of the transition region, and the transition region was the 18-inch (460-millimeter) region that gradually reduced the grout section from the anchorage diameter to the free length diameter. The interface of the transition region with the free length was the location of the tension ring.

The intent of the laboratory tests was to have the specimen mimic the curvature and stress profiles incurred by the anchorage zones of the actual Fred Hartman Bridge stay cables. The peaks at the anchorage plate and tension ring of the cable A22S model best characterized the stress profiles (Figure 6.2). The dynamic excitation of the cable A22S model was determined to be a more realistic simulated vibration event based on the polyethylene sheath inspections. For this reason, an anchorage box opening was not replicated for the laboratory testing. Therefore, the local maximum of stress at the anchorage box opening was

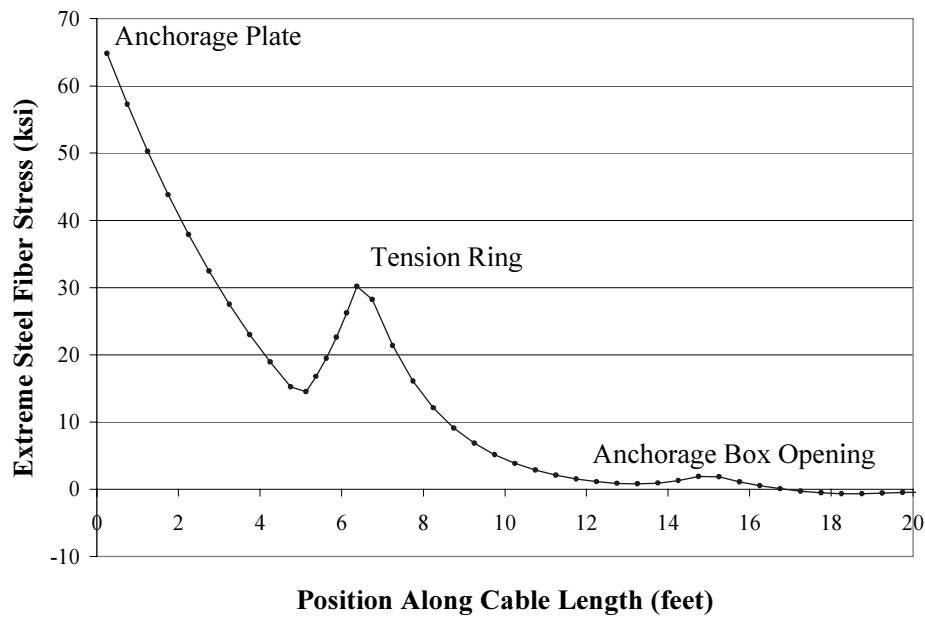


**Figure 6.2: Extreme Steel Fiber Stress Profile for 20 feet of Cable A22S Model  
Nearest the Deck Anchorage**

not considered when characterizing the anchorage zone stress profile derived from the finite element models.

As a consequence of the insignificant impact of the anchorage box opening on the computed results for the cable A22S model, this stress profile provided the basis for the criteria defining the profile of the first cable specimen. The two peak values were used to establish the ratio of stress at the anchorage plate to the stress at the tension ring. Based on the A22S results, three such ratios were calculated. The target steel stress, grout stress, and curvature ratios were all used to characterize the anchorage zone profile of a vibrating stay cable (Table 6.1). To model accurately the effect of cable vibration on the actual bridge



<b>Table 6.1: Target Ratios of Stress or Curvature at Anchorage Plate to Tension Ring for Peak Motion Results from Cable A22S Model</b>		
Curvature	Anchorage Plate	5.71E-07 in <sup>-1</sup>
	Tension Ring	5.11E-07 in <sup>-1</sup>
Target Curvature Ratio		1.12
Extreme Steel Fiber Stress	Anchorage Plate	64.8 ksi
	Tension Ring	30.2 ksi
Target Steel Stress Ratio		2.15
Extreme Grout Fiber Stress	Anchorage Plate	12.1 ksi
	Tension Ring	6.3 ksi
Target Grout Stress Ratio		1.92

structure, these target ratios were considered to be parameters for the first specimen to possess.

As indicated by the stress profile (Figure 6.2), the highest fatigue stress range existed at the anchorage plate. Because Figure 6.2 only represents one peak of motion, the stress range that the extreme steel fiber experienced in the model simulation was approximately twice the maximum shown, or nearly 130 kips per square inch (900 megaPascals). This fatigue stress range was not used as a parameter for the laboratory bending fatigue test because, as mentioned, the calculated stress results of the stay cable finite element models were higher than anticipated. Since validation from strain measurements on the bridge was not possible, the computed results were relied upon to obtain the target ratios, but a realistic estimate for the maximum fatigue stress range was not extracted from the

results. Instead, a range of 40 kips per square inch (280 megaPascals) was assigned as the target extreme steel fiber fatigue stress range for the first specimen based on the advice of Frank (2000).

### Specimen Variables

Constrained by the defined specimen parameters, several dimensions of the specimen geometry were varied so that the target ratios (Table 6.1) and fatigue stress range could be attained (Figure 6.3). The only defined length on the specimen was the transition region. The overall specimen length and the length of the anchorage region were left as variable parameters. Alteration of these dimensions was to aid in attaining an anchorage zone profile close to the target curvature and stress ratios. Additionally, all of the aspects of the testing configuration were unknowns. Variation of parameters such as the cycling frequency and displacement amplitude of the hydraulic ram influenced the desired fatigue stress range.

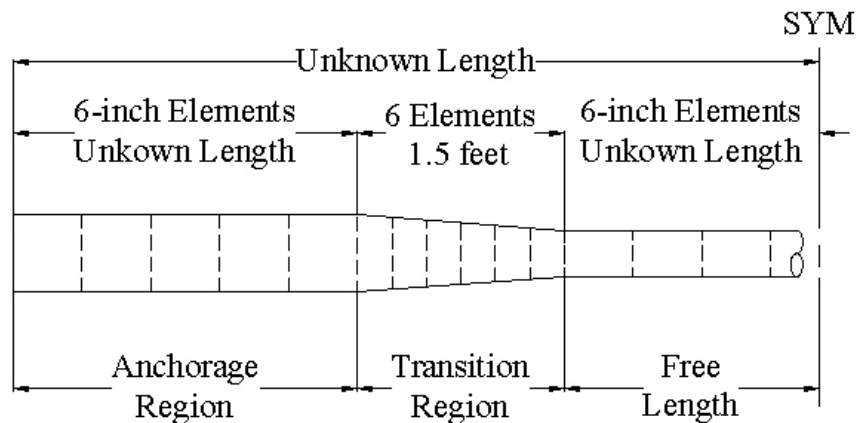


**Figure 6.3: Geometric Variable Parameters of the Specimen Model**

## **Modeling of the Specimen**

The specimen variables were studied using a series of finite element models created with ABAQUS. Each of these models possessed common properties and used similar modeling techniques as the cable A24S and A22S models. Each model was broken up into Timoshenko beam elements defined linearly with two nodes. The elements in the anchorage region and along the free length were 6-inches (150-millimeters) long while 3-inch (76-millimeter) beam segments formed the transition region (Figure 6.3). The composite cross-sectional properties for each of the linear elements were defined in terms of a transformed grout section. These properties were constant along the free length, but in the anchorage and transition regions, a grout diameter and strand profile that were averaged over the length of the individual element were used to calculate representative properties for an entire element.

### ***Model Properties and Analysis Details***

Consistent with the cable A24S and A22S models, the work of Willox (1998), and the work of Hamilton (1995), a modulus of elasticity of 27,600 kips per square inch (190 gigaPascals) was used for the steel strand, and a modulus of elasticity of 4000 kips per square inch (28 gigaPascals) was used for the grout. The grout was initially assumed to be uncracked, and any stiffness associated with the polyethylene sheath was neglected. The cable's end supports were modeled with rotational springs using a stiffness based on the resistance provided by the testing frame.

The specimen model was tensioned using the same prescribed condition approach described in Chapter 5, and the overall analysis was again divided into four steps. Step one involved attaching the ends of the cable to the rotational springs. The second step statically applied the specimen's self-weight. The third step extracted the modal frequencies of the tensioned cable, and step four dynamically excited the specimen model based upon chosen values for the cycling frequency and displacement amplitude of the hydraulic ram. The structural analysis again included geometrically nonlinear terms in the stiffness matrix but neglected any material nonlinearity.

Similar to the cable A24S and A22S models, a consequence of the linear mesh modeling technique was that a stress profile for a given cross-section could not be directly produced by ABAQUS. Therefore, all stress profiles were calculated using Equation 6.1 based upon the curvature,  $\phi$ , provided by the analysis.

$$\sigma(y) = \phi y E(y) \quad \text{Equation 6.1}$$

The stress a distance  $y$  from the centroid is represented by  $\sigma(y)$ , and  $E(y)$  denotes the modulus of elasticity at location  $y$ . Equation 6.1 assumes elastic behavior and that no slip occurs between the strand and uncracked grout.

### ***Intermediate Iteration Results***

Figure 6.4 shows an extreme steel fiber stress plot for the anchorage zone of a typical candidate specimen. The overall and anchorage region lengths were 28 feet (8.5 meters) and 4 feet (1.2 meters), respectively. Excitation was at 1.5 Hertz with an amplitude of  $\pm 1.5$  inches (38 millimeters). The fatigue stress range

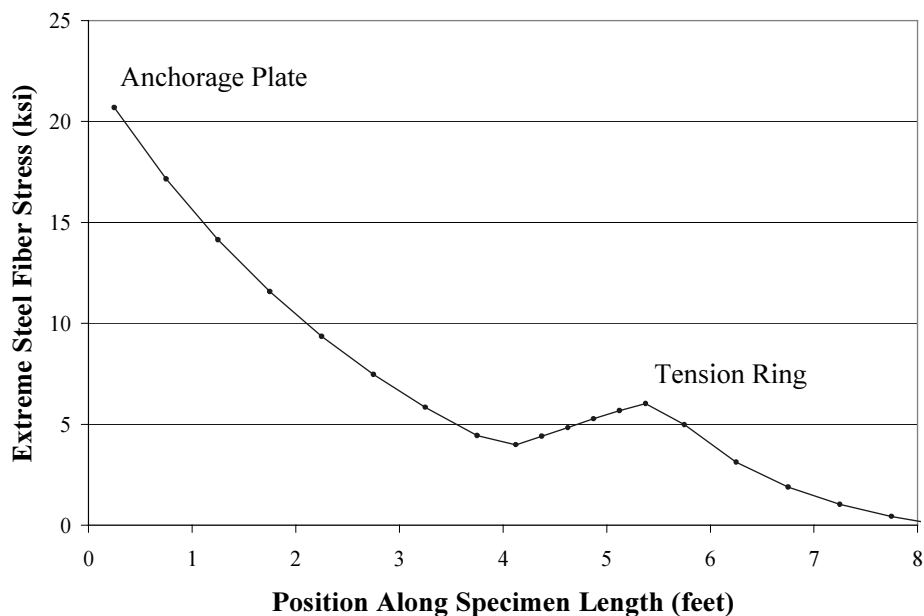


**Figure 6.4: Typical Specimen Steel Stress Profile in the Anchorage Zone for a Peak of Motion**

at the anchorage plate of approximately 40 kips per square inch, or  $\pm 20$  kips per square inch (280 megaPascals or  $\pm 140$  megaPascals), was readily controlled with the displacement amplitude of the hydraulic ram.

When compared to the cable A22S anchorage zone profile of Figure 6.2, the maximum at the tension ring of the specimen in Figure 6.4 was not as pronounced. In fact, the ratio of anchorage plate stress to tension ring stress for this specimen geometry was 3.44, well above the 2.15 target ratio for steel stress. If the cable were prismatic, the stress profile would consist of a decreasing slope from the anchorage. The source of the tension ring peak was the change in cross-sectional geometry through the transition region. Therefore, moving the transition

region closer to the anchorage plate (shortening the length of the anchorage region) would result in an increase in the tension ring stress value.

The overall length of the specimen also affected the tension ring stress magnitude. Again assuming the cable to be prismatic, the decreasing slope of the stress profile away from the anchorage plate became steeper as the overall specimen length was reduced. Therefore, a longer specimen had a higher tension ring stress than a shorter specimen assuming equal anchorage region length. The geometry of the specimen was altered until a 32-foot (9.8-meter) specimen with a 2.5-foot (0.76-meter) long anchorage region provided anchorage plate to tension ring ratios approaching the target values.

### **Modeling of the Ram Clamp for Dynamic Excitation**

Figure 6.5 shows the steel stress profile for the entire specimen from the same candidate specimen as Figure 6.4. The dominating feature of the plot is the pair of stress spikes at the center of the specimen. These peaks are the result of the excitation of the specimen model. The cable A24S and A22S models also exhibited stress spikes due to the excitation method. For these models, the free length portion of each cable was neglected because the analysis focused on the anchorage zones. For the specimen, however, the stress profile along the entire length was important to ensure fatigue-testing accuracy. If the fatigue stress range under the ram exceeded the stress range at the anchorage plate, failure could occur at midspan, and the bending fatigue test would not model the response of the actual Fred Hartman Bridge stay cables accurately. The lateral excitation of

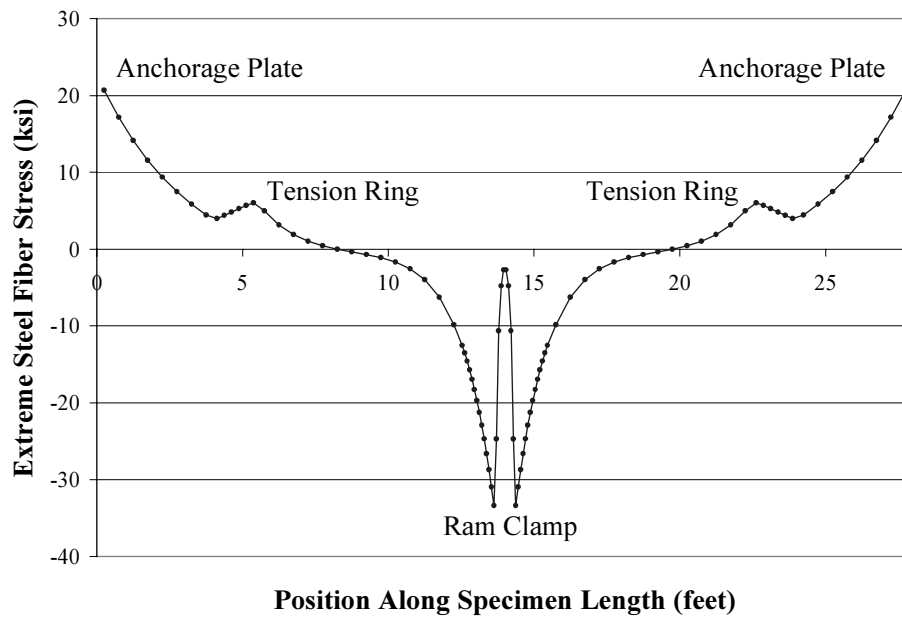


**Figure 6.5: Typical Specimen Steel Stress Profile for a Peak of Motion**

the actual specimen with the hydraulic ram needed to be modeled as carefully as the specimen itself to get a reliable stress profile. This requirement implied two tasks: 1) devise a suitable method for clamping the cable to the ram, and 2) model that method accurately.

***Direct Displacement Control***

The preliminary specimen models (including the model providing the stress profile for Figure 6.5) assumed that the ram clamp would rigidly grip the specimen over a specified distance. Thus, lateral motion was simply produced through displacement control of several center nodes. Figure 6.6 shows the effect of varying the length of the clamp using this excitation method with a 20-foot (6-

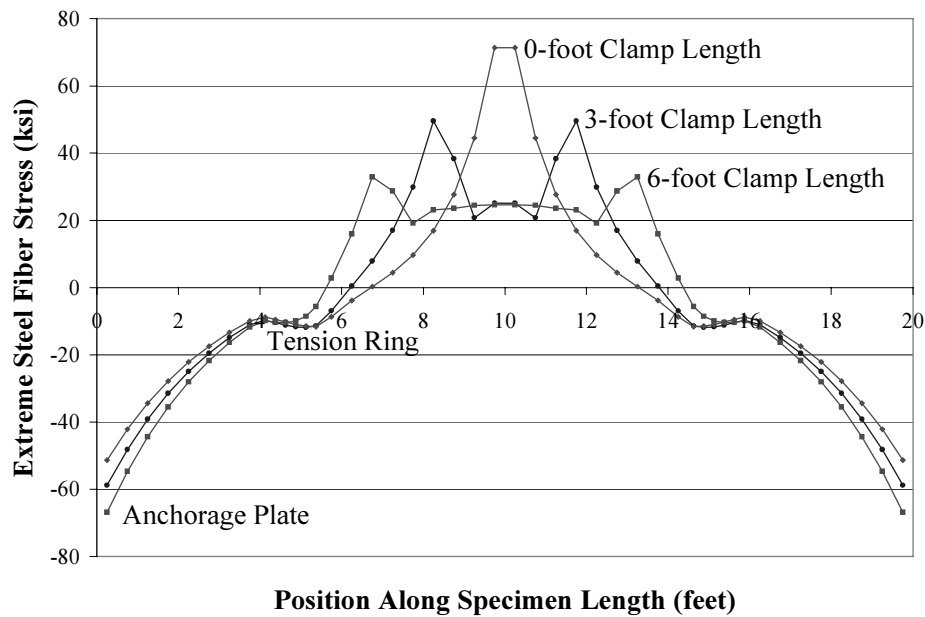


**Figure 6.6: Effect of Ram Clamp Length on Steel Stress Profile When Using Direct Displacement Control**

meter) specimen model. The clamp length indicates the dimension of the center portion of cable that was excited using direct displacement control. The *0-foot Clamp Length* corresponded to a displacement control occurring at the single center node only. The plateau at the peak of the *0-foot Clamp Length* curve was due to the manner in which the stress profile was calculated. As described, the profile was directly calculated from the curvature profile using Equation 6.1. Curvature is a property of an element and not a node. Therefore, the single center point excitation created a symmetric curvature profile with equal curvature values for both elements defined using the center node, creating the plateau exhibited in Figure 6.6.



For each curve in Figure 6.6, the spikes in stress occur just to either side of the ram clamp region. This behavior was due to the high curvature associated with the kinks in the cable produced at these locations. As the ram clamp length increased, the magnitude of the stress spike decreased. The stress values, however, were still quite large compared to the stresses at the anchorage plate and tension ring. While for some larger clamp lengths, the stress induced by the ram was less than the anchorage plate stress, the actual conditions of the experiment had to be considered. A 6-foot (1.8-meter) ram clamp length was not a practical solution for a 20-foot (6-meter) specimen. Additionally, it was unrealistic to assume that a single hydraulic ram load would be distributed evenly over a 6-foot (1.8-meter) clamp. Therefore, other modeling solutions were sought.

#### ***Contact Surfaces with Internal Curvature***

To reduce the stress concentrations produced by the ram grip, the literature suggests a clamp with an internal radius. For example, Raoof (1992 and 1993) performed bending fatigue tests on spiral strands in this manner. To investigate the applicability of this approach to the stay cable specimen, contact surfaces were used to model this type of a clamp in ABAQUS.

ABAQUS allows the user to specify surfaces on modeled bodies that will come into contact with one another. One of these contact surfaces is the *master surface*, and the other is the *slave surface*. The *slave surface*, a deformable body, reacts to the *master surface*, the stiffer of the two bodies. Just as the parameter *HAFTOL*, described in Chapter 5, controls the accuracy of a dynamic analysis, the parameter *HCRIT* specifies the accuracy of a contact analysis. As contact occurs,

the distance that the *slave surface* has penetrated the *master surface* measures the tolerance of the analysis. A high *HCRIT* value allows deeper penetration and a less accurate analysis.

A ram clamp with internal curvature was modeled as a pair of parabolic rigid surfaces (Figure 6.7). The top half of the clamp acted as the *master surface* for the top of the specimen, defined as a *slave surface*. Similarly, the bottom half of the clamp acted as the *master surface* for the bottom of the specimen, also defined as a *slave surface*. The parabola used to define a clamp half was forced to meet the length and depth constraints illustrated in Figure 6.7. The testing frequency and amplitude associated with the hydraulic ram were then assigned to the clamp using displacement control.

Figure 6.8 displays typical results for a 20-foot (6-meter) model. Stress concentrations in the clamp region were still observed. Note that the ABAQUS mesh was refined in the clamp region to 1-inch (25-millimeter) beam elements. To minimize the magnitudes of the stress peaks, the radius of the clamp was varied by altering the clamp depth. A large clamp depth, such as the 3.24-inch (82-millimeter) depth, denoted a smaller clamp radius of curvature. The deeper the clamp became, the more the excitation resembled a point load because less of the clamp made contact with the specimen. At the other end of the spectrum, a shallow clamp depth, such as the 0.25-inch (6-millimeter) depth, signified a larger

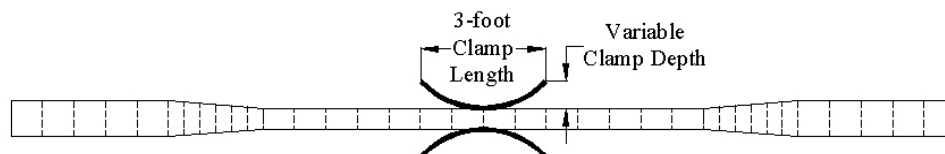


**Figure 6.7: Specimen and Clamp with Internal Curvature**

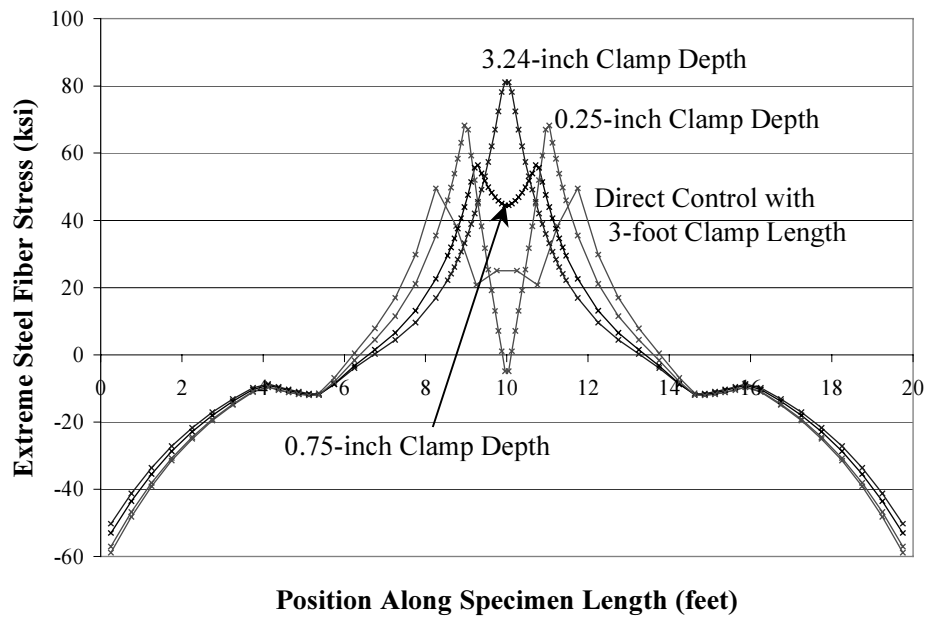


**Figure 6.8: Effect of Ram Clamp Internal Curvature on Steel Stress Profile  
When Using Contact Surface Control**

clamp radius of curvature. The shallower the clamp became, the greater the contact area between the clamp and the specimen. This contact forced the specimen to match the curvature of the clamp until the stress profile more closely resembled the results of the direct displacement control method (Figure 6.8).

The steel stress profile for the 0.75-inch (19-millimeter) ram clamp depth in Figure 6.8 illustrated that an optimum clamp curvature could possibly be attained that minimized the stress concentrations in the region. Of the stress profiles produced from a contact analysis, the stress peaks for this 0.75-inch (19-millimeter) clamp depth profile were the lowest in the figure. The peak values were, however, still larger than those corresponding to the direct displacement control analysis that did not use contact surfaces or internal clamp curvature.

Further iteration showed that significant reduction of the peak stress magnitudes could not be made within the allowable manufacturing tolerance for a clamp with a specified internal curvature. Because the analytical results did not warrant the difficult manufacture of such a clamp, the focus shifted to modifications of the specimen itself to better withstand the higher stresses in the ram clamp region.

### ***Stepped Midspan Grout Section***

Efforts to minimize the effect of stress concentrations near the point of cyclic loading, by strengthening the specimen at midspan, included an analytical investigation of the efficiency of increasing the midspan grout diameter (Figure 6.9). For this investigation, the larger cross-sectional area used at midspan possessed the same grout diameter of 6.75 inches (171 millimeters) as the anchorage region, but unlike the anchorage region, the strands along the midspan were straight. Therefore, while the two cross-sections had the same area, the larger midspan section maintained a lower composite moment of inertia. The ram excitation was modeled using direct displacement control along the center 8 inches (200 millimeters) of the specimen.

Figure 6.10 displays typical results for a 28-foot (8.5-meter) model. For comparison, the *0-foot Stepped Length* indicates a model with no stepped region. For the models with stepped grout regions, stress concentrations just to the side of

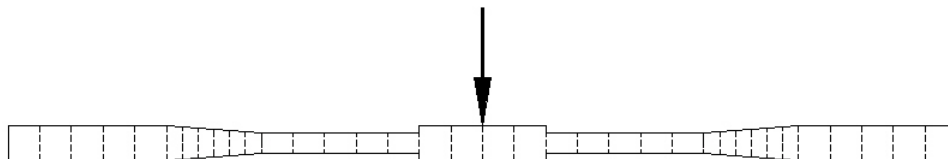


**Figure 6.9: Specimen with Stepped Midspan Grout Section**

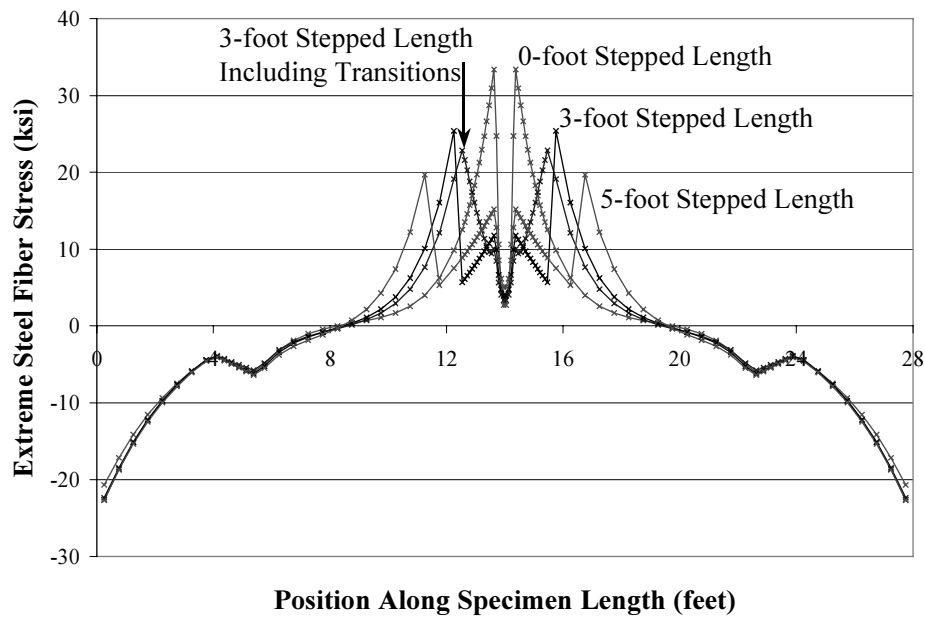


**Figure 6.10: Effect of Midspan Stepped Grout Diameter Length on Steel Stress Profile**

the ram were reduced significantly, but stress peaks at the edges of the stepped section dominated the response. To optimize the steel stress profile, the length of the stepped region was varied. As the length of the stepped section increased, the stress magnitudes at the edges of the stepped region decreased, but the stress spikes next to the ram grew. An alternate method of reducing the stress magnitudes at the edges of the stepped section, by including a 12-inch (300-millimeter) transition region on either side of the stepped portion of cable, did not produce significantly different results (Figure 6.10).

The 5-foot (1.5-meter) stepped length shown in Figure 6.10 was near the optimum length where the stress concentration next to the ram was approximately equivalent to the stress peak just beyond the edge of the stepped region.

Additionally, the 5-foot (1.5-meter) stepped region was considered a reasonable upper bound for the length of the clamp region so that the additional stiffness did not affect the response of the specimen at the anchorages. While stress spikes still existed, the specimen design continued based on the assumption that the extreme peak of the stress concentration would not be fully realized in an actual test.

### ***Ram Clamp with Graduated Stiffness***

The geometric and testing parameters of the stay cable specimen were all chosen based upon the model with the 5-foot (1.5-meter) long increased cross-section at midspan, but construction tolerances prevented this approach from being employed. Instead, the ram clamp designed for the first laboratory test is shown in Figure 6.11. The clamp attempted to distribute the ram force over a 26-inch (660-millimeter) midspan region with decreasing clamp stiffness away from the ram connection. The ram, connected to a 10-inch (250-millimeter) long, flat

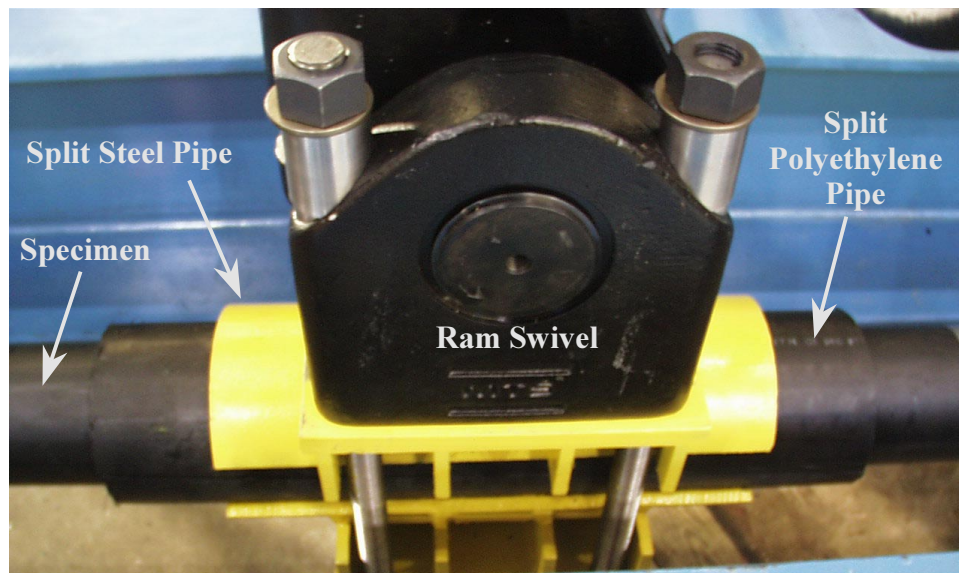


**Figure 6.11: Ram Clamp Used for First Laboratory Fatigue Test**

steel plate, transferred load through the plate and into a series of vertical stiffeners. The stiffeners transmitted the ram force into an 18-inch (460-millimeter) long, split steel pipe. The steel pipe then transferred the load into a 26-inch (660-millimeter) long, split polyethylene pipe, fitting directly over the stay cable specimen (Figure 6.12).

This clamp was modeled as a series of twenty-seven parallel linear

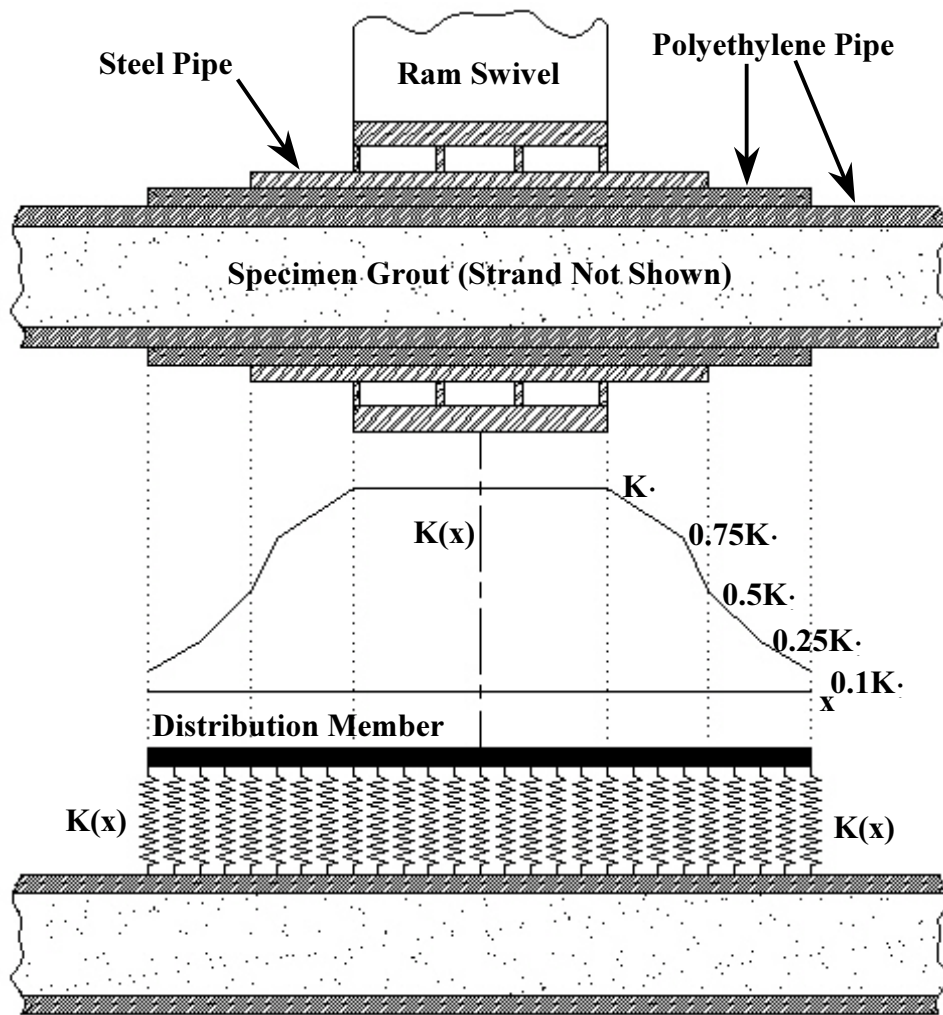


**Figure 6.12: Cross-Section and Modeling Approach for Ram Clamp Used for First Laboratory Test**

springs with stiffness coefficients chosen to represent the decreasing stiffness of the clamp as a function of the distance,  $x$ , from the ram centerline (Figure 6.12). Each spring connected a specific node in the clamp region of the model to a common distribution member. The springs representing the portion of the clamp directly below the ram were assigned a stiffness of  $K_c$ , denoting that motion of the distribution member results in similar motion of the cable. The stiffness for each spring along the clamp was then assigned as a fraction of  $K_c$  (Figure 6.12). The magnitude of  $K_c$  was not defined so high as to cause fractions of the value to also behave as an infinite stiffness. A  $K_c$  value of 200 kips per inch (35 kiloNewtons per millimeter) allowed a 0.002-inch (0.05-millimeter) discrepancy between the specimen and the distribution member at the center spring. This representation of the ram clamp was used to attain preliminary stress profile predictions for the first laboratory test.

### **Preliminary Stress Profile Predictions Before Start of First Laboratory Test**

Using the geometric and testing constraints, the specimen variables were determined. The optimal lengths of the anchorage region and the overall specimen were 2.5 feet (0.76 meter) and 32 feet (9.8 meters), respectively. A hydraulic ram stroke of 61.6 inches (641 millimeters), with a corresponding predicted ram force range of approximately 20 kips (89 kiloNewtons), was required to produce a steel fatigue stress range of approximately 40 kips per square inch (280 megaPascals). Figure 6.13 presents an envelope of the predicted extreme steel fiber stress profile during cycling. The upward and downward



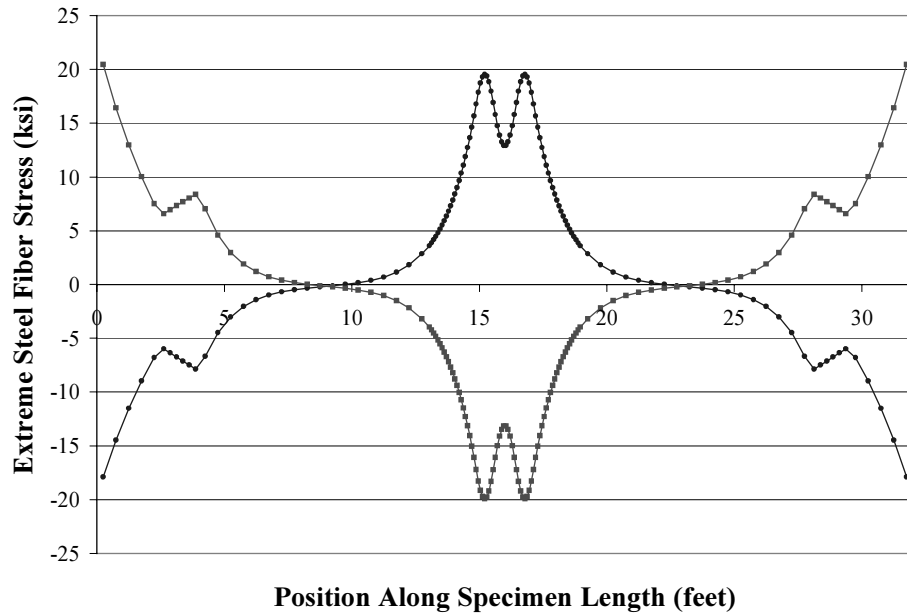


**Figure 6.13: Predicted Extreme Steel Fiber Stress Profiles for Peaks of Motion  
– Uncracked Model**

peaks of motion are represented. Similarly, Figure 6.14 illustrates the expected extreme grout fiber stress profiles. Despite considerable effort, the stress concentrations induced by the ram were still significant, and only the actual test could determine if the majority of failure would occur at this location instead of at one of the critical locations being investigated.

Both stress profiles indicated that the predicted response of the specimen’s anchorage region matched the response of the cable A22S model’s anchorage reasonably well. Table 6.2 compares the curvature and stress profiles of the cable A22S model and the specimen model. The specimen ratios were all

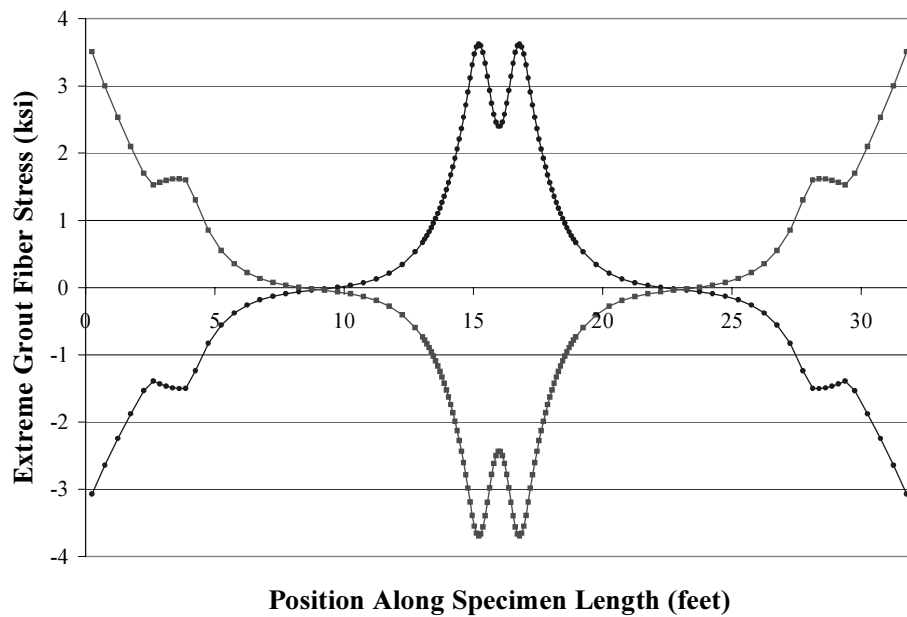


**Figure 6.14: Predicted Extreme Grout Fiber Stress Profiles for Peaks of Motion  
– Uncracked Model**

above the corresponding target ratios, signifying a slightly higher gradient at the anchorage of the test specimen.

The first stay cable bending fatigue test at Ferguson Structural Engineering Laboratory tested the accuracy of the finite element model, prompting improvements to be made, primarily by modeling portions of the cable as having cracked grout. The bending fatigue test, the validation of the ABAQUS analysis, and improvements to the specimen finite element model are discussed in the following chapter.

<b>Table 6.2: Comparison of Curvature and Stress Profiles for Specimen and Cable A22S Models</b>			
		Cable A22S Model	Specimen Model
Curvature	Anchorage	5.71E-07 in <sup>-1</sup>	2.60E-04 in <sup>-1</sup>
	Tension Ring	5.11E-07 in <sup>-1</sup>	1.89E-04 in <sup>-1</sup>
Curvature Ratio		1.12	1.38
Extreme Fiber Steel Stress	Anchorage	64.8 ksi	20.5 ksi
	Tension Ring	30.2 ksi	8.37 ksi
Steel Stress Ratio		2.15	2.44
Extreme Fiber Grout Stress	Anchorage	12.1 ksi	3.51 ksi
	Tension Ring	6.3 ksi	1.60 ksi
Grout Stress Ratio		1.92	2.19

## **Chapter 7: Finite Element Model Adaptation and Validation Through a Bending Fatigue Test of a Stay Cable Specimen**

The stay cable specimen whose design and modeling was detailed in Chapter 6 was constructed and tested in a bending fatigue test at Ferguson Structural Engineering Laboratory. Experimentally measured stress ranges and displacements provided the basis for a validation of the specimen's uncracked finite element model. The specimen model was then adapted based upon experimental observation of cracking, to obtain analytical results closer to the experimentally measured values.

### **Description of the Bending Fatigue Test**

The 32-foot (9.8-meter), nineteen-strand stay cable specimen was fabricated following a process similar to the one used during construction of the Fred Hartman Bridge. Segments of polyethylene pipe were attached end-to-end, using a plastic welding technique, to form the outer sheath of the specimen. The nineteen steel strands were next threaded through the anchorage assemblies and the polyethylene sheath (Figure 7.1). The ungrouted specimen was then tensioned within a compression frame designed by Poser (2001). The following fabrication step involved inclining the entire reaction frame at an angle similar to the cables on the bridge so that the specimen could be injected with grout. A thesis by Poser (2001) will provide a more detailed description of the construction process.



**Figure 7.1: Installation of Strand During Construction of Stay Cable Specimen**

Following a week of grout curing and instrumentation preparation, the specimen, positioned horizontally, was cyclically loaded using a hydraulic ram attached to the specimen at midspan with the ram clamp discussed in Chapter 6 (Figure 7.2). An acoustic monitoring system detected the occurrence of wire breaks and the location along the length of the specimen at which the wire breaks occurred. Over 2.8-million cycles produced fourteen wire breaks in one anchorage and eleven wire breaks near the ram clamp. No wire breaks were identified by the acoustic monitoring system in the other anchorage. More details, including the results of a post-mortem investigation, may again be found in the work of Poser (2001).



**Figure 7.2: Stay Cable Bending Fatigue Test**

### **Strain Collection Instrumentation**

Two strain gage varieties monitored strain ranges at critical points along the length of the specimen so that the fatigue stress ranges incurred by the specimen during the laboratory test could be experimentally determined. Figure 7.3 shows the locations of strain gages on the stay cable specimen. Gages were positioned in every location that the finite element modeling indicated a stress maximum or minimum: near the anchorage plate, on the anchorage region prior to the transition region, and on the free length just passed the tension ring. The series of gages near the ram clamp provided information about stress

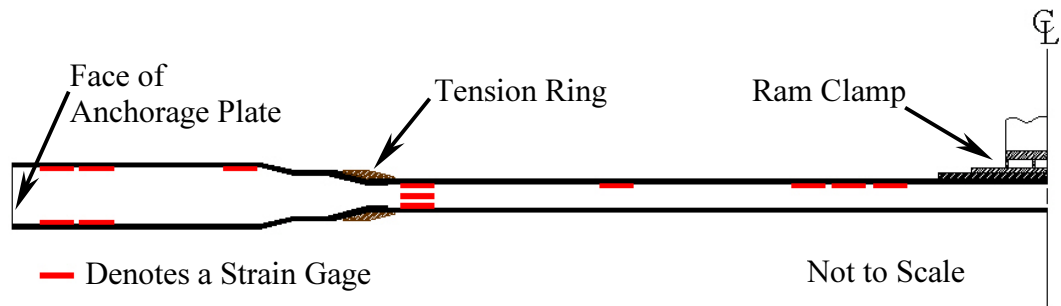


**Figure 7.3: Locations of Strain Gages for First Stay Cable Specimen**

concentrations produced by the excitation. The single gage along the free length between the ram clamp and the tension ring was intended to provide axial strain data.

The majority of the gages were 2.4-inch (60-millimeter), 120-Ohm concrete strain gages of the variety initially used on the Fred Hartman Bridge stay cables. After curing of the grout, windows were cut in the polyethylene sheath at the desired strain gage locations. Each gage was adhered to the grout surface using a thin layer of a quick-setting cold weld compound (Figure 7.4). Due to the reaction frame, however, the gages near the anchorage plate were not accessible after tensioning and grouting. A different variety of strain gage was needed. Prior to assembly of the cable stay specimen, 0.5-inch (12-millimeter), 120-Ohm strain gages, designed to be embedded in concrete, were installed on the inside surface of the polyethylene sheath. The gages were mounted, using the same cold weld compound, near the end of the sheath so that they would be near the anchorage plate in the completed specimen (Figure 7.5).

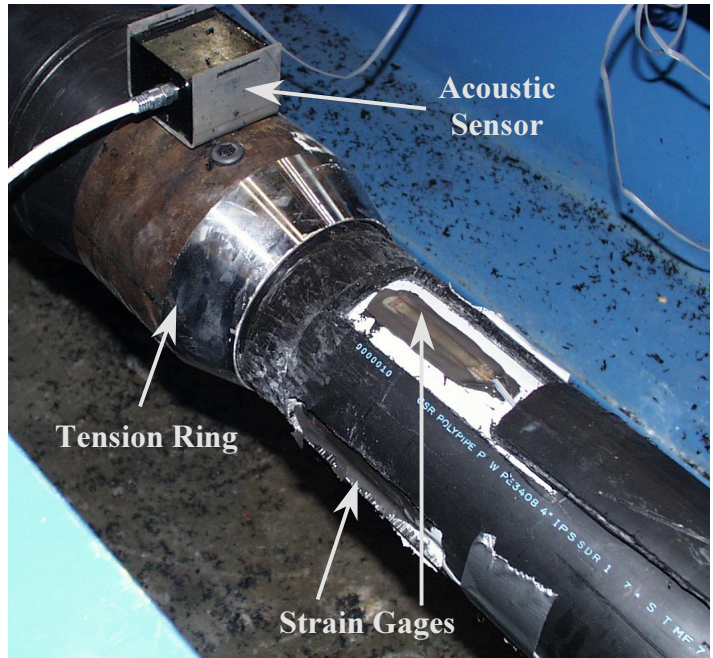


**Figure 7.4: Strain Gages Near the Tension Ring**

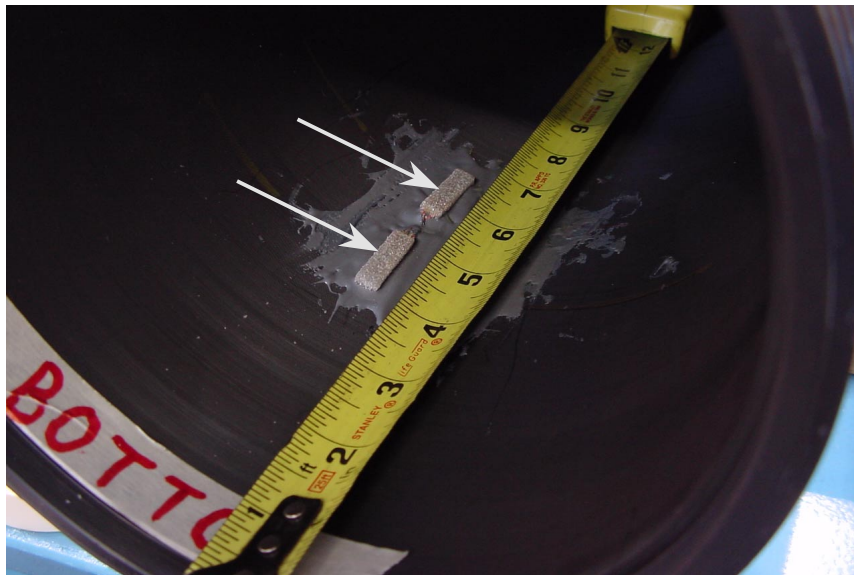


**Figure 7.5: Strain Gages Near the Anchorage Plate**



## Experimental Results

Strain data from all of the gages were gathered at a sampling rate of 50 Hertz with the mobile data acquisition unit used on the Fred Hartman Bridge. The initial cycle of the test was performed slowly enough to be considered a static test. Strain information from dynamic cycles was then collected at numerous time intervals throughout the length of the test.

### *Static Test Strain Results*

The first part of the static test involved pulling the cable up to a displacement of 1.6 inches (41 millimeters). This deformation required the ram to impart a load of 7.79 kips (34.7 kiloNewtons). Figure 7.6 illustrates the measured strain associated with the top gage from several of the key strain gage locations. The top of the specimen near the tension ring and near the anchorage plate

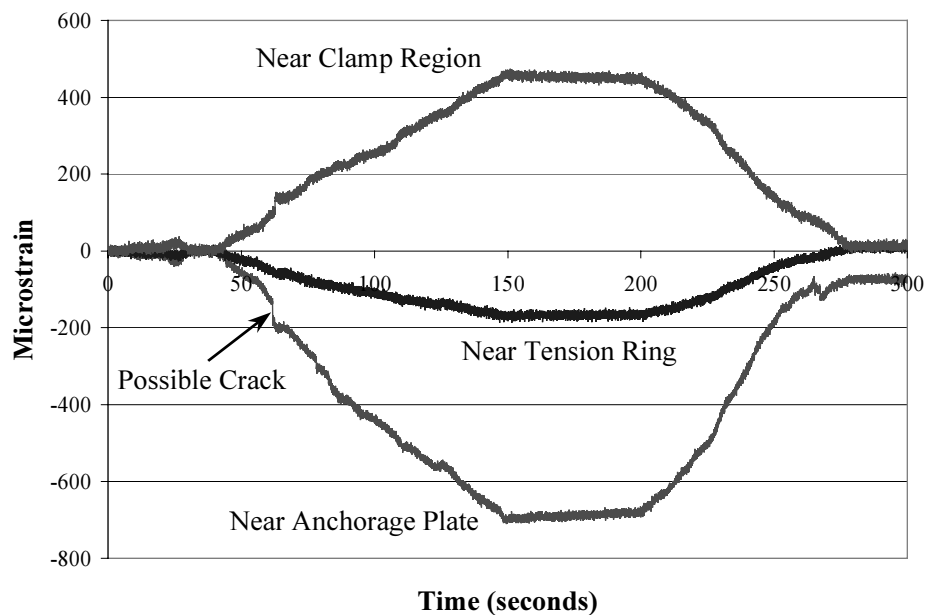


**Figure 7.6: Top Gage Strain Histories for Upward Motion of the Static Test**

experienced compression while the top of the cable near the clamp region went into tension. This trend indicates a point of inflection between the clamp and the tension ring. Therefore, the anchorage did behave with a significant amount of fixity.

Figure 7.6 also demonstrates that the strain near the anchorage plate exceeded the strain near the tension ring, as expected. The strain near the ram clamp was very high, but it was lower than the anchorage plate strain. The strain for the gage located on the anchorage region prior to the transition region was not shown because it plots almost on top of the strain from the gage near the tension ring. The anchorage plate strain in Figure 7.6 did not appear to return to zero upon unloading. This feature may have been the result of cracks forming in the grout surrounding the gage. In fact, such a crack may have developed at a time of approximately 60 seconds, causing a sharp, concentrated increase in the strain magnitude. All gages in a specific location, such as the three gages near the ram clamp, exhibited similar trends with slightly varying magnitudes. For example, the measured results in Figure 7.6 for the gage location near the ram clamp were associated with the middle of the three gages. These gages displayed an increasing strain profile towards the clamp.

The second part of the static test involved pushing the cable down to a displacement of -1.6 inches (-41 millimeters). This deformation required the ram to impose a load of 7.67 kips (34.1 kiloNewtons). Figure 7.7 illustrates the measured strain associated with the top gage from several of the key strain gage locations. The trends were very similar to those shown in Figure 7.6 but with

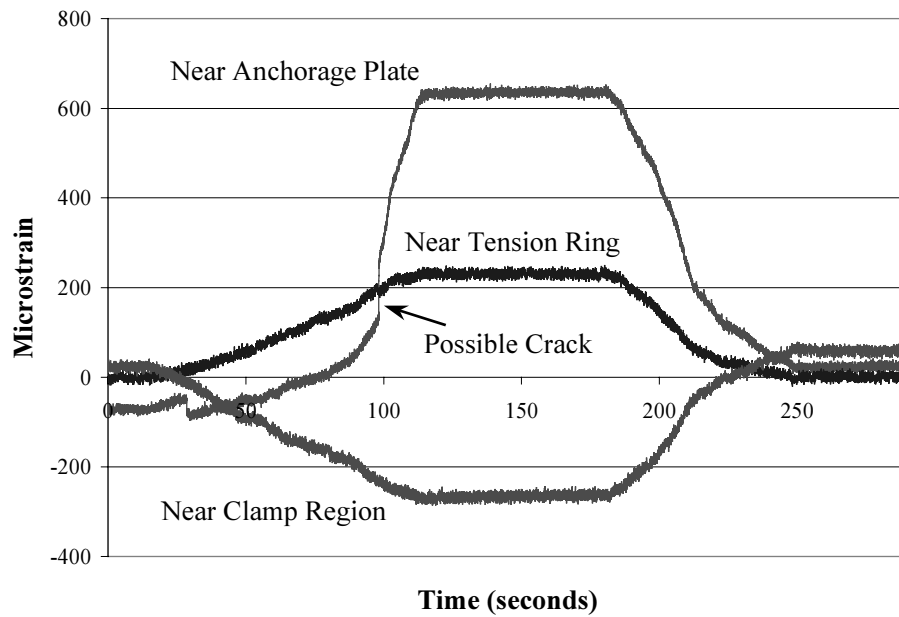


**Figure 7.7: Top Gage Strain Histories for Downward Motion of the Static Test**

opposite signs. The top of the anchorage region experienced tension for this half of the static test instead of compression as in the first half. The rate of increase of the strain near the anchorage plate displayed unique behavior. At approximately 100 seconds, the rate increased dramatically. This feature may again be due to a crack developing in the grout surrounding the gage. By this point in the test, some strain gages, such as the one prior to the transition region, were failing to provide reliable results, presumably due to cracking.

***Sample Dynamic Test Strain Results***

As the test progressed, more gages were lost due to cracking, but strain data for most of the critical specimen locations were intermittently gathered as

late as 2.6 million cycles into the fatigue test. Figure 7.8 displays a typical plot of strains measured during test execution. Each curve was sinusoidal, and the relative magnitudes remained similar to those observed during the static test. The anchorage plate strain was still higher than the strain near the tension ring, and the strain near the ram clamp remained between these two strain measures. Figure 7.8 shows data from a combination of bottom and top gages, as noted, due to the loss of numerous gages as a result of grout cracking.

***Deterioration of Stress Ranges***

Strain data were collected several different times during the course of the first bending fatigue test. Consistent with the assumptions made for the analysis of the cable using the transformed section concept, the strain values obtained for the extreme grout fiber were translated into extreme steel fiber stress using

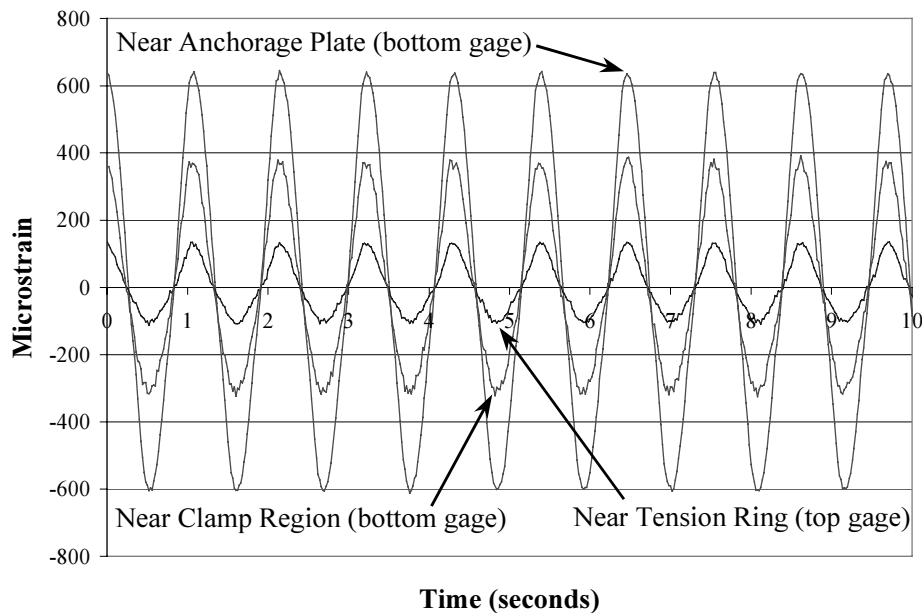


**Figure 7.8: Strain Histories During Cycling at 77,000 Cycles**

Equation 7.1.

$$\sigma_{steel}(x) = \varepsilon_{test}(x) \frac{y_{steel}(x)}{y_{grout}(x)} E_{steel} \quad \text{Equation 7.1}$$

Where  $\sigma_{steel}(x)$  represents the extreme steel fiber stress at a location,  $x$ , along the length of the specimen,  $\varepsilon_{test}(x)$  indicates the strain value obtained from the laboratory test at the same location, and  $y_{steel}(x)$  denotes the distance from the centroid of the cross-section at  $x$  to the extreme steel fiber. Similarly,  $y_{grout}(x)$  denotes the distance from the centroid of the cross-section at  $x$  to the extreme grout fiber. Finally,  $E_{steel}$  indicates the modulus of elasticity of the steel strand, taken as 27,600 kips per square inch (190 gigaPascals).

The extreme steel fiber fatigue stress ranges at the critical locations along the specimen's length were investigated at every measurement interval. Figure 7.9 illustrates both the relative magnitudes of each location's stress range and how each stress range deteriorated as the test progressed. All of the stress ranges declined progressively throughout the majority of the test. The stress range near the tension ring actually rose again during the later cycles. This phenomenon may have been the result of a redistribution of stress in the specimen due to damage incurred, or, more likely, the strain gage may have been damaged to a point of unreliability.

### **Validation and Adaptation of the Specimen Finite Element Model**

The finite element model of the stay cable specimen discussed in Chapter 6 included the assumption that the grout remained uncracked. Visual and audible observations, along with the early loss of many strain gages, indicated that this

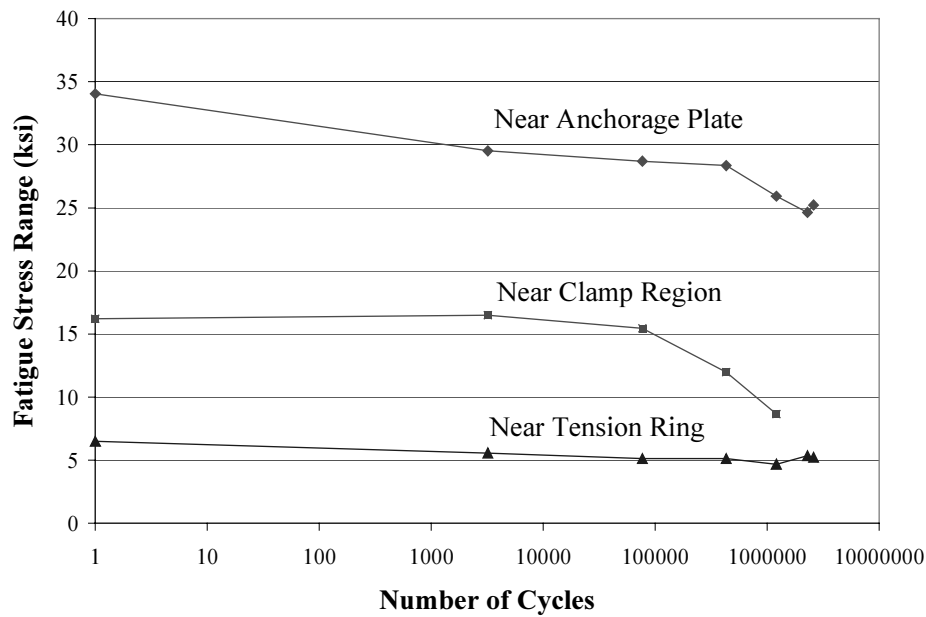


**Figure 7.9: Deterioration of Extreme Steel Fiber, Fatigue Stress Ranges**

assumption was primarily false. Consequently, the uncracked finite element model was adapted to include varying degrees of cracking, and the results were compared with experimentally determined deflections and stress ranges.

A specimen model containing only steel strand, with no grout, was investigated so that this analysis, coupled with the uncracked analysis, could bound the computed results. Additionally, other degrees of cracking were examined. For one analysis, a traditional cracked section, ignoring only the tension zone of grout, was used for every element. Other models neglected the grout strength at each of the end anchorage region elements, modeling the scenario of grout damaged beyond compressive load carrying ability. Still

another model accounted for wire breaks in the anchorage. Table 7.1 outlines the parameters of each model.

***Comparison of Models to Measured Data Using Displaced Shape***

The range of the displaced shape along the length of the specimen indicated the level of agreement for each model. All of the models were forced to maintain the same displacement range at midspan as the stay cable specimen. Generally, each of the six models followed the trend of the measured displacements (Figure 7.10). The actual displacements were obtained using a dial gage at regular intervals along the cable’s length, 870,000 cycles into the test. To provide an overall view of the agreement, Figure 7.10 does not differentiate between the individual models. Rather, focusing on the 5-foot (1.5-meter) region closest to one of the specimen’s ends allowed the models to be compared (Figure

<b>Table 7.1: Schedule of Specimen Finite Element Models Based on Degree of Cracking</b>			
Model ID	Crack Status of Specified Elements		
	Elements Near Face of Anchorage Plate	Elements Next to Ram Clamp	Remainder of Elements
1	Uncracked	Uncracked	Uncracked
2	No Grout	No Grout	No Grout
3	Tension Zone Cracked	Tension Zone Cracked	Tension Zone Cracked
4	No Grout	Tension Zone Cracked	Tension Zone Cracked
5	No Grout	No Grout	Tension Zone Cracked
6	No Grout/Wire Breaks	No Grout	Tension Zone Cracked

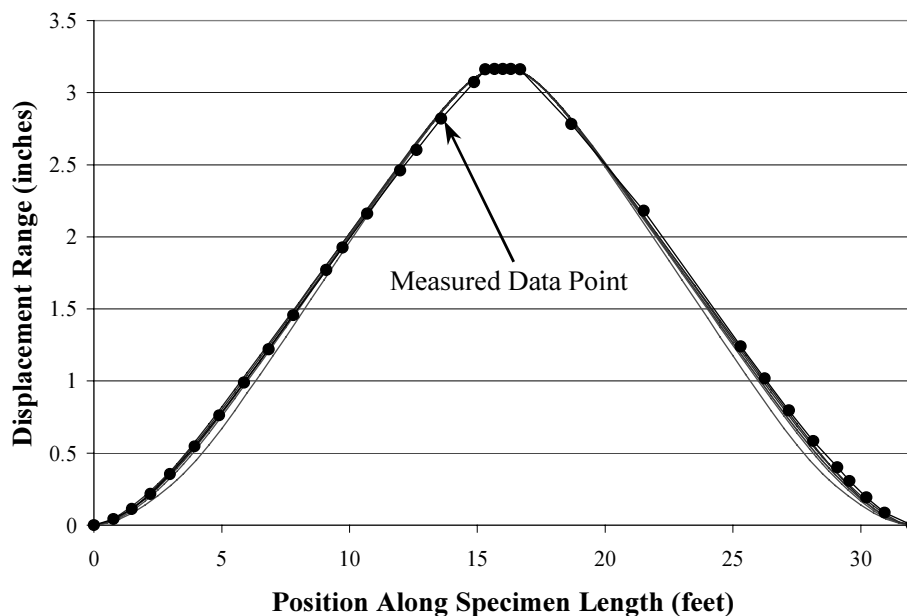


**Figure 7.10: General Agreement of Specimen Models to Measured Data Based Upon Displacement Range**

7.11). In this localized region, all of the displacement range profiles (including the measured ones) were generally bounded by the uncracked analysis (Model 1) and the analysis considering only the steel strand (Model 2). An exception to this trend was Model 6 over the last 3 feet (0.9 meters) of the specimen.

The end of the cable depicted in Figure 7.11 had not experienced wire breaks at the time of measurement. Model 6 was the only model to consider wire breaks. The top and bottom seven-wire strand at each of the two elements at the face of an anchorage plate, totaling 14 wires per section, were removed from the model. A major consequence of the wire breaks was the loss of the prestress carried by these wires. The initial tension of 445 kips (1980 kiloNewtons) was reduced to 398 kips (1770 kiloNewtons), decreasing the overall stiffness of the



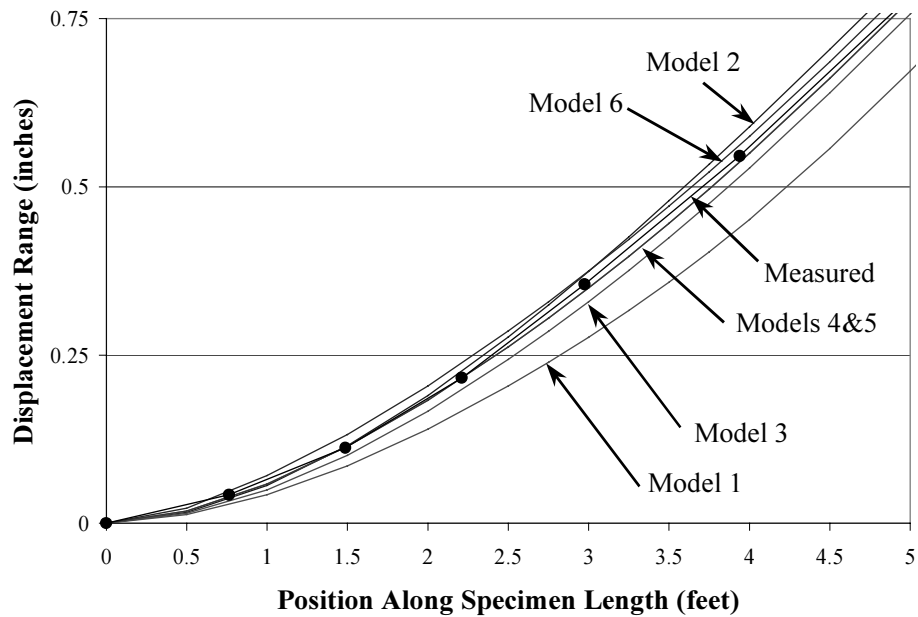


**Figure 7.11: Agreement of Specimen Models to Measured Data Based Upon Displacement Range Near Anchorage Without Wire Breaks**

cable structure. The order of the displacement range profiles in Figure 7.11 also provided an indication of the relative stiffness of the models in this region of the specimen. The model with the most stiffness (the uncracked Model 1) had the smallest displacement range. Conversely, the analyses completely neglecting the grout (Model 2) and considering wire breaks (Model 6) went through larger displacement ranges and, thus, possessed lower stiffness.

Models 4 and 5 have nearly identical displacement range profiles. Both models possessed groutless elements at the face of the anchorage plate. The only difference between the two models was the further reduction in the cross-sections next to the ram clamp from *tension zone cracked* to *no grout* (Table 7.1). The

agreement of these two models demonstrated the possible lack of effect the degree of cracking near the clamp has on the response of the anchorage zone. In the region encompassed by Figure 7.11, Models 4 and 5 have the best agreement to the measured values.

Other portions of the cable, however, did not match as well. For example, in the vicinity of the ram clamp, all six of the models displayed a similar smooth response, but the measured data indicated a kink in the displaced shape (Figure 7.10). Because accurate measurements in this area were difficult to obtain, the measured displaced shape near the ram clamp was not relied upon, and the agreement of the specimen models focused on the displacement ranges in the anchorage zone. As mentioned, Figure 7.11 shows the displacement range profiles for the end of the specimen that did not experience any wire breaks. The other end of the specimen (Figure 7.12) did experience wire breaks, and Models 1 and 2 did not bound the measured displacement range profile. Model 6, designed to account for the wire breaks, also did not correlate well with the experimental data. Overall, the specimen analyses had a higher level of agreement with the measured displacement data in the region not incurring any wire breaks, making the analytical modeling most applicable to the period of the fatigue testing prior to wire failure. Modeling of specimens following the onset of wire breaking is an area for future development to be discussed in the next chapter.

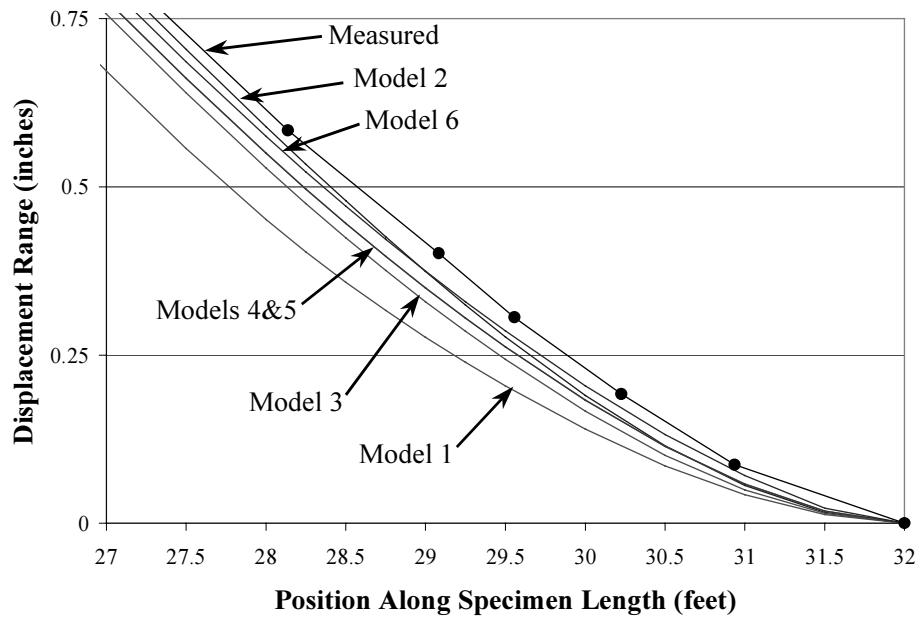


**Figure 7.12: Agreement of Specimen Models to Measured Data Based Upon Displacement Range Near Anchorage With Wire Breaks**

***Comparison of Models to Measured Stress Ranges Near the Anchorage Plate***

Extreme steel fiber fatigue stress ranges also were used as a means of comparing each of the six specimen finite element models to the experimentally obtained data. The locations of the extreme steel fiber fatigue stress range measurements, presented in Figure 7.9, were correlated to elements in each of the finite element models of the specimen. Figure 7.13 illustrates the experimentally measured deterioration of the fatigue stress range near the anchorage plate. The horizontal lines indicate the constant, predicted level for the extreme steel fiber fatigue stress range based on the noted model.

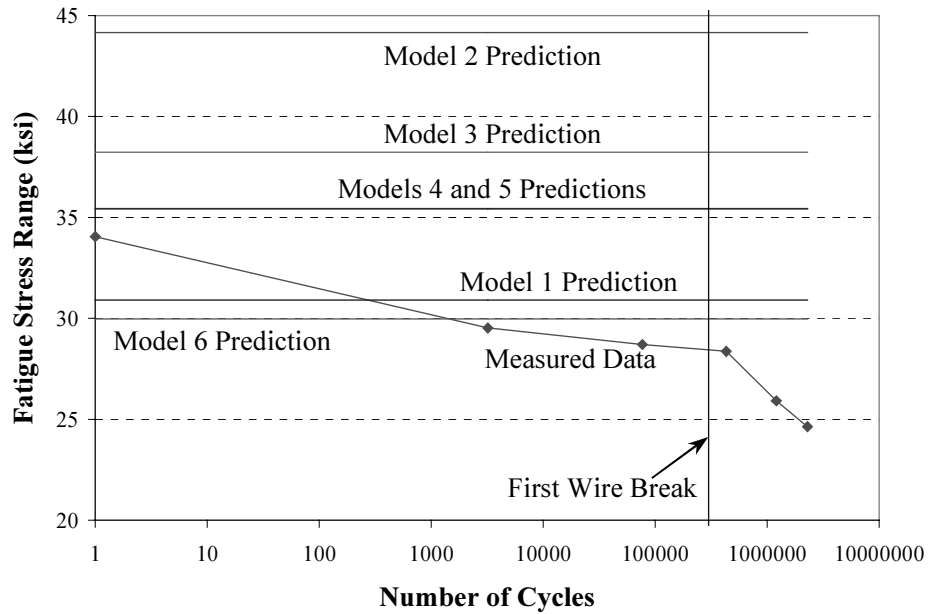


**Figure 7.13: Comparison of Predicted and Measured Extreme Steel Fiber Fatigue Stress Ranges Near the Anchorage Plate**

The cross-sectional properties of the actual specimen continually changed due to fatigue damage. Thus, any of the six models could only have been accurate for a brief period. Therefore, where each horizontal line crossed the measured data curve (assuming each did) denoted the age of the specimen (in terms of cycles experienced) for which the corresponding model may have been appropriate. One of the keys to finding an accurate model was determining how realistic the stage of deterioration represented by the model matched the age of the specimen at the point of closest correlation. For example, the uncracked Model 1 in Figure 7.13 was most applicable for the first cycle of the fatigue test instead of approximately cycle 300 where it crosses the plot of measured data.

This model, then, underestimated the stress range near the anchorage plate by 10%, assuming the strain gage data to be accurate.

At the other extreme, the predicted value from Model 6 crossed the measured data at approximately 1,000 cycles into the test. This location was also unrealistic because the first wire break was not detected until 300,000 cycles had been experienced. The prediction of Model 6 was most applicable to the end of the test. This model, then, overestimated the stress range near the anchorage plate by over 20%.

The proper placement of the remaining models, in terms of the number of cycles experienced by the specimen, was not as evident. The conditions depicted by Models 3, 4, or 5 could have been realized one hundred or one hundred thousand cycles into the test. Consequently, bounds were placed on the conditions. The specimen could reasonably have experienced the degrees of damage represented in Models 3, 4, and 5 at any time between the first cycle and the first wire break at 300,000 cycles. This definition implied that Model 3 overestimated the stress range near the anchorage plate by 12-35% and Models 4 and 5 both overestimated the stress by 4-25%. The prediction of Model 2 was used as a bound on the displacement range comparison, as discussed earlier, and did not produce accurate stress values for the anchorage plate region.

### ***Comparison of Models to Measured Stress Ranges Near the Tension Ring***

Similar to the display for the stress near the anchorage plate, Figure 7.14 shows the experimentally measured deterioration of the fatigue stress range near the tension ring. The horizontal lines again indicate the constant, predicted level

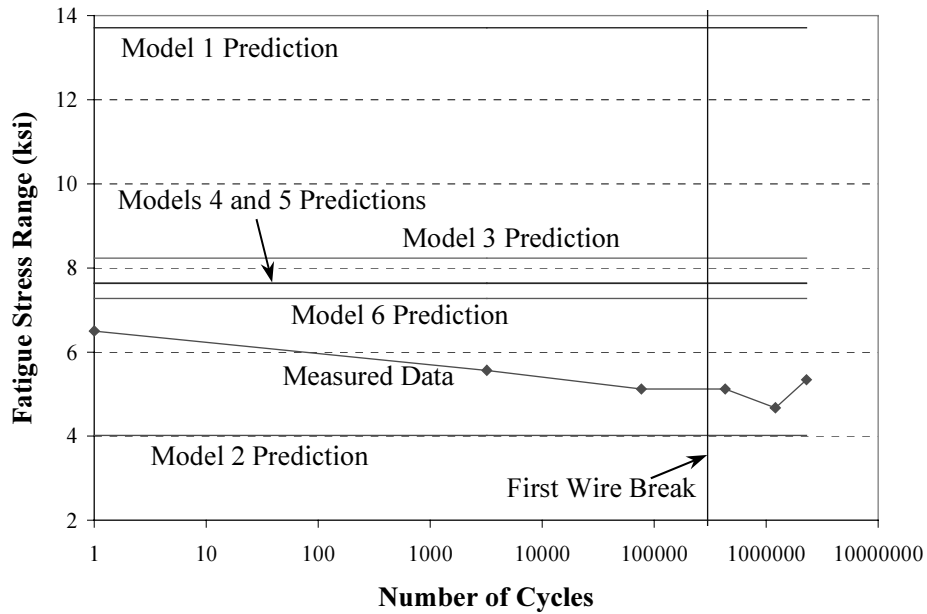


**Figure 7.14: Comparison of Predicted and Measured Extreme Steel Fiber Fatigue Stress Ranges Near the Tension Ring**

for the extreme steel fiber fatigue stress range based on the noted model. Models 1 and 2 provided a bound for the predictions of all of the other models as well as the measured values. The stress profiles for Models 1 and 2 more effectively demonstrate how the models serve as the extremes (Figure 7.15). Only half of the specimen's length is shown. The uncracked Model 1's profile possessed the local maximum near the tension ring (4-feet from the end of the cable) described in Chapter 6 while the groutless Model 2's profile did not. All of the other models, along with the actual specimen behavior, lie within this range.

General agreement between the models and the experimental stress data, however, was very poor. Model 3 overestimated the stress range near the tension

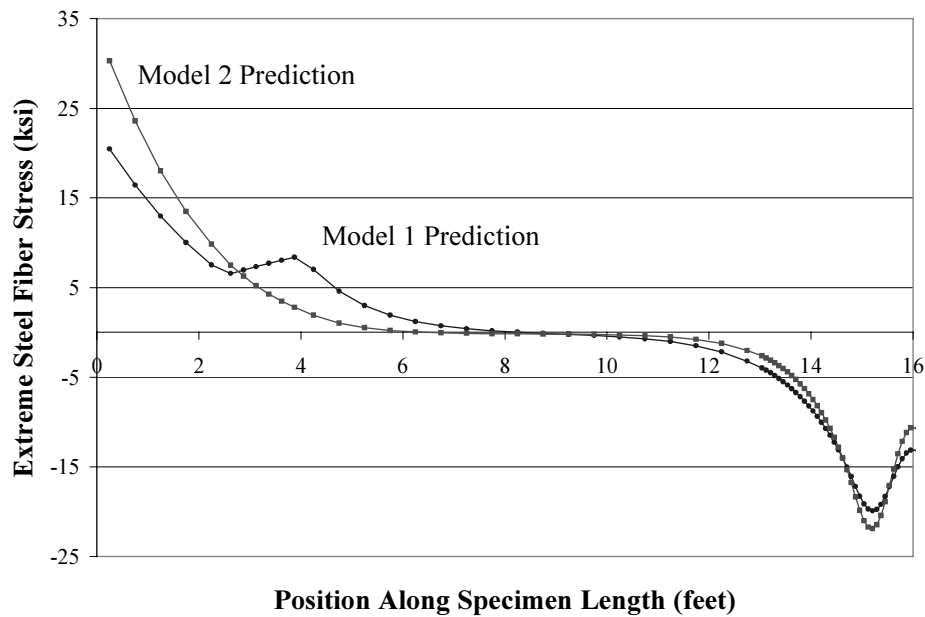


**Figure 7.15: Extreme Steel Fiber Stress Profiles for Models 1 and 2**

ring by 27-61% relative to the first cycle and first wire break, and Models 4 and 5 predicted a value 18-49% higher than that measured at the first cycle and the first wire break, respectively. The Model 6 prediction exceeded the final experimental value by 36%. Model 1 was the original model used for the specimen design. As shown in Figure 7.13, this uncracked model was not a bad predictor of the initial stress range near the anchorage plate. However, Figure 7.14 indicates that Model 1 overestimated the stress range near the tension ring by 110% relative to the first cycle. A possible explanation for the poor agreement of every model in the area near the tension ring will be discussed in the next chapter.

### *Comparison of Models to Measured Stress Ranges Near the Ram Clamp*

The finite element models exhibited better correlation with the measured extreme steel fiber fatigue stress ranges near the ram clamp (Figure 7.16). Models 1 and 2 again provided a bound for each of the other models and for the majority of the measured data prior to the first wire break. Models 3, 4, 5, and 6 all provided predictions within 3% of the last measured point before the first wire break. As the cycle numbers corresponding to degrees of damage represented in each model were not known, Models 3, 4, and 5 agreed with the measured response as well as reasonably could be discerned.

The strain gage, and, thus, the position of the model element providing the predicted stress, could not be located at the expected peak of the stress

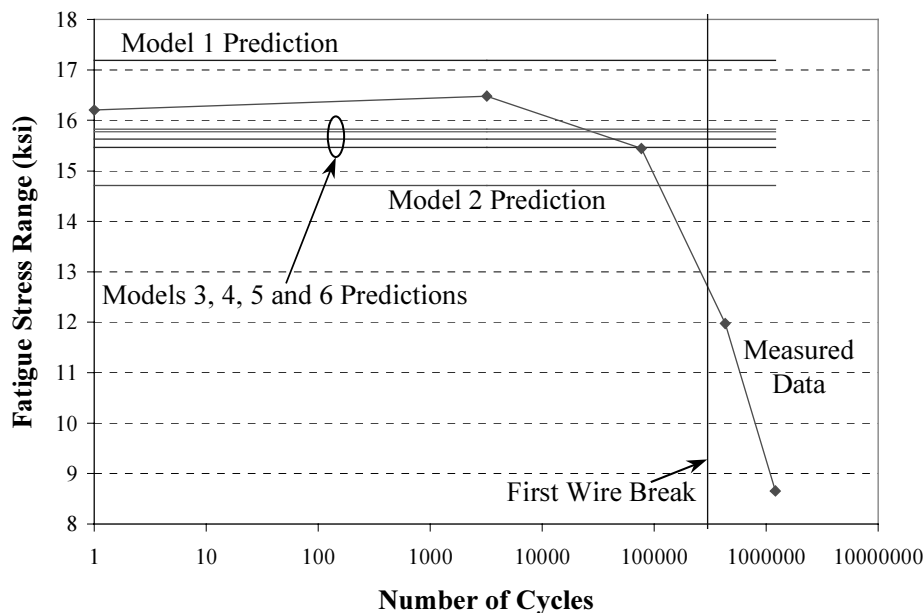


**Figure 7.16: Comparison of Predicted and Measured Extreme Steel Fiber Fatigue Stress Ranges Near the Ram Clamp**



concentration produced by the hydraulic ram load due to interference with the ram clamp. Consequently, while the finite element models may have provided adequate results compared to the location of the strain gage, it was unknown if the maximum stress values predicted by the analyses near the ram clamp were ever realized by the laboratory specimen. Wire breaks near the ram clamp did indicate, though, that the stress concentrations in this area were large enough to initiate failure.

#### ***Comparison of Models to Measured Data Using Hydraulic Ram Force and First Fundamental Frequency***

An additional indicator of the correlation of the six specimen finite element models to the actual experimental response was the predicted hydraulic ram force range necessary to attain the required displacement amplitude. As a result of the laboratory test being conducted using displacement control, this force range decreased as the test progressed (Figure 7.17). The horizontal lines indicate the constant, predicted level for the hydraulic ram force range based on the noted model. The uncracked model used to design the testing parameters (Model 1) overestimated the ram force range by nearly 30% relative to the initial measured value. The closest prediction (Model 6 relative to the last measured value) overestimated the ram force range by almost 20%.

The decreasing force predictions signified the relative overall stiffness of the specimen models just as the displaced shape did for the anchorage region (Figure 7.11). Model 1, as expected, had the highest stiffness while Model 6 had the lowest. A frequency extraction from the specimen models also supported this relationship as a higher frequency indicated greater stiffness with mass held

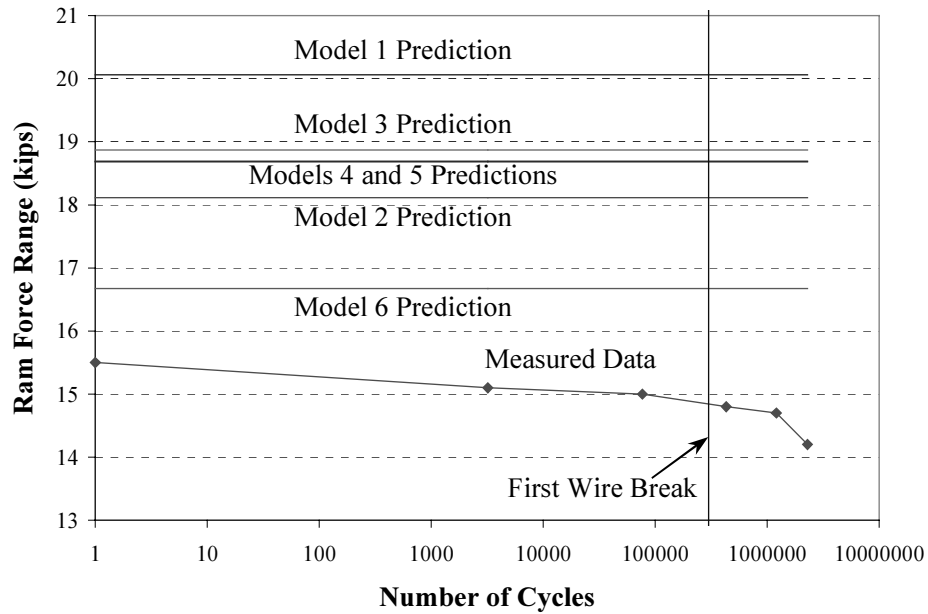


**Figure 7.17: Comparison of Predicted and Measured Ram Force Range**

constant (Figure 7.18). The measured ram force values showed that the actual stay cable specimen was not as stiff as any of the analyses indicated, but a measurement of the first fundamental frequency of the specimen initially seemed to oppose this trend.

The acoustic monitoring equipment used to detect wire beaks was utilized to acquire a frequency spectrum of the cable, in free vibration, before commencement of fatigue testing and after completion of the cycles. The lowest mode's frequency was measured to be approximately 26 Hertz prior to the test and nearly 12 Hertz following conclusion of the test. The initial value implied that the actual specimen's stiffness might have been much higher than those associated with any of the finite element models. Perhaps the simplest way the

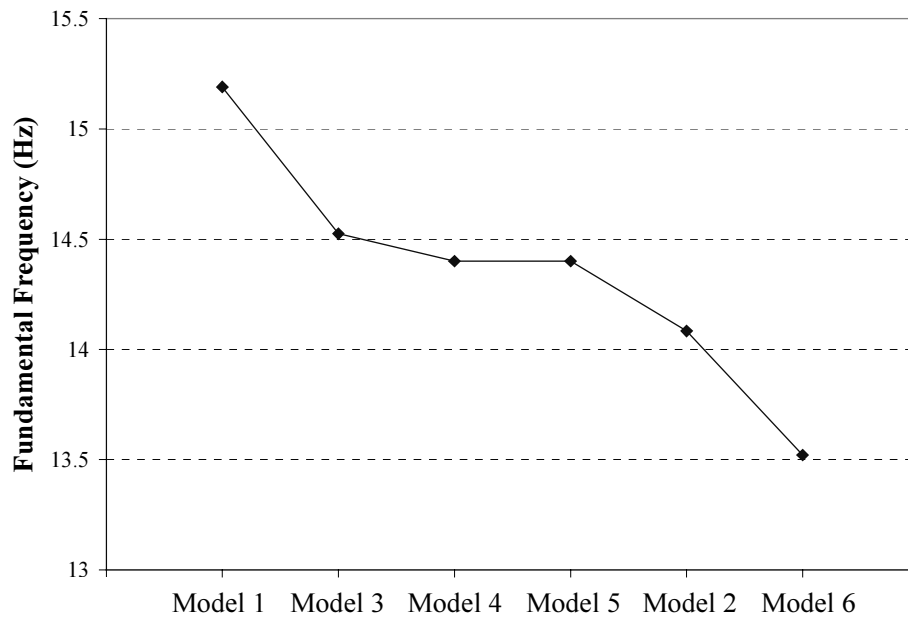


**Figure 7.18: Comparison of Predicted First Fundamental Frequencies**

specimen could have attained a larger stiffness involved the tensioning of the steel strand. The lateral stiffness of a cable structure is directly related to its axial force; a higher tension produces larger stiffness. Manipulation of the uncracked model, however, indicated that a pretension of approximately 1550 kips (6900 kiloNewtons) would have been required to produce a stiffness resulting in the measured frequency. This load corresponded to an unlikely 250% error in prestressing. Additionally, the lower specimen stiffness as indicated by the measured ram force, coupled with the frequency extraction following the conclusion of the fatigue test, implied that the initial frequency measurement did not accurately represent the first-mode response of the cable.

The first-mode frequency of almost 12 Hertz, established after the first fatigue test, did not represent deterioration of stiffness from the initial 26-Hertz measurement. Rather, the cable stimulation from the initial measurement did not excite the structure's first mode. If 26 Hertz was considered a second-mode frequency, Models 4 and 5, for example, overestimated the second-mode frequency by approximately 12%, following the trend that the actual specimen stiffness was less than the analyses predicted. Additionally, the second-mode frequency measured after completion of the test was approximately 24 Hertz, representing a 2-Hertz decline from the beginning to the end of the test.

#### ***Optimum Specimen Finite Element Model***

Of the finite element models presented, Model 5 most accurately portrayed the response of the actual stay cable specimen. The measured displaced shape at the anchorage of the specimen not possessing wire breaks (Figure 7.11) validated the model. Additionally, Model 5 predicted extreme steel fiber fatigue stress ranges close to those measured near the face of the anchorage plate and in the vicinity of the ram clamp. Even though all of the models performed poorly in predicting stress ranges near the tension ring (for possible reasons still to be discussed), Model 5 was among the closest to the actual measured values.

For the majority of the comparisons, Models 4 and 5 provided nearly indistinguishable results. Model 5, however, represented a more realistic degree of fatigue damage. The two models were identical (Table 7.1) except that model 5 incorporated a groutless section next to the ram clamp to simulate potentially excessive grout crushing. Given the predicted stress profiles, it was more likely

to obtain groutless cross-sections both at the face of the anchorage plate and next to the ram clamp, rather than just at the anchorage plate.

The goal of refining the specimen's finite element model was to control more accurately the stress ranges incurred by the specimens to follow. As discussed, the level of deterioration represented by each finite element model may have been applicable for only a short period of the specimen's life. Model 5 represented a typical state of fatigue damage between the first cycle and the event of the first wire break. Therefore, Model 5 only supplied the ability to predict the stress ranges in the specimen for a period of the specimen's life. Further, this period of the cable's life could not be defined in terms of cycles.

Accurate predictions of the stress ranges at better defined points of the specimen's life, such as at the beginning of the test, however, would not be as relevant. For example, cracking during the first cycle permanently changed the cross-sectional properties of the specimen, making these ranges not pertinent to a discussion of fatigue. A similar argument applies to the condition of the specimen at the end of the test. The most applicable state of deterioration is that which lasts the longest and experiences the most fatigue cycles. The extent of the fatigue damage depicted in Model 5, therefore, provided a better representation of the degree of deterioration to be used in establishing the target fatigue stress ranges for the subsequent laboratory tests. Potential for improvement of this process is offered in the next chapter.

## **Chapter 8: Summary, Conclusions, and Recommendations for Future Work**

The development of cable-stayed bridges has included the discovery of unique phenomena such as rain-wind induced vibration. Excessive lateral motion of the cables supporting structures such as the Fred Hartman Bridge has instigated major research. The primary investigations have focused on vibration prevention and assessment of bending fatigue damage.

### **Measurement of Strain on the Stay Cables of the Fred Hartman Bridge**

To characterize rain-wind induced vibration events using strain data, strain collection instrumentation was maintained on the Fred Hartman Bridge. As of the time of writing, repeated efforts had not yielded any discernable strain data from a vibration event. Reduction or elimination of signal noise, considered to be the most significant problem, is the primary future consideration in this aspect of the study. Ideally, autonomous instrumentation should be developed that does not rely on Johns Hopkins University's data acquisition system. Similar to the secondary strain acquisition attempt outlined in Chapter 4, an effort to artificially excite the cable should be made. The forced excitation, however, should be mechanical rather than manual. The manual pluck tests proved that significant excitation is difficult to achieve by hand.

Strain data obtained from an artificial excitation may also provide insight into the axial strain representation of lateral vibration discussed in Chapter 5. The

convenient location of strain gages at the level of the guardrail may not be an area of high curvature. Therefore, the responses to the excitation of the flexural strain and axial strain histories should be compared to validate the analytical axial strain investigation and make vibration events easier to calibrate in the future.

The acquisition of strain data from vibration events is crucial to the assessment of stay cable fatigue damage because the information allows fatigue stress ranges to be identified for actual oscillation events encompassing a spectrum of severity. The fatigue stress ranges, however, can only be determined for the points of strain measurement. Therefore, strain data from vibration events are, perhaps, more vital to the process of validating finite element models that can be used to predict fatigue stress ranges at all points of a stay cable.

### **Finite Element Modeling of Fred Hartman Bridge Stay Cables**

The ABAQUS models of cables A24S and A22S represented an early generation of stay cable finite element models. Validation was not directly attainable due to the lack of strain data, but a critique of the general modeling technique can be drawn from the validation and adaptation of the specimen finite element models. Both the cable A24S and cable A22S models produced extreme grout fiber stress values well in excess of the grout's modulus of rupture. The cables were modeled with uncracked sections because observations on the bridge revealed that discernable cracks were not significant. Inspection of the grout, however, was only possible at the windows cut in the polyethylene sheath near the tension ring and at the level of the guardrail. The region of the cable closest to the

anchorage was obstructed by the superstructure, preventing observation of the grout condition.

### ***Effect of End Rotation***

The high stresses near the anchorage were calculated from the curvature profile produced by ABAQUS. The magnitudes of the curvature profile along the anchorage and transition regions were greatly influenced by the end fixity preventing rotation. Two realistic scenarios would decrease the magnitudes of the curvature profile: 1) localized damage permitting rotation and 2) the support allowing rotation while behaving with some degree of partial fixity. The first condition was represented in specimen Models 4 and 5 in Chapter 7 through the groutless section at the face of the anchorage plate. In the models, local damage had crushed the grout beyond all load carrying ability, allowing, in essence, rotation of the cable about this damage point at the expense of a high curvature value for that single element. A partial fixity would have provided much the same behavior, allowing rotation at the cable supports without inflicting higher curvature on any element.

Increased rotation at the anchorage reduces the curvature along the rest of the cable near this region. This reduction implies a lower stress range at the tension ring. Figure 8.1 compares the extreme steel fiber stress for the uncracked Model 1 with the extreme steel fiber stress for Model 5, normalized to the same maximum value. Model 5 maintained the high stress at the face of the anchorage plate, but the remainder of the stress profile fell below Model 1.



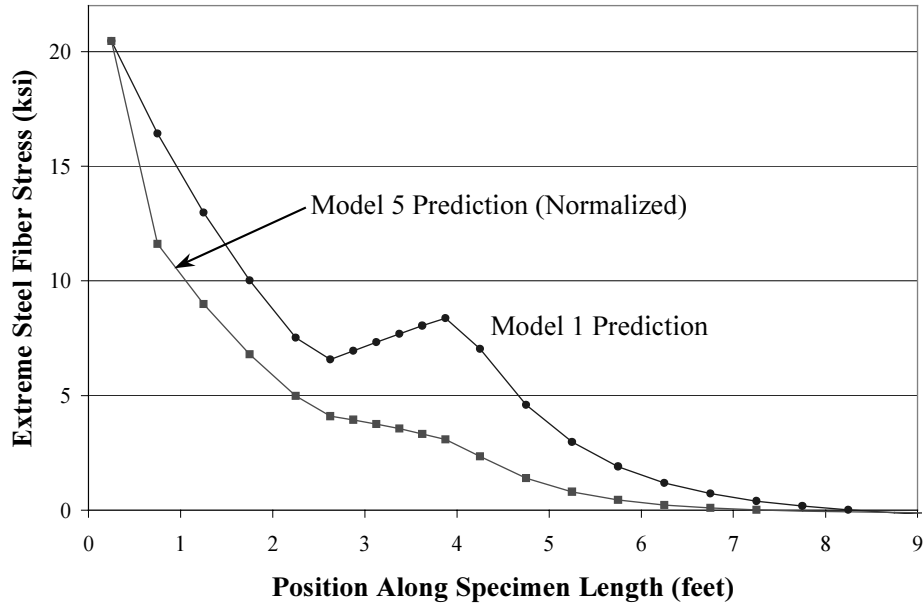


**Figure 8.1: Effect on Stress Profile of End Rotation Due to Local Damage**

This behavior was observed on the first bending fatigue specimen and may explain the poor agreement of the models to the experimental results near the tension ring. If the end rotation is a result of local damage at the face of the anchorage plate, the anchorage stresses can still reach high values, but the rotation reduces the intermediate curvature and, thus, reduces stress values farther from the anchorage. This trend was evident when considering the ratio of extreme steel fiber stress at the face of the anchorage plate to the tension ring (Chapter 6). The first specimen was designed (with an uncracked model) to possess a ratio of 2.44. The strain gages mounted on the specimen could not be located directly at the tension ring or at the anchorage, but an estimate for the steel stress ratio of the actual specimen was 5.4, based on the nearest gages. The lack of agreement

between the predicted and measured ratios directly demonstrates the effect of end rotation from localized damage or a source of partial fixity.

If the source of rotation is local damage, this phenomenon has some major implications. First, the location of the tension ring may not be as critical a fatigue location as previously assumed. The tension ring, however, does still produce a high normal force that contains the splaying strands. The high normal force may exacerbate fretting fatigue even though the extreme steel fiber fatigue stress ranges may not be as high as believed. Second, the region of cable at the face of the anchorage plate may be an area of greater concern than previously assumed because serious damage to this vicinity may not be evident. The grout condition at the face of the anchorage plate has never been inspected. More importantly, localized damage in that region may be preventing excessive deterioration of the grout in the rest of the cable, allowing current observations of minimal cracking in areas away from the anchorage to provide a false sense of security concerning the overall condition of the stay cable.

At the present time, however, these conclusions only represent hypotheses for the continuation of the study. A post-mortem investigation of the first stay cable specimen should reveal the extent of the grout damage localized at the face of the anchorage plate. This examination will help distinguish the source of any end rotation. A more optimistic scenario would be movement of the entire support allowing the end rotation instead of localized damage. Regardless of the degree of damage to the first specimen at the anchorage plate, further finite

element modeling should consider varying degrees of partial fixity at the supports of the stay cables of the Fred Hartman Bridge.

Additionally, the cable A24S and cable A22S models should be revised to account for grout cracking along the length of the cable structure. As a minimum, the cross-sectional properties should be calculated neglecting the tension zone of the grout. If further research warrants, the models should be further modified to include a groutless section at the face of the anchorage plate. Perhaps extreme steel and grout fiber fatigue stress ranges more realistic than those previously obtained may be acquired. Strain measurements from the Fred Hartman Bridge may be used to validate these models once such data are collected.

### **Finite Element Modeling of Laboratory Stay Cable Specimen**

Many of the considerations for the cable A24S and A22S models apply also to the specimen finite element models. For example, the effect of partial fixity should be investigated. Models 1 through 6, outlined in Chapter 7, all incorporated a rotational spring at the anchorages to account for the rotation of the reaction frame. While these springs did allow some end rotation, the magnitudes were minimal, and lower degrees of fixity require investigation.

### ***Material Property Adjustment***

A potentially significant source of modeling error lies in the material properties used for all of the analyses. Based on the work of Hamilton (1995), 4000 kips per square inch (28 gigaPascals) was used as the modulus of elasticity of the grout, and 27,600 kips per square inch (190 gigaPascals) was used as the

modulus of elasticity of the steel strand. The modulus of elasticity of grout is difficult to calculate, but various design recommendations exist. Perhaps the most applicable equation comes from the American Concrete Institute's *Code Requirements For Masonry Structures* (ACI 530-99) (Equation 8.1). The modulus of elasticity of grout,  $E_g$ , is defined in terms of the grout's compressive strength,  $f_g$ .

$$E_g = 500 f_g \quad \text{Equation 8.1}$$

Although grout cubes should have been tested in stages during the first fatigue test, they were only tested at the end of the test, 47 days after grouting of the specimen. Compressive strengths ranged from 4.13-8.09 kips per square inch (28.5-55.8 megaPascals) with an average of 5.43 kips per square inch (37.4 megaPascals). Moduli of elasticity ranged from 2070-4050 kips per square inch (14.3-27.9 gigaPascals) with an average of 2890 kips per square inch (19.9 gigaPascals). Despite the fact that the design equations are typically conservative, the modulus of elasticity of the first specimen was likely lower than the value used in the finite element models, supporting experimental measurements that the specimen stiffness was lower than predicted.

A significant improvement to the analyses would be the modification of the material properties. The modulus of elasticity of the strand could be similarly determined, and the modulus of elasticity of the grout at various stages of the specimen's life could be estimated from a series of grout cube tests. The last analysis of a particular specimen, finalizing the testing parameters, could be executed with a current estimate of the grout modulus of elasticity shortly before

beginning a new test. Similarly, progressive grout cube tests could allow for predictions of stress ranges during a test. An accurate estimate of the degree of fatigue deterioration also would be required.

### ***Modeling Stages of Fatigue Deterioration***

Varying levels of fatigue damage were represented with Models 1 through 6, but improvements are recommended. While Model 5 provided an adequate representation of a typical level of fatigue damage prior to the first wire break, a model does not exist that accurately predicts the behavior of a specimen with wire breaks. Model 6 depicted fourteen wire breaks localized in each of the two anchorages, but it did not correlate well with measured data for several possible reasons. First, the exact number, and especially location, within the cross-section of the breaks was not known. Modeling attempts were based solely on the assumption that the extreme fiber steel would fail earliest.

Additionally, the loss of prestress associated with the wire breaks was considered to be complete, affecting the entire cable. Theoretically, because of development length considerations, a wire break at the anchorage may not affect the prestress in the center of the cable. Thus, these factors should be considered when improving any finite element models of the specimen that include wire failure.

A legitimate goal of the specimen analyses is a series of accurate models representing the stages of deterioration of the specimen. The first specimen was tested using displacement control, meaning that as fatigue damage progressed, stress ranges decreased. If accurate models for numerous stages of the cable's life

exist, the displacement could be adjusted to maintain the same maximum fatigue stress range as the test progresses. As discussed in the previous chapter, assessing the degree of grout deterioration is difficult. Therefore, the location of the wire breaks would have to be relied upon to modify the model. An additional problem lies in the fact that the location in the cross-section of the wire break is not known. Estimates could be made based upon the findings of the post-mortem investigation of the first specimen.

Similarly, if these progressive models prove to be reliable, analogous models could be established for each of the bridge cables. Then, the response of the actual cable could be matched to a model to assess the degree of deterioration. A potential method of correlation deals with a comparison of fundamental frequencies, which are easily attainable from the stay cables on the bridge structure with a pluck test. A problem with this approach, however, is the possibility of measuring a different phenomenon such as loss of prestress due to strand relaxation rather than the degree of fatigue deterioration. Potential exists, though, to monitor other physical data, such as displacements or acceleration, to correlate a stay cable to an appropriate model.

The ultimate objective of all of the finite element analyses, strain collection, and laboratory fatigue testing is assessment of the extent of the bending fatigue damage incurred by the stay cables of the Fred Hartman Bridge. Correlating observed displacements and measured strains or accelerations to the fatigue life of a stay cable is paramount in this evaluation. The establishment of a set of procedures for evaluating stay cable fatigue damage will allow the

condition of every cable on the Fred Hartman Bridge, and possibly others, to be identified, reliably predicting the current lifespan of individual bridge cables.

## Bibliography

- ABAQUS/Standard User's Manual: Version 5.8*. 1998. Hibbitt, Karlsson, and Sorensen, Inc.
- Andersen, H., D. L. Hommel, and E. M. Veje, 1999. Emergency Rehabilitation of the Zarate-Brazo Largo Bridges, Argentina. *IASBE Conference, Malmo 1999: Cable-Stayed Bridges – Past, Present, and Future [CD-ROM]*. 698-706.
- Angelo, W. J. 2000. Towering Cable-Stayed Crossing Adds Monument to Boston Skyline. *Engineering News Record*. 21 February.
- Berketa, R. 2000. Niagara Falls Thunder Alley Web Page. [www.iaw.com/~falls](http://www.iaw.com/~falls).
- Bournand, Y. 1999. Development of New Stay Cable Dampers. *IASBE Conference, Malmo 1999: Cable-Stayed Bridges – Past, Present, and Future [CD-ROM]*. 559-566.
- Buckland and Taylor, Ltd. Bridge Engineering Home Page. 1999. [www.b-t.com/projects/alexfras.htm](http://www.b-t.com/projects/alexfras.htm).
- Code Requirements For Masonry Structures* 1999. American Concrete Institute. ACI 530-99.
- Dowd, J. A., and D. B. Thatcher. 2000. *Investigation of the Perfect Flexibility Assumption in the Analysis of Cable Structures*. Class Project, CE381P, The University of Texas at Austin.
- Dowd, J., M. Poser, K. Frank, S. Wood, and E. Williamson. 2001. Bending Fatigue of Cable Stays, not yet published.
- Dupre, J. 1997. *Bridges*. New York: Black Dog and Leventhal Publishers.
- Feld, J., and K. L. Carper. 1997. *Construction Failure*. 2d ed. New York: John Wiley and Sons.
- Frank, K. H. 2000. Personal conversation.



- Gimsing, N. J. 1997. *Cable Supported Bridges: Concept and Design*. 2d ed. Chichester: John Wiley and Sons.
- Gimsing, N. J. 1999. History of Cable-Stayed Bridges. *IASBE Conference, Malmo 1999: Cable-Stayed Bridges – Past, Present, and Future [CD-ROM]*. 8-24.
- Hamilton, H. R. III. 1995. *Investigation of Corrosion Protection Systems for Bridge Stay Cables*. Ph.D. diss., The University of Texas at Austin.
- Hamilton, H. R. III, J. E. Breen, and K. H. Frank. 1998. Bridge Stay Cable Corrosion Protection. I: Grout Injection and Load Testing. *Journal of Bridge Engineering* 3, no. 2:64-71.
- Hamilton, H. R. III, J. E. Breen, and K. H. Frank. 1998. Bridge Stay Cable Corrosion Protection. II: Accelerated Corrosion Tests. *Journal of Bridge Engineering* 3, no. 2:72-81.
- Hikami, T. and N. Shiraishi. 1988. Rain-Wind Induced Vibration of Cables in Cable Stayed Bridges. *Journal of Wind Engineering and Industrial Aerodynamics* 29, 409-418.
- Irvine, M. 1993. Local Bending Stresses in Cables. *International Journal of Offshore and Polar Engineering* 3, no. 3:172-175.
- Ito, M. 1999. Stay Cable Technology: Overview. *IASBE Conference, Malmo 1999: Cable-Stayed Bridges – Past, Present, and Future [CD-ROM]*. 481-490.
- Johnson, E. A., G. A. Baker, B. F. Spencer, and Y. Fujino. 1999. Semiactive Damping of Stay Cables. *Journal of Engineering Mechanics*. Preliminary submission.
- Kesner, K., and R. W. Poston. 1999. *Progress Report No. 2: Evaluation and Repair of Stay-Cable Vibrations, Fred Hartman Bridge, Veterans Memorial Bridge*. Whitlock Dalrymple Poston Project No. 06-95114B.
- Leonhardt, F., and W. Zellner. 1991. Past, Present and Future of Cable-Stayed Bridges. In *Cable Stayed Bridges: Recent Developments and their Future*. Ed. M. Ito, Y. Fujino, T. Miyata, and N. Narita. Amsterdam: Elsevier. 1-34.

- Main, J. A., and N. P. Jones. 2000. Full-Scale Measurements of Stay Cable Vibration. Presented at Whitlock Dalrymple Poston & Associates' Progress Report Meeting on Evaluation and Repair of Stay-Cable Vibrations, Fred Hartman Bridge, Veteran's Memorial Bridge.
- Miyazaki, M. 1999. Aerodynamic and Structural Dynamic Control System of Cable Stayed Bridge for Wind Induced Vibration. *IASBE Conference, Malmo 1999: Cable-Stayed Bridges – Past, Present, and Future [CD-ROM]*. 86-94.
- Ohashi, M. 1991. Cables for Cable-Stayed Bridges. In *Cable Stayed Bridges: Recent Developments and their Future*. Ed. M. Ito, Y. Fujino, T. Miyata, and N. Narita. Amsterdam: Elsevier. 125-150.
- Pacheco, B. M. and Y. Fujino. 1993. Keeping Cables Calm. *Civil Engineering* 63, no. 10:56-58.
- Poser, M. 2001. Master's Thesis, The University of Texas at Austin, in progress.
- Poston, R. W. 1998. Cable-Stay Conundrum. *Civil Engineering* 68, no. 8:58-61.
- Poston, R. W. 2000. Personal conversation.
- Raouf, M. 1992. Free Bending Fatigue of Axially Pre-Loaded Spiral Strands. *Journal of Strain Analysis* 27, no. 3:127-136.
- Raouf, M. 1993. Design of Steel Cables Against Free-Bending Fatigue at Terminations. *The Structural Engineer* 71, no. 10:171-178.
- Sarkar, P. P., and T. B. Gardner. 2000. Model Tests to Study Rain/Wind-Induced Vibration of Stay Cables. Presented at Whitlock Dalrymple Poston & Associates' Progress Report Meeting on Evaluation and Repair of Stay-Cable Vibrations, Fred Hartman Bridge, Veteran's Memorial Bridge.
- Verwiebe, C. 1998. Rain-Wind-Induced Vibration of Cables and Bars. In *Bridge Aerodynamics*. Ed. Larsen and Esdahl. Rotterdam: Balkema. 255-263.
- Virlogeux, M. 1998. Cable Vibrations in Cable-Stayed Bridges. In *Bridge Aerodynamics*. Ed. Larsen and Esdahl. Rotterdam: Balkema. 213-233.
- Wardlaw, R. L. 1991. Cable Supported Bridges Under Wind Action. In *Cable Stayed Bridges: Recent Developments and their Future*. Ed. M. Ito, Y. Fujino, T. Miyata, and N. Narita. Amsterdam: Elsevier. 213-234.

- Watson, S. C., and D. Stafford. 1988. Cables in Trouble. *Civil Engineering* 58, no. 4:38-41.
- Wilcox, A. 1998. *Determining the Vibration-Induced Stresses in the Stay Cables of the Fred Hartman Bridge*. Master's Departmental Report, The University of Texas at Austin.
- Yamaguchi, H. and Y. Fujino. 1998. Stayed Cable Dynamics and Its Vibration Control. In *Bridge Aerodynamics*. Ed. Larsen and Esdahl. Rotterdam: Balkema. 235-253.

## **Vita**

Joseph Arthur Dowd was born in Rockville Center, New York on January 3, 1977, the son of Judith Alice and Joseph Julian Dowd. After being raised in Sherman, Connecticut and Colleyville, Texas, he became a May 1995 graduate of Grapevine High School in Grapevine, Texas. The following fall, he entered Texas A&M University in College Station, Texas, pursuing a Bachelor of Science in Civil Engineering with an emphasis on structures. In May of 1999 he graduated summa cum laude with University Honors. Following graduation, he worked for L.A. Fuess Partners of Dallas, Texas, and in September of 1999, he continued his education at The University of Texas at Austin. Since August of 2000 he has been happily married to Alisa Carol Calloway of Dallas, Texas. He will be employed by Walter P. Moore and Associates in Dallas, Texas beginning in June of 2001.

Permanent address: 2009 Woodstock Drive  
Colleyville, Texas 76034

This thesis was typed by the author.